Università degli Studi di Catania

Dottorato di Ricerca in Fisica

XXVII Ciclo

Paolo M. Sberna

Novel Approaches to Photoactive Nanostructured Materials for Efficient Solar Cells

Tutor: Prof.ssa Francesca Simone

Supervisors: Prof.ssa Elvira Fortunato

Dott.ssa Maria Miritello

Dott. Salvatore Mirabella

Coordinatore: Prof. Francesco Riggi

Tesi per il conseguimento del titolo

Dicembre 2014

List of abbreviations

ARC: anti-reflection coating

CSP: concentrating solar power

CVD: chemical vapor deposition

EF: Raman intensity enhancement factor

EF-TEM: energy filtered transmission electron microscopy

EROI: energy return on investment

FE-SEM: field emission scanning electron microscopy

FWHM: full width half maximum

GDP : gross domestic product

ICT : information and communications technology

MG: metallic grating

MNP: metallic nano-particle

NP: nano-particle

NS: nano-structure

NW: nano-wires

PBG: photonic band gap

PC: photonic crystal

PDOS: photon density of states

PERL *solar cell*: passivated emitter rear locally diffused solar cell

PNJ: photonic nano-jet

PV: photovoltaic

QD: quantum dot

QE: quantum efficiency

RBS: Rutherford back scattering spectrometry

TEM: transmission electron microscopy

XRD: X-ray diffraction

List of symbols

$f_e(E)$: Fermi distribution

E_f : Fermi energy

K: Boltzmann constant

T: absolute temperature

n_e: density of electrons in the conduction band

n_h: density of holes in the valence band

n_i: intrinsic electron density

N_C: effective density of state in the conduction band

N_V: effective density of state in the valence band

E_C: conduction band edge level

E_V: valence band edge level

E_g: band gap

F: free energy

E: energy

S: entropy

N: number of particles

E_e: electron energy

E_h: hole energy

p: pressure

V: volume

μ: chemical potential

φ: electrical potential

ζ: electro-chemical potential

h: Planck constant

$\hbar$: reduced Planck constant

ω: frequency

Ω: solid angle

J: current density

η: efficiency

R_r: radiative recombination rate

R_{nr}: non-radiative recombination rate

P: power

B: light trapping factor

t: time

n: refraction index

$S(\lambda)$: solar cell spectral response

$R(\lambda)$: reflection coefficient

$T(\lambda)$: transmittance

α: absorption coefficient

A: absorptivity

ε: dielectric constant ($\varepsilon = \mathrm{Re}[\varepsilon] + i \cdot \mathrm{Im}[\varepsilon]$)

α: polarizability

$\boldsymbol{\xi}$: electric field

$\boldsymbol{p}$: dipole moment

$\boldsymbol{k}$: wave number

Contents

Chapter 1- ENERGY: RESOURCES AND TECHNOLOGIES

Chapter 2- LIGHT TRAPPING FOR PHOTOVOLTAICS

Chapter 3 - CUPROUS OXIDE

1 - ENERGY: RESOURCES AND TECHNOLOGIES

1.1 - Introduction: basic concepts and consumption

The eminent scientist R. Feynman wisely stated that humans have no knowledge of what energy is. This challenging remark could sound curious considering that nowadays Mathematics, Physics and Engineering provide the theoretical instruments, the concepts and the practical notions to attain a deep and broad understanding of the mechanisms which govern energy transformations and production. Such a lack of general knowledge and awareness of this issue would be due to the fact that the concept of energy permeates all the rules of the Universe, from the fundamental ones to the laws of the upper complex levels. Even though this issue is extremely intricate, it is needed to initially focus on drafting some energy concerning notions and ideas not only to offer a stimulating taste of first principles but mainly to furnish a basal frame for the themes dealt in this thesis.

The first intuitive feeling of energy is that it makes things happen through changes of states and transformations; thus energy is closely connected with another elusive concept, that is time. Specifically, quantum physics proffers a fascinating picture about energy and time connection. The second simple perception is that energy is the capacity of a system of producing work: i.e. exerting a force for a certain distance. From the first idea the concept of energy related to movement of bodies (kinetic energy and thermal energy) together with the concepts of energies associated to absorption and decays of systems (electro-magnetic energy) come out. Whereas from the second idea the notion of potential energy in all its forms (mechanical, nuclear, chemical and electrical) emerges. At the beginning of the last century, A. Einstein discerned and demonstrated that energy and mass are two different forms of the same stuff. Hence energy is so intimate to things that it constitutes also their essence.

Energy cannot be created or destroyed. It can be transformed from a given type to another form by means of various processes and reactions which human-kind has learnt to exploit and control since its rise. The numerous forms of energy are not equivalent according to the perspective of technological uses and human purposes. Some kinds of energy are easily marketable (so valuable), as electrical energy, other ones are fruitless, as low temperature dissipated heat. Between these extremes there is a group of energy forms (mostly embodied in natural resources) that cannot be efficiently utilized directly. Thus they have to undergo conversions or secondary resources, which are more profitable and useful, have to be extracted by refining

processes. Extraction, refining and conversion require the consumption of energy and according to the laws of thermodynamics, are inexorably accompanied by a loss of a fraction of the primary energy quantity.

The parameter that quantify the above issue is the EROI (energy return on investment) calculated as the ratio of the amount of usable energy acquired from a resource to the amount of energy expended to make it available [1]. The estimation of EROI is incredibly complicated, since has to take into account scientific, economical and political aspects which generally are greatly entangled, for instance the concentration of energy stored into a given natural resource, the technological know-how to gain it, the geographic location and the associated political situation. The greater the EROI of an energy resource is than unity, the more such supply can be extensively used and pervasively spread. It is worth to specify that EROI, as most of typical parameter does not consider ecological (green house effect) and ethical matters, often arising from that resource exploitation.

The global amount of used energy (from a set of resources) is modulated by the total EROI generally in a direct manner. On the other hand, the modulation, dependent on the society needs, is a chaotic (in the mathematical sense), thus usually not fully predictable, trend. This chaotic behaviour is caused by the energy demand being in turn subject to energy availability (deterministic parameter) and life style (non-deterministic parameter). The mutual interplay between energy consumption and demand is a matter of the most advanced economical models.

Despite the fact energy consumption versus demand is, at short time scale, a complex function, a fast schematic tour in the energy use in the history could give a glance of the global trend.

From the rise of the first primitive societies up to 8.000 years ago the utilized energy sources were man power (80 W/person on the average) and biomass (mainly wood) [1]. Gradually, agriculture labour, craft activities and trade efficiencies were boosted by the exploitation of animal power (up to 800W/animal). Later with the advent of technological breakthroughs, men learned to gain mechanical energy from wind and water. Both compared to the above sources resulted more intensive, cheaper and with extended flow. Pushed by the appearance and development of the Industrial Revolution, coal progressively substituted wood as energy supply, the former having, since the XIX century, a higher EROI. When the energy stored by fossil fuels, such as gas and oil became accessible, men started to own a more versatile energy form, that could be spent for faster transportation and to improve the agricultural and industrial outcomes. Since the beginning of the last century, coal, gas and oil energy supplies, combined with the alternate current generation, made electricity one of the most

utilized energy form. In the last decades, whirling increase of information and communications technology (ICT) pervasiveness (it accounts for 10% of the total electricity consumption [1]) together with other comforts, like air conditioning, have been coercing modern developed society to be dramatically addicted to 24 h electricity thirst. Similarly, the exploitation of the chemical energy coming from oil has the same terrific proportions of the electricity use. As conclusion of this brief historical survey, it is important to underline that the gigantic energy consumption rate, sustained (but followed as well) by technological and life standard improvements, have been belonging to the tiny minority of the world rich population. This statement is further confirmed by the fact that the gross domestic product (GDP) per capita trend generally follows the same one of the energy use per capita [2].

Therefore it can be concluded that worldwide energy consumption rate is a continuously growing parameter (energy use per year increase factor / population increase factor = 6) [2]. Its destiny of inexorable exploding parameter is now reinforced as future perspective by the following points:

- In this century several billion more people will join us. Hence if the current world average per capita power use is considered the present demand growth will be roughly of the 50%[2].
- On average, the populations of the fast growing economies is going to reach the life standards, thus the energy consumptions, of rich countries. This factor will enhance the former one.
- The attempts to improve the efficiency of energy transformations, storage and usage are not enough to mitigate the previous two factors.

Even though the evolution of energy extraction and transformation have taken advantage by novel scientific and technological approaches, during all the years following the industrial revolution, the various usable forms of energy (mainly non-renewable) were treated simply as a commodity with endless supply and no long-term environmental/social impacts [1]. In other words the consumption philosophy of early men burning a bunch of wood trunks to light up a small village has not changed until now, where human activities take place at a scale, large enough to influence the planet as a whole. This problem is reflected, for instance, by the lack of controls, measurements and optimization of the power flow through the grid, which looks basically the same as that built a century ago. Hence the approach to the consumption of resources is essentially parasitic rather than symbiotic and, as it is well known from biology, parasites always kill the guest. Shifting our current socio-economic infrastructures to a sustainable system is a compelling and urgent transition whose strategy could be summarized in these five points:

- Increase the efficiency of energy use.
- Enlarge the availability and reliability of low carbon emission energy supply.
- Improve the efficiency of energy conversion and storage technologies.
- Match the renewable energy flows, which are fixed and dilute, with the power densities of energy uses in modern society.
- Tailor a global cooperation to push such transition by means of effective policies, business models and life standards.
- Recycling of critical materials.

Further details and a deeper insight of these issues will be provided in the next sections.

1.2 - Non-renewable resources

1.2.a - Oil

The existing types of oil are classified into two groups: conventional oil (liquid oil accumulated in deep reservoirs, called fields) and unconventional oil, including heavy oils, oil sands (tar sands) and fine-grained sedimentary rock containing mixed organic chemical compounds (oil shale). According to some estimates, there is as much oil shale as the total global conventional oil endowment [1]. In most conventional oil fields, the recoverable fraction by drilling and pumping is around 60% of the total stored[(1)]. Unconventional sources mining is generally a more expensive extraction method (40% of the initial energy is wasted in production [1]), causing severe environmental damages. Crude oil must be processed to become a wide variety of usable products. Oil refining is the most energy intensive industry, where energy consumption can reach half of the operating costs [1]. The advance in sophistication of extraction technologies and geological investigations is opening the access to new resources; nevertheless being oil a finite good, according to Hubbert's model [1], the global oil production is a bell shaped function of time, thus after reaching a peak of production, it inexorably will decrease. Today oil accounts for 40.8% of total world energy use [3], and at present demand conventional reserves would last for less than 100 years [2]. However oil shale energy potential is estimated to be $3 \cdot 10^4$ TW·year [2]. The prominent utilization comes from transports [3], a sector hardly supplied by renewable energy sources because of the current logistic organizations.

1.2.b - Coal

Coal is today the second primary energy supply (28.8% share [3]). Coal production should follow the Hubbert curve even though the global reserves are expected to last for centuries. Since the conversion technologies are mature, coal-based energy generation is cost effective. The main output is electricity for industries (80.7% of the total share [3]). In terms of sustainability the most urgent issue is its environmental impact, indeed 1 KWh electric energy produced by coal burning emits in the atmosphere more than 1 Kg of carbon dioxide followed by non negligible amounts of other pollutants [2]. However, thanks to the coal consumption being concentrated in big burning facilities, carbon dioxide capture systems could be integrated [1].

1.2.c - Gas

As for oil, there are unconventional (that is more difficult to exploit) gas resources such as gas hydrates which are bulky ice lattice trapping methane molecules (1 CH_4 for every 5.75 H_2O) [1]. Nowadays, natural gas total energy share is the third (21.3% [3]). The main gas use is for residential heating and cooking (44.2% [1]), yet electricity gas-based production is growing, being gas combustion the cleanest among fossil fuels (0.5 Kg of CO_2 per 1 KWh [2]). It has been estimated that gas peak world production would occur in the next decades. A promising alternative is methane hydrates exploitation, which would have a potential of $2 \cdot 10^4$ TW·year.

1.2.d - Nuclear

Nuclear energy is liberated in the form of thermal energy through the controlled fission reaction, in which U^{235} nucleus (that is the fissile isotope constituting 0.7% of the total uranium [1]) is split into smaller radioactive nuclei upon collision with a neutron. Nuclear power plants generate electrical energy (11.7% of share [3]) operating two possible fuel cycles:

- Open fuel cycles: uranium is used only once and it is disposed directly. Nuclear energy potential, considering this method, the current production and the estimated uranium resources would be only 370 TW·year [2]. The majority of operating plants use this method.
- Closed fuel cycles: in this case the used nuclear fuel is reprocessed (breeding) to recover and use the remaining fissile fuel (95% is not used during first burning [2]) facilitating the waste management. The efficiency of this method could enhance the nuclear energy potential to 7400 TW·year [2].

Nuclear fission energy is affected by the following drawbacks:

- The problem of disposition of long-living and radioactive waste is still practically unsolved;
- Risk that weapons usable material could be produced;
- Safety and security risks;
- Power plants installation is extremely capital intensive.
- Decommissioning and dismantling of power plants are generally at least one order of magnitude greater than the construction costs.

Because of the pressure exerted and the doubts rose by these issues, nuclear electricity generation globally is decreasing (2% in 2007 [1]).

1.3 - Renewable resources

The outer boundary of Earth atmosphere is invested by 1368 Wm^{-2} of solar radiation intensity [1]. This solar radiation power, crossing the atmosphere, is strongly attenuated by many scattering and absorption processes. The intensities absorbed by oceans and continents are respectively 170 Wm^{-2} and 180 Wm^{-2} [1], which integrated over the entire surface give a total absorbed power of 90 PW [1] (65 PW only for water [1]). Such an endless (on a human scale) huge power supply is 6000 times higher than the recent power demand (15 TW). Land and ocean phytomass is sustained by photosynthesis, which is powered by only 1% of the solar flux reaching the Earth surface [1]. Similarly, air circulation and winds utilize 1% of the same flux [1]. Then, about one fourth of the total power absorbed by seawater sustains the global water cycles [1]. Therefore Sun power, in addition to constitute a renewable energy source itself, feed the processes in the cycles at the bases of numerous renewable supplies such as hydro-power and wind energy. An overview of the solar energy transformations is shown in Fig. 1.1.

The following section provides general description and the relevant issues of the currently most effective renewable energy technologies.

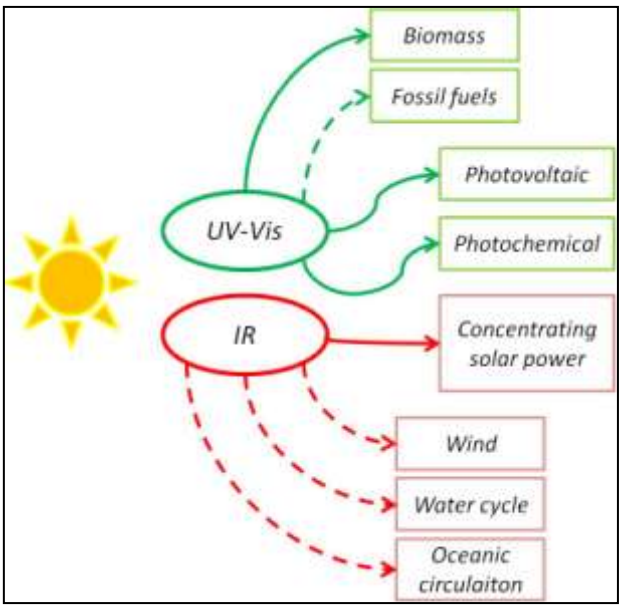

Fig. 1.1 *Direct (full line) and indirect (dashed line) transformations of solar energy*

1.3.a - Hydro-power

Hydro-power generation is based on the conversion of the mechanical potential energy of water stored in large high basins firstly into kinetic energy (falling water) and finally by turbines, into electricity. Systems linked to huge water artificial reservoirs have capacities ranging from few mega-watts to several gig-watts. Few kilo-watts up to some mega-watts can be produced for local demand by small systems not involving water reservoirs. Hydro-electric generation efficiency reaches 90% [1], dwarfing thermonuclear (33%) [1]. For this reason, 16% of the global electricity demand is covered by hydro-power [3], which is the largest exploited source. Moreover the systems can be designed either to generate power or to store energy, pumping water to high levels. Hydro-power related drawbacks are:

- Vulnerability to climate changes affecting water cycle.
- Invasiveness in terms of used area by water reservoirs.

Nevertheless hydro-power stations, in parallel, can provide irrigation water and navigation advantages.

1.3.b - Wind

Wind kinetic energy is transformed into electricity by horizontal axis turbines kept at elevated heights to face not dragged fast wind (operating speed ranges from 7 – 15 m/s [1]). Since wind must keep on flowing after crossing the turbine blades to carry on their rotation, the theoretical generation efficiency limit is 60% [1], yet operating efficiencies are between 30% – 40% [1]. Installation and dismantling are cheaper and faster the relative operations of any other electric technology [1]. Wind is the world fastest growing technology, whose capacity reached 38 GW in 2009 [1]. Recent estimates indicates that a feasible turbines networks could provide an electricity budget forty times bigger than the amount currently consumed [1]. The biggest disadvantages of connecting wind energy to the present grid are intermittency and instability of supply.

1.3.c - Concentrating Solar Power

Solar radiative energy can be indirectly converted into electricity concentrating diluted sun light, by means of wide reflectors, onto a small absorbing area to obtain at least 300 °C for turbine moving steam generation. Such systems can even use waste heat

from power generation to desalinate seawater. A wide variety of concentrating solar power (CSP) stations exists, using different collecting systems (parabolic trough concentrators, solar towers, dish collector with Stirling engines etc...) and heat absorbing fluids, which, depending on the properties, could store the accumulated thermal energy for long time. CSP capacity is growing rapidly, in fact 1 GW is under construction and 14 GW more are planned through 2014 [1]. CSP can be operated economically on large scale only within the large sun-belt covering US south-west, southern Europe, North Africa and Middle East. The cost of raw materials for construction is not rising like fossil fuels, however the main drawback is the large quantity of water (scarce in sun-belt area) necessary for cooling the systems and cleaning the collectors. Because of all these issues, CSP electricity is twice more expensive than wind electricity.

1.3.d - Photovoltaic

Electric power generation by means of photo-voltaic (PV) systems (both inorganic and organic) is based essentially on irradiation induced creation of electric current in a properly engineered stack of suitable materials. This process happens because, at small scales the photo-generated charges are transferred from one material to another to end in the total electric flow output. Nowadays 25 GW of PV capacity is installed, covering only 0.55% of the total electricity supply [1]. Nonetheless PV market yearly growth is about 40% [1], having the technical and economic potential to satisfy high shares of electricity demand (70% in US and even more in EU [1]).

PV capacity is intrinsically de-localized and can provide off-grid energy supply in remote or developing regions [2]. Currently the leading technology is crystalline silicon solar panels (80% of the market [1]) followed by thin-film panels (mainly hydrogenated amorphous silicon and cadmium telluride as absorber layers). The applied research is now focused on the development of novel technologies, based either on earth-abundant and non-toxic metal oxides or on nano-structured absorber layers, exploiting the peculiar phenomena at the quantum scale, like quantum dots, plasmonics and other systems.

1.3.e - Solar Fuels

Solar fuels are solid, liquid or gaseous compounds and substances able to release chemical energy through a red-ox reaction with an oxidizer (generally O_2). This

reaction can occur as combustion or as electro-chemical oxidation of the fuel on one electrode in a fuel cell [2]. By means of combustion electrical or mechanical energies can be obtained operating burning systems on a thermal cycle (gas turbines and internal combustion engine); while fuel cell transforms chemical energy into electricity in a more controlled way, not operating on a thermal cycle, thus having higher performance efficiency (theoretical maximum value 80%) [2]. Fuel cells can be automotive (80 – 130 KW [2]) for transportation or stationary (2 – 250 KW [2]) for industrial or residential uses. Solar fuels production and regeneration are sustained by sun radiation and heat (direct production) or by electricity generated by CSP, PV or wind plants (indirect production). The main form of solar fuels is biomass, formed by natural photosynthesis. Bio-fuel produced by biomass conversion surely cannot substitute fossil fuels in a highly industrialized economy due to extremely low efficiency of biomass production and conversion and mainly owing to the unsustainable competition with food production (wide fertile land employed for biomass cultivation) and to environment damages (deforestation for new biomass cultivation lands) [2].

Hydrogen (H_2) is a promising solar fuel due to the following reasons:

- sustainable production;
- environmentally friendly if used in fuel cells (whose by-products are heat and water);
- free enthalpy higher that gasoline (141.5 $MJ \cdot Kg^{-1}$ vs. 45.7 $MJ \cdot Kg^{-1}$);
- high versatility use.

Renewable H_2 can be produced by solar energy by different methods [2]:

- Water thermolysis by CSP: H_2 is obtained by H_2O solar thermo-chemical splitting with the aid of catalytic metal oxi-reduction.
- Carbo-thermal reduction of metal oxides: carbonaceous materials are used as reducing agents to produce metal from oxides and CO. Both these substances are further processed to produce H_2.
- Methane re-formation: methane is converted in CO_2 to extract H_2. This endothermic reaction (that can be powered by solar heat) ideally upgrade the calorific value of methane by more than 25%.
- Thermo-chemical conversion of biomass: it consists in solar heat biomass gasification and pyrolysis whose product is H_2.
- Water electrolysis: renewable electricity sources such as PV and wind provide energy to obtain H_2 from electrolytic cells.

It has been proven, on laboratory scale, significant efficiencies for most of the above H_2 production methods, yet their scaling up at industrial levels is still a far achievement.

1.4 - Perspectives and outlooks

From the overview on the non-renewable energy resources it can be surely asserted that their power potentials are high enough to not consider their ultimate depletion a very urgent issue. Whereas the vast majority of scientific evidence indicates that most of the recent observed warming of Earth and related forthcoming environmental catastrophes are being caused by increased concentrations of greenhouse gases released by fossil fuels utilization [2]. Therefore the global energy consumption upgrade to low carbon emission energy supply is a really compelling goal. Owing to the fact that further large increase of hydro-power share is not feasible for geographic and environmental reasons, such a target can be accomplished further spreading wind and solar power supplies and, above all, planning wisely their high penetration in the future energetic infrastructures. Since the extracted energy form from wind and solar irradiation is basically electric current, our demand shares should be revised, strongly enhancing the role of electricity. An appropriate strategy could be developing electric private transports and efficaciously adapting trades to railway transportation (electric carrier). High renewable electricity exploitation in turn, means also matching wind and solar power plants to the grids.

The current grids topology, structure, organization and operations put relevant barriers to this high penetration for the following reasons [2]:

1. CSP and PV power is intermittent due to day/night cycle, thus related plants can not constitute base-load generators (generators that run all time to provide the minimum constant power supply).
2. Wind and solar irradiation intensities are subject to short time scale irregularities which are deleterious for grid stability. Disturbances of generators synchronization causes harmful grid faults..
3. Erroneous forecast of wind outages leads to supernumerary conventional base-load plants (coal and nuclear) activation. Over-scheduled plants causes high start-up costs.
4. Renewable energies over production (i.e. wind in spring time and sun irradiation during the summer) press either uneconomic partial loading of base-load conventional plants or curtailment of the renewable supply. The last constraint reduces the net capacity factor of the installed renewable generators, increasing the overall cost of the energy.

For almost every former problem a clear solution ideally exists [2] and the succeeding list orderly catalogues them:

1. Conventional base-load plants complete substitution is the hardest and less feasible goal, unless revolutionary breakthroughs in energy storage technology occur;
2. Special processors, which are able to execute protection schemes in microseconds, ought to be integrated in the network. Well designed sensors could also detect disturbances and can signal digitally for grid clusters to be temporary isolated;
3. Improvement of the weather forecasting techniques combined with fast communications decreases over-scheduling risk. Moreover expanding the use of flexible gas turbines guarantees a high grid responsiveness;
4. The wastefulness related to renewable energy overproduction could be avoided reshaping the demand trend actively involving the customers. Another strategy can be sharing the supply on large scale to spread it on a bigger market or to store it as potential energy in far hydro-electric plants. Finally, a further solution should be the addition of new loads as hydrogen production, process heating and plugging of electric vehicles.

The former strategies fulfilment (especially point 4) for a higher renewable supply penetration requests a deep reorganization of the existing grids into what is known as "*smar*t" grids [2].

Conventional grids are structured as centralized networks where big generators (hubs) are connected to high voltage transmission lines, which in turn, diffuse energy to the medium and small customers (nodes) through tree-like distribution lines [2]. A smart grid envisages not only a centralized sub-mesh, functioning as a backbone network, but also a bi-directional distribution lines arranged as clustered knits (micro-grids) of peripheral nodes [2]. In this way the smart grid structure is similar to an ecosystem net, and, according to the pioneering theoretical studies of Baran on complex nets [4], comparable to Internet structure.

1.5 - Solar cells fundamentals

A solar cell is a device that basically converts solar radiation energy to chemical energy, from which electrical energy is then harvested. In a semiconductor, kept at a fixed temperature, chemical energy is produced by the generation of electron-hole pairs, induced by the absorption of electro-magnetic radiation. In a semiconducting material, not invested by light, the electrons are distributed in the band states according to the Fermi distribution $f_e(E)$ with the Fermi energy E_f. The position of E_f in respect to the bands edges depends on the material, being intrinsic or doped [5]. On the other hand, holes distribution, in the dark, follows the complementary distribution 1- $f_e(E)$, which has the same Fermi energy E_f as for electrons. Therefore the density of (free) electrons n^0_e in the conduction band is [5]:

$$n_e^0 = N_C \, e^{-\left(E_C - E_f / KT\right)} \tag{1.1}$$

where N_C is the effective density of state in the conduction band and E_C is the conduction band edge level. The density of (free) holes in the valence band is instead [5]:

$$n_h^0 = N_V \, e^{-\left(E_f - E_V / KT\right)} \tag{1.2}$$

where N_V is the effective density of state in the valence band and E_V is the valence band edge level.

Being the semiconductor at equilibrium, it follows from Eq. (1.1) and Eq. (1.2) that:

$$n_e^0 \cdot n_h^0 = {n_i}^2 = N_C N_V \, e^{-\left(E_g / KT\right)} \tag{1.3}$$

where E_g is the band gap and n_i is the intrinsic electron density.

When the material is invested by photons from the sun, whose energy is higher than E_g, further electrons are promoted from the valence band to the conduction band, leaving in the former an increased number of holes. The mean energies of these photo-generated electrons and holes are respectively [6]:

$$\langle E_e \rangle = E_C + {}^3/_2 \cdot KT_S \tag{1.4-a}$$

$$\langle E_h \rangle = E_V - {}^3/_2 \cdot KT_S \tag{1.4-b}$$

where T_S is the temperature of the sun.

However, due to collisions with the lattice, the energy distributions of photo-generated electrons and holes change very rapidly. In fact, immediately after their generation, the electrons and holes mean energies become respectively [6]:

$$\langle E_e \rangle = E_C + {}^3/_2 \cdot KT_0 \tag{1.5-a}$$

$$\langle E_h \rangle = E_V - {}^3/_2 \cdot KT_0 \tag{1.5-b}$$

being T_0 the environment temperature. This means that the charge carriers, during the thermalization time, establish thermal equilibrium with the lattice, even for continuous irradiation. Hence, their steady-state energy distributions must be Fermi distributions at T_0. By irradiation, both n_e and n_h are greater than the relative values in the dark n_e^0 and n_h^0, thus:

$$n_e \cdot n_h > {n_e}^0 \cdot {n_h}^0 = {n_i}^2 \tag{1.6}$$

In this situation, the Fermi energy of electrons, E_{fc} should be closer to the conduction band, whereas, the Fermi energy of holes E_{fv} should stay closer to the valence band. Consequently, electrons and holes occupations in the bands now follows two separate Fermi distributions $f_e(E)$ and $f_h(E)$. As in Eq. (1.1) and Eq. (1.2), the densities of electrons in the conduction band and in the valence band are, under illumination [6]:

$$n_e = N_C \, e^{-\left({}^{E_C - E_{fc}}/_{KT}\right)} \tag{1.7-a}$$

$$n_h = N_V \, e^{-\left({}^{E_{fv} - E_V}/_{KT}\right)} \tag{1.7-b}$$

$$n_e \cdot n_h = {n_i}^2 \, e^{-\left({}^{E_{fc} - E_{fv}}/_{KT}\right)} \tag{1.7-c}$$

The previously mentioned Fermi distributions contradict each other in the energy range between E_{fv} and E_{fc}, because the charges occupation, in this range, is governed by kinetics (electron-hole recombination) [6].

In order to obtain energy from the illuminated semiconductor, it is necessary to extract the photo-generated pairs before their recombination. The energy carried by each pair is composed by one entropic part, i.e. heat, and by one entropy-free part, called Free energy, which constitutes the useful electric energy per pair [6]. Free energy is defined as $F = E - T \cdot S$, being S the entropy. With the extraction of dN_e electrons and $dN_h = dN_e = dN$ holes, the Free energy removal from the material is [6]:

$$dF = dF_e + dF_h =$$

$$= -S_e dT - p_e dV + \mu_e dN_e - e\varphi dN_e - S_h dT - p_h dV + \mu_h dN_h + e\varphi dN_h \tag{1.8}$$

In the expression above p is pressure, V the volume, μ the chemical potential, e the fundamental charge and φ the electrical potential. Since during the pairs extraction, from the illuminated material, volume and temperature are kept constant, Eq. (1.8) becomes:

$$dF = (\mu_e - e\varphi)dN_e + (\mu_h + e\varphi)dN_h = (\zeta_e + \zeta_h)dN \tag{1.9}$$

where ζ are the electro-chemical potentials. From the calculations made by Sacker and Tetrode [6] on the energy per particle E/N, it results that $\zeta_e = E_{fc}$ and $\zeta_h = E_{fv}$. Therefore, electrical power can be obtained from an illuminated semiconductor because the Fermi energy is split in two parts, that are E_{fc} and E_{fv}. This separation does not occur, for example, in illuminated metals, from which only entropic (thermal) energy can be obtained. The already described conversion of solar irradiation energy in electrical energy, by the solar cell, is affected by energy losses, hence it is characterized by a certain efficiency. The first energy loss is the fast thermalization process involving the photo-generated pairs, whose mean energy decreases from $E_g + 3 \cdot KT_s$ to $E_g + 3 \cdot KT_0$. The thermalization of charge carriers provides heat to the lattice, thus creates entropy. The second energy loss is the wastefulness of not absorbed photons with energy less than E_g.

In order to calculate the other efficiency decreasing factors, it is straightforward to consider a situation in which the former energy loss mechanisms cannot occur. This situation is ideally achieved shining the semiconductor with monochromatic photons at $E = E_g + d\hbar\omega$. Moreover, for now, we consider only radiative pairs recombination, maximal light trapping and incident solid angle ($\Omega_S = 6 \cdot 10^{-5}$) [6] equal to the emission one (Ω_E). When the illuminated material is in equilibrium at T_0 with the solar radiation and no pairs are extracted, the emitted and absorbed photon current densities (derived from the generalized Planck radiation law [6]) are the same:

$$J_{emi} = \left[\Omega_E / 4\pi^3 h^3 c^2\right] \cdot \left[E_g{}^2 d\hbar\omega \Big/ e^{\left(E_g - \mu_{oc}\right)/KT_0} - 1 \right] =$$

$$= \left[\Omega_S / 4\pi^3 h^3 c^2\right] \cdot \left[E_g{}^2 d\hbar\omega \Big/ e^{E_g/KT_S} - 1 \right] = J_{abs} \tag{1.10}$$

From which it results that:

$$\mu_{oc} = E_{fc} - E_{fv} = E_g \left(1 - {}^{T_0}/_{T_S}\right) \tag{1.11}$$

Eq. (1.11) means that, at open circuit (oc) conditions, the chemical energy per pair is always less than the band gap. This quantity corresponds to the voltage difference V_{oc} between the poles of the cell. From this formula, it can be calculated the efficiency of the conversion of solar radiation energy (in this case $E = E_g$) in chemical energy:

$$\eta = {}^{\mu_{oc}}/_{E_g} = 1 - {}^{T_0}/_{T_S} \tag{1.12}$$

Eq. (1.12) is the Carnot efficiency [6] (entropy is, for now, kept constant because of lack of pairs thermalization). Nonetheless, there are some non-ideality factors that affect Eq. (1.11) further decreasing the efficiency η. The first is the spontaneous photon emission into a solid angle $\Omega_E > \Omega_S$ (up to 4π). The second factor is the incomplete light trapping, which diminishes the absorbed photon current J_{abs} by a factor B. Finally, being respectively R_r and R_{nr}, the radiative and non-radiative recombination rates, the emitted photon current J_{emi} decreases by a factor R_r / (R_r + R_{nr}) (defined as "quantum efficiency" QE). Thus, equating the new J_{abs} and J_{emi} [7]:

$$\mu_{oc} = E_g \left(1 - {}^{T_0}/_{T_S}\right) - KT_0 \left[ln\left({}^{\Omega_E}/_{\Omega_S}\right) + ln\left({}^{1}/_{B}\right) - ln(QE)\right] \tag{1.13}$$

All these three factors belong to entropy-generator processes.

To harvest electric energy, the cell cannot operate at open circuit condition. A charge current J_{eh} (equal to electrons and holes currents) has to be extracted. Such a current is given by [6]:

$$J_{eh} = J_{abs} - J_{emi} \tag{1.14}$$

Under illumination $n_e \cdot n_h > {n_e}^0 \cdot {n_h}^0 = {n_i}^2$ thus [6]:

$$J_{emi} = J^0_{emi} \cdot \left({}^{n_e \cdot n_h}/_{{n_i}^2}\right) \tag{1.15}$$

where ${J^0}_{emi}$ is the emitted photon current in the dark at equilibrium.

Combining Eq. (1.15), Eq. (1.16) and Eq. (1.7) it results that [6]:

$$J_{eh} = J_{abs} - J^0_{emi}\, e^{({}^{\mu}/_{KT})} \tag{1.16}$$

In Fig. 1.2 the current of extracted chemical energy ($J_{eh} \cdot \mu$) is, for a given μ, the orange rectangle. Therefore at operative conditions, every extracted pair provides an

electrical energy μ, always smaller than μ_{oc}. The useful voltage difference V, between the cell contacts, is μ. Solar cells, under illumination, always work at J_{eh} and V for which the provided electrical power $P = V \cdot J_{eh}$ is at its maximum value $P_{max} = V_{max} \cdot J_{eh,max}$. Consequently, the conversion of solar radiation energy in electrical energy is performed by the cell with an overall efficiency:

$$\eta = {}^{\mu_{max}}/_{E_g} < {}^{\mu_{oc}}/_{E_g} \tag{1.17}$$

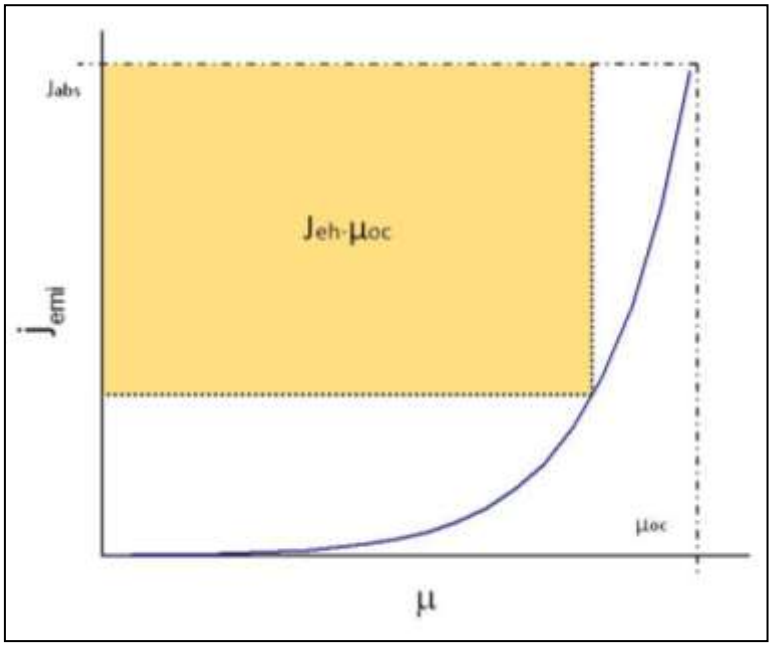

Fig. 1.2 *Emitted photon current J_{emi} vs. electron-hole pair chemical potential μ. The orange rectangle is the current of extracted chemical energy for a given μ.*

If now we consider the real case of a broad spectrum incident radiation, thermalization of hot charge carriers and wastefulness of sub-gap photons will contribute to a further degradation of device efficiency. Moreover, defects such as non-ideal contacts and cell structural imperfections add to these detrimental effects.

Each of these efficiency loss mechanisms involves one conversion step of the entire conversion chain, thus, in general the total cell efficiency is:

$$\eta_{Tot} = \eta_{abs} \cdot \eta_{th} \cdot \eta_A \cdot \eta_D \tag{1.18}$$

where η_{abs} accounts for sub-gap incident photons loss; η_{th} considers the thermalization; η_A comes from Eq. (1.17), that is, the maximum useful pair chemical energy is smaller than the average thermalized pair energy. Finally, η_D comprises all the cell fabrication defects. The product $\eta_{abs} \cdot \eta_{th}$ is a peaked function of E_g, since there is a trade-off between the amount of radiation energy loss due to thermalization and the loss caused by the transmission of sub-gap photons. Considering the solar radiation spectrum at sea level, $\eta_{abs} \cdot \eta_{th}$ is maximum for E_g ranging from 1 eV and 1.6 eV.

It has been remarked several times that to obtain electrical power from an illuminated cell, it is necessary to collect separately the photo-generated electrons and holes, which have to maintain their chemical potential up to the extraction contacts. Therefore a solar cell cannot consist of a single n or p-type semiconductor, since its symmetry does not provide any preference for the transport of electrons in one direction and holes in the opposite direction. For this porpoise, charge carriers selective "*filters*" are needed just before the opposite contacts. Such "*filters*" can be created taking advantage of bands structure asymmetries of different materials. The general solar cell structure has to be as shown in Fig. 1.3. In this structure the typical modulation of the band gap through the device creates, on the opposite sides, two barriers, which allow the transmission, from the absorber layer, of only one kind of charge carrier, i.e. electrons or holes.

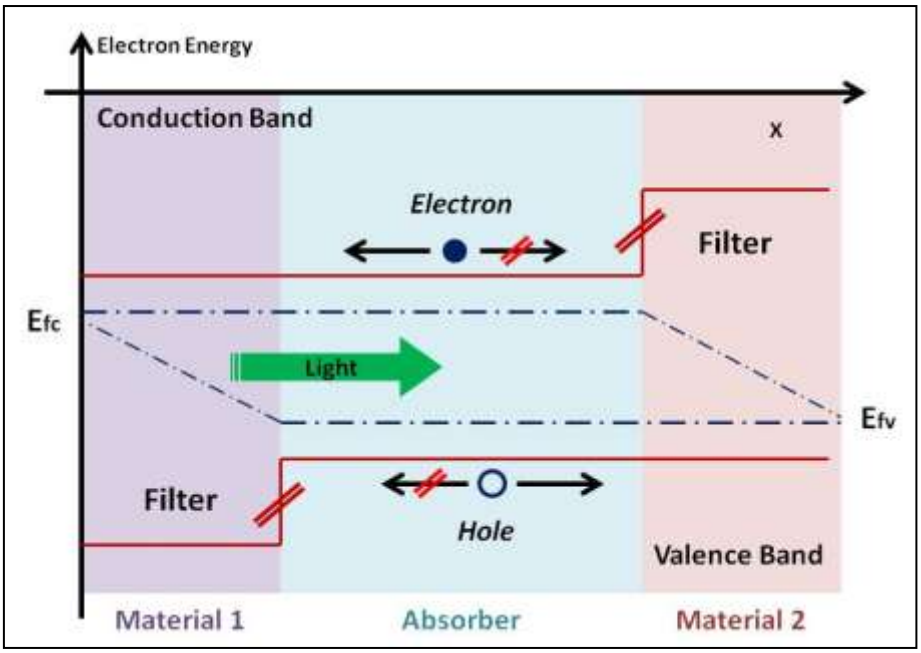

Fig. 1.3 *General solar cell structure.*

In practice such a structure can be reproduced in different kind of cells as schematized in Fig. 1.4.

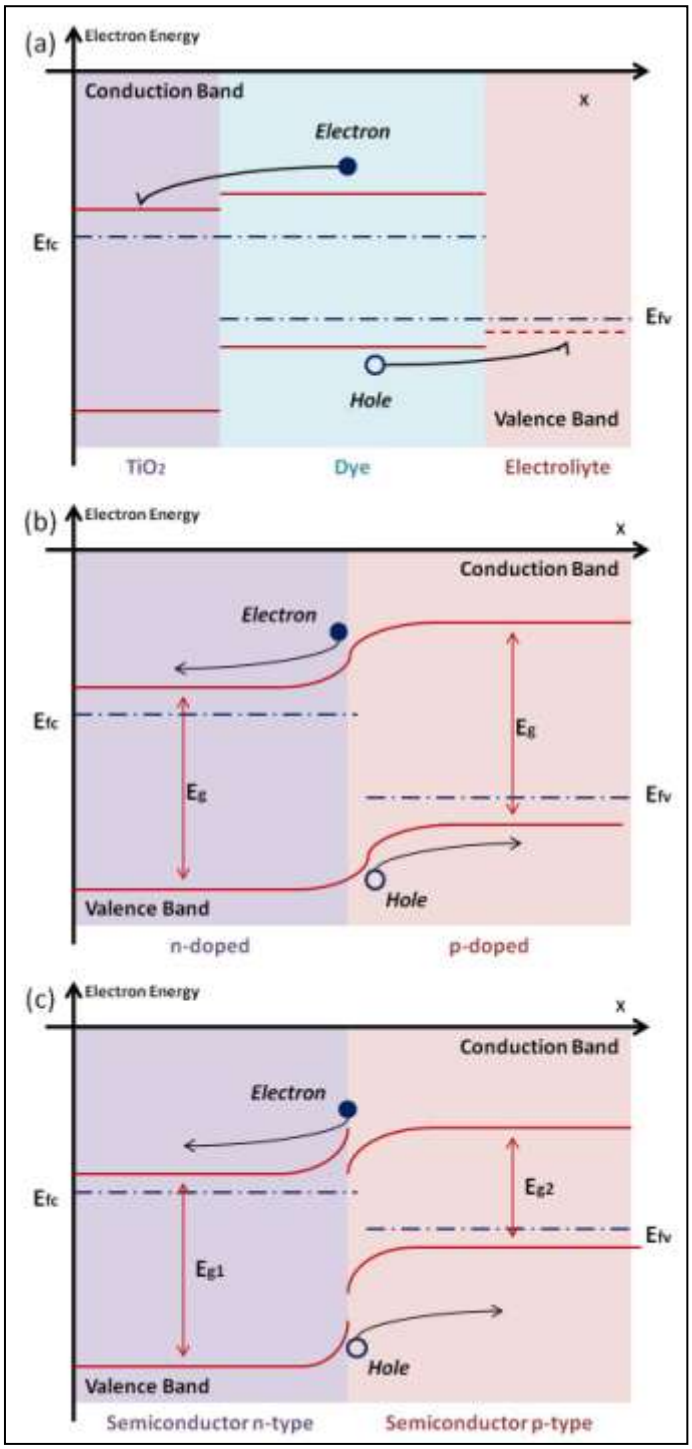

Fig. 1.4 *(a) Dye solar cell; (b) p-n homo-junction; (c) p-n hetero-junction.*

In order to gain a deeper insight in the issue of solar cells efficiency improvement, we have to look back at Eq. (1.13) and Eq. (1.18) and try to be more quantitative. Schockley and Queisser calculated that an ideal single junction solar cell with maximum *QE* and light trapping factor *B*, made up of materials with 1 eV < E_g < 1.6 eV (crystalline silicon and gallium arsenide), has an efficiency of 33%. This value could be, in principle, increased up to 40% restricting the emission angle Ω_E to Ω_S. Hence, in general, the biggest efficiency loss is owing to thermalization of hot photo-generated pairs and lack of sub-gap photons absorption. To partially unlock such a big conversion efficiency potential it is necessary to fabricate a solar cell with an overall decreasing graded band gap. In this way, the high E_g front of the device, facing as first the incoming radiation, will absorb only the photons whose energy is very similar to the high E_g (blue-green light). The generated pairs, in turn, will occupy energy states essentially adjacent to bands edges, thus they cannot thermalize. The lower energy light (yellow-red-NIR) entirely transmitted through the first cell layer will be then absorbed by the next layer whose band gap is now well matched with the incoming light. Again the generated pairs will not have the possibility to thermalize. It has been theoretically and experimentally proven that the "*tandem-cell*", shown in Fig. 1.5, fulfill this aim, increasing the efficiency up to 40% (double junction cell) or even 60% (six junctions cell).

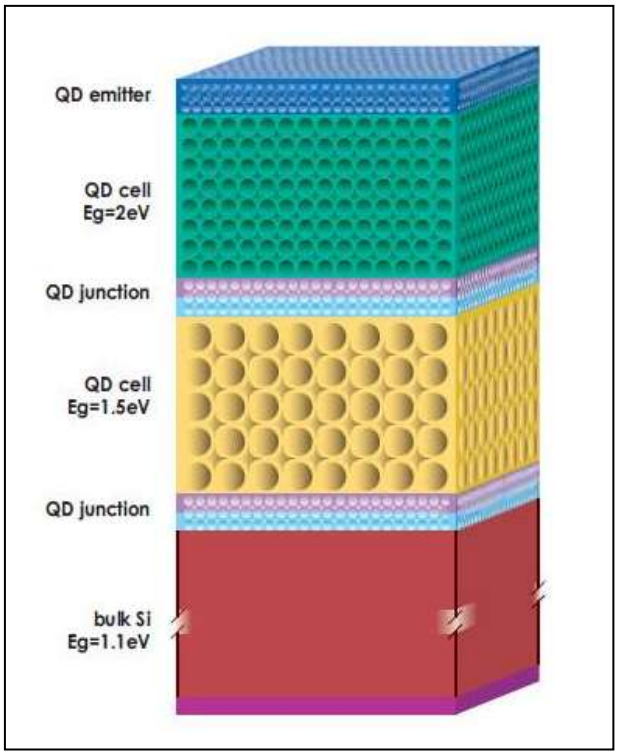

Fig. 1.5 *All-silicon tandem cell based on SiO_2 quantum dots (QDs) super-lattices (taken from Ref. [8]).*

A less efficient alternative to this solution is the utilization of solar cells containing materials absorbing sub-gap photons (up-converters or intermediate band layers) or "splitting" an high energetic photon (UV-blue-green) in many lower energy photons, better matched with the device band gap (down-converter). Most of these kind of innovative cells exist only as proof of concept devices, while the most successful tandem cells, in spite of showing astonishing performances in laboratories, are still far from wide spread deployment in PV global market.

In order to spread PV energy supply on large scales it is, however, important and urgent to decrease the price of solar cells, using a smaller amount of precious material, as crystalline silicon. As regards c-Si cells, advances in smarter fabrication steps (casting, cutting, etc...) recently heavily decreased solar module prices. Nevertheless, utilization of novel materials as thin films (less than 100 nm) is envisaged as a promising alternative. Some of these materials have direct band gaps, thus higher absorption coefficient and *QE* compared to crystalline silicon. The former property allows the use of much thinner absorber layers without significant absorption losses. Unfortunately, the set of alloys with the best (for now) recorded performances embraces materials, as CIGS (copper-indium-gallium-sulfur) and CdTe (cadmium telluride), containing rare or toxic elements. Therefore developing non-toxic and Earth-abundant material based cells is a compelling aim for applied physics research. Among the wide ensemble of novel candidates (organic compounds, perovskites, oxides, etc...), metal oxides, such as cuprous oxide (Cu_2O), are of paramount interest. Apart from the above mentioned innovative materials, crystalline silicon, micro-crystalline silicon (μc-Si) and hydrogenated amorphous silicon (α-Si:H) based cells could also have great efficiencies (for example c-Si cells could reach 40%) if light trapping and management inside the devices are successfully accomplished.

To sum up, there are three possible strategies to achieve super high efficiency cells and/or extremely cheap (with efficiencies bigger than 10%) solar cells:

1. Enhance c-Si, μc-Si and α-Si:H based cells efficiencies by means of innovative and yet not fully explored light-matter interactions, which can allow to better engineer the flow of light inside the solar cell.
2. To develop and to improve cheap thin-film solar cells employing high performances non-toxic and abundant materials. Junctions based on these materials can be integrated in multi-junctions cells if the absorber band gap of the former junction does not match the solar spectrum.
3. To fabricate and to improve multi-junction (tandem) solar cells, which are expensive but ultra efficient. The costs can be constrained to reasonable values exploiting solar irradiation concentration on small area devices.

1.6 - Outline of the work

Taking inspiration from the issues discussed in the points *1.* and *2.*, with the research activity carried out during my Ph.D. studies, I provided the following contributes:

1. Research and development of a simple synthesis of semiconductor nano-structures, with proper morphologies and shapes to provide efficient radiation harvesting for solar cells. Moreover, it has been undertaken an examination of novel nano-structures geometries and the related light-matter interactions.
2. Investigation of some key features of physical and chemical deposition methods, suitable for the synthesis of cuprous oxide thin films for cheap and green solar cells. Since the efficiency of Cu_2O based hetero-junctions has not yet surpassed 6% [9], it has been also endeavored to improve the material properties by means of doping with a wide variety of non-toxic and Earth-abundant elements. In particular, the doping has been fulfilled employing deeply different approaches.

The first subject is discussed in chapter 2. Firstly it is provided a review on the light trapping principles and approaches, unfold and employed since the beginning of the PV era (sections 2.1, 2.2 and 2.3). After a brief overview on the most promising nano-structures scalable fabrication techniques (section 2.4), it is reported my experimental activity aimed at seeking and describing efficient light scattering and trapping in silicon nano-wires (section 2.5) and novel interconnected silicon nano-structures (section 2.8), respectively fabricated by catalyzed CVD and pulsed laser induced dewetting.

The nano-structures synthesis by pulsed laser irradiation, the related characterizations and the investigation on the silicon NWs optical properties was performed at the MATIS - IMM laboratories of the University of Catania (Italy).

The topic of chapter 3 is Cu_2O thin films for photovoltaic applications. The first section reports the state of the art of Cu_2O-based cells and the issues concerning the drawbacks and their possible solutions. Section 3.2 is an overview on the structural, optical and electrical properties of the bulk material. The summary of the principal methods for the deposition of thin films and their properties is presented in section 3.3. Section 3.4 deals with the various effects that doping can have on the material characteristics. The second part of the chapter presents the experimental results. Specifically, one physical deposition method, RF magnetron sputtering (section 3.5), has been compared with one chemical technique, spray pyrolysis (section 3.7), providing the key features of both the synthesis methods.

Moreover, two deeply different doping techniques are investigated:

1. out -of-equilibrium incorporation of nitrogen atoms in sputtered films by ion implantation (section 3.6);
2. Zn, Mg and Ca doping, carried out during the spray pyrolysis film growth (section 3.8).

Furthermore, the variety of dopants permitted to examine various aspects of the doping effects on the Cu_2O physical properties, encompassing structural, optical and electrical modulation.

The synthesis of Cu_2O thin films by RF magnetron sputtering, nitrogen doping by ion implantation and all the related characterizations, were performed at the MATIS - IMM laboratories of the University of Catania (Italy).

The deposition of Cu_2O samples by ultra-sonic spray pyrolysis, Zn, Mg and Ca doping with the relative analyses were carried out during the eight months richly spent at the laboratories of CENIMAT and of the "Departamento de Ciencias e Tecnologia dos Materiais" at the Nova University of Lisbon (Portugal).

Bibliography

[1] Energy for a Suitable World: From the Oil Age to a Sun-Powered Future - N. Armaroli; V. Balzani - Wiley-VCH (2011)

[2] Fundamentals of Materials for Energy and Environmental Sustainability - Edited by D. S. Ginley & D. Cahen - Cambridge University Press (2012)

[3] Key World Energy Statistics - International Energy Agency (2013)

[4] Link; La Nuova Scienza delle Reti - A. L. Barabasi - Einaudi (2008)

[5] Dispositivi a Semiconduttore; Comportamento Fisico e Tecnologico - S. M. Sze - Hoepli (1991)

[6] Physics of Solar Cells; From Principles to New Concepts - P. Würfel - Wiley (2005).

[7] A. Polman; H. A. Atwater - Nature Materials; Vol. 11 (2012).

[8] ARC Photovoltaics Centre of Excellence - Annual Report (2009)

[9] T. Minami, Y. Nishi and T. Miyata; Applied Physics Express **6**, 044101 (2013).

2 - LIGHT TRAPPING FOR PHOTOVOLTAICS

2.1 - Antireflection coatings

In section 1.5 it has been stated that, in a solar cell, non-efficient light trapping causes a reduction of the short-circuit current J_{sc} and a decrease of the open circuit voltage V_{oc}, leading to an overall shrinkage of the cell efficiency. Non-efficient light trapping occurs in the cell, when some photons with energy above the material optical band gap E_g, are lost before their absorption in the active layer of the device. For example, since at the air/cell interface there is an index of refraction discontinuity, a fraction of this incoming photons is reflected back to the air (see Fig. 2.1). Moreover photons with energy slightly higher than E_g, transmitted through the air/cell interface, can escape from the cell front or from the back surface of the cell if its thickness is not sufficient to ensure a high absorption probability. In fact, when the cell thickness is comparable or less than the penetration depth $1/\alpha$, being $\alpha(\hbar\omega)$ the absorption coefficient, the absorption probability for a straight crossing photon is smaller than 40%.

The photon density of states (PDOS) in a medium is proportional to square of the refraction index n^2 [1], thus, for a certain photon energy $\hbar\omega$, the materials of a cell can accommodate more photon modes compared to the air, which has always a smaller n. Consequently, all possible incident photons (coming from the hemispherical solid angle 2π) can cross the cell surface to occupy one of the material photon states, without violating the Second Principle of Thermodynamics [2]. This fact makes suppression of surface reflection theoretically possible by means of proper refraction index tuning of the cell front material. Indeed one of the earliest light trapping approaches is the growth of antireflection coatings (ARCs) on the cells surface. Such approach is based on the ray-optics interference effects caused by the interaction of light with a stack of layers coating the cell surface.

Considering unpolarized light (as sunlight is) normally incident on a single ARC layer with thickness $d_1 = \lambda_0/(4 \cdot n_1)$ (where λ_0 is the light wavelength and n_1 the refraction index of the layer) the light reflected from the coating/cell interface will go back to the air with a phase change of π. In this way, the ray will undergo destructive interference with the incident ray and the total reflection coefficient of the coated cell surface will be [3]:

$$R_{single}(\lambda_0) = \left({n_1}^2 - n_{air} \cdot n_{cell} \Big/ {n_1}^2 + n_{air} \cdot n_{cell} \right)^2 \tag{2.1}$$

which is null for:

$$n_1 = \sqrt{n_{air} \cdot n_{cell}} \tag{2.2}$$

Unfortunately, ARC layers thickness is optimized only for one wavelength λ_0. Since the sun spectrum is broad, it has to be considered, as reported in Eq. (2.3), $R(\lambda)$ averaged on the sun wavelength range. Moreover such average calculation has to take into account the spectral response of the cell $S(\lambda)$.

$$\bar{R} = \int_{\lambda_1}^{\lambda_2} S(\lambda)\, R(\lambda) d\lambda \tag{2.3}$$

The optimum design of an antireflection stack coating is numerically calculated by searching a minimum for $\bar{R}$ [3].

Antireflection coatings enhance the light transmitted through the air/cell front interface, but do not change the rays path inside the cell, thus do not solve the problem of the large loss of those photons whose energy is just above E_g. To overcome this drawback, it is necessary to redesign the (coated) cell surface into a more complex morphology, in order to exploit those light diffusion and scattering mechanisms which enhance the rays path inside the cell.

2.2 - Light trapping by surface texturing in the ray-optics regime

Consider a slab of transparent (low α) material placed in a region filled of black-body radiation. If this slab is in equilibrium with the external radiation the internal electro-magnetic energy intensity is [1]:

$$I_{int} = \left({\hbar\omega^3}\Big/{e^{\left({\hbar\omega}/{KT}\right)} - 1} \right) \cdot \left({n^2}/{4\pi^3 {c_0}^3} \right) \cdot d\omega \cdot d\Omega \tag{2.4}$$

where c_0 is the light speed in vacuum, n is the refractive index of the slab material and $\hbar\omega$ is the photon energy. This expression differs from the external energy intensity I_{bb} by the factor n^2. Therefore it can be stated that [1]:

$$I_{int}(\omega) = n^2 I_{bb}(\omega) \tag{2.5}$$

Since the slab is transparent Eq. (2.5) holds separately for every frequency ω.

If the external radiation has not the isotropic distribution of the black-body, the behaviour of the internal light may not be ergodic, hence Eq. (2.5) is not valid. For example, in a planar slab the refracted photons keep memory of the incident angle (by means of the Snell's Law) and Eq. (2.5) breaks down. Nevertheless, if the surface of the slab is textured in such a way that the collimated incident rays, undergoing random refractions and total reflections, are able to lose any correlation with the incidence angle, the internal radiation distribution will be isotropic. When a textured surface has this kind of geometry, it is defined as an ergodic surface and Eq. (2.5) is correct.

Some random textures, as resulting from proper chemical etching or lithographic patterning, could approach this ideal property. Even slabs with ordered surface textures can show this characteristic, because light randomization can occur on successive internal reflections and can result from the spatial average over the illuminated area [1].

In conclusion, if the morphology of the textured slab surface ensures light ergodic behaviour inside the material, Eq. (2.6) holds also for collimated incident light. In particular, if the back surface is covered with a perfectly reflecting film, the external radiation will be confined only on one half of the region. This leads to a concentration factor of *2*, thus [1]:

$$I_{int}(\omega) = 2n^2 I_{inc}(\omega) \tag{2.6}$$

Eq. (2.6) is valid if the wave optical effects can be ignored, that is, if the slab thickness is higher than $\lambda/2n$.

If now we consider that the photons, isotropically distributed (over 4π) inside the slab, can be absorbed (the relative absorption coefficient should be low if the previous results has to be still valid and this is true for photons whose energy is slightly above E_g), the current of the absorbed photons in the volume $V = s \cdot L$ is [2]:

$$I_{abs} = \alpha \cdot s \cdot L \cdot 4\pi \cdot I_{\Omega} \tag{2.7}$$

where α is the absorption coefficient, s is the area on the surface, L is the ray internal path length and I_{Ω} is the photon current inside the slab per solid angle. For Eq. (2.7) it has been assumed a surface reflection equal to zero.

According to Eq. (2.6), the photon current per solid angle outside (where photons are distributed over 2π) is a factor of $2n^2$ lower, therefore, the escaping photons current is [2]:

$$I_{emi} = s \cdot {}^{2\pi}/_{2n^2} \cdot I_{\Omega} \tag{2.8}$$

At equilibrium it should be:

$$I_{inc} = I_{\mathrm{emi}} + I_{\mathrm{abs}} \tag{2.9}$$

Absorptivity is defined as [2]:

$$A = {}^{I_{\mathrm{abs}}}/_{I_{\mathrm{inc}}} = {}^{I_{\mathrm{abs}}}/_{(I_{emi} + I_{\mathrm{abs}})} = {}^{1}\Big/\left[\left({}^{1}/_{4n^2\alpha \cdot L}\right) + 1\right] \approx 4n^2\alpha \cdot L \tag{2.10}$$

The last approximated equality is acceptable because α is assumed low. The absorptivity for a single photon passing along L, in non-textured slab, is $\alpha \cdot L$. Thus, Eq. (2.10) states that the absorptivity of a cell, with ergodic surface, is enhanced by a factor of $4n^2$, defined as the "Yablonovitch limit" [4]. Such enhancement results from the light trapping effects of the peculiar surface morphology. If the surface texturing only partially causes the randomization of light inside the cell, the absorptivity enhancement factor is less than the Yablonovitch limit. For this not perfectly ergodic cell surfaces a "trapping factor" I is defined, always ranging from unity (in the case of planar slabs) to $4n^2$.

According to Eq. (2.10), the factor B becomes $I/4n^2$ in Eq. (1.13) [5], which can be rewritten in the following way:

$$\mu_{oc} = E_g\left(1 - {}^{T_0}/_{T_S}\right) - KT_0\left[ln\left({}^{\Omega_E}/_{\Omega_S}\right) + ln\left({}^{4n^2}/_{I}\right) - ln(QE)\right] \qquad (2.11)$$

Combining wisely the antireflection and light trapping principles, discussed in these two sections, it is possible to improve the open circuit voltage and to increase the photo-current of a cell, in other words its efficiency. In addition, decreasing the efficiency loss factor $K{\cdot}T_0{\cdot}ln(4n^2/I)$ in Eq. (2.11) by improved light trapping, allows to obtain high efficiency solar cells even with lower materials quality, i.e. lower QE. This could reduce the cost of c-Si based cells. The group led by Professor M. Green, implementing optimized antireflection coatings and efficient light trapping surface textures (inverted pyramids), fabricated a c-Si solar cell (PERL) with the high efficiency of 25% (see Fig. 2.1) [6].

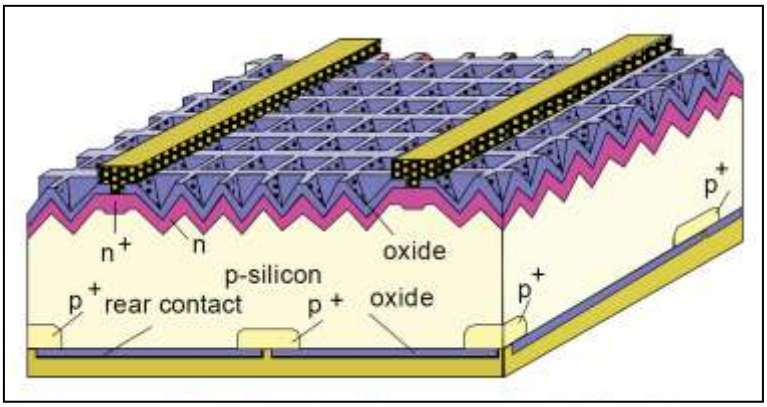

Fig. 2.1 *PERL solar cell (image taken from Ref. [6]).*

Proficient light trapping is mandatory to fabricate high efficiency thin-film solar cells, because the reduced thickness of the absorber layer does not allow great absorption of those photons with energy slightly above the material band gap. However, all the principles and the results discussed up to now are valid in the ray-optics regime, that is, when the thickness of the cell and the size of the texture features are much greater than the wavelength of the light. For light trapping in thin-film cells, it is necessary to work in the wave regime, where light is indeed treated as a wave phenomenon, therefore it can be made to interfere in specific regions of the cell [4].

As it will be shown in the next sections, this new light management approach is essentially based on the redistribution of the PDOS inside the cell. Whereas, in the ray-optics regime, PDOS are absolutely not redistributed in space and spectrum.

2.3 -Light trapping approaches for thin-film solar cells

Light trapping and management in thin-film solar cells can be accomplished employing dielectric or metallic structures in the cells. In fact, these objects, that can be particles, gratings or multilayer with nano or mesoscopic dimensions, interact with the incident light causing radiation scattering, diffraction, interference and concentration phenomena inside the cell. Appropriate engineering of these objects structural parameters, which control the light-matter interactions, together with a suitable choice of structure disposition in the solar cell, are necessary actions to obtain excellent cell performances in terms of solar radiation harvesting.

Dielectric ordered structures, for cell light management, form the large family of photonic crystals (PC). PCs can be categorized in three classes, 1D, 2D and 3D, according to the dimensions along which the dielectric constant ε periodicity occurs. A PC can be a periodic stack of alternating dielectric layers with different dielectric constants (1D), an array of dielectric rods (2D) or a lattice of dielectric particle (3D), such as spheres (see Fig. 2.2). The symmetry arguments that can be carried out in these structures resemble the theory of electronic states in crystal lattices, therefore, PC can also possess a range of frequencies in which light cannot propagate in the structure, known as photonic band gap (PBG) [7]. Owing to this property, PCs can be used as non-absorbing back reflectors in solar cells [4].

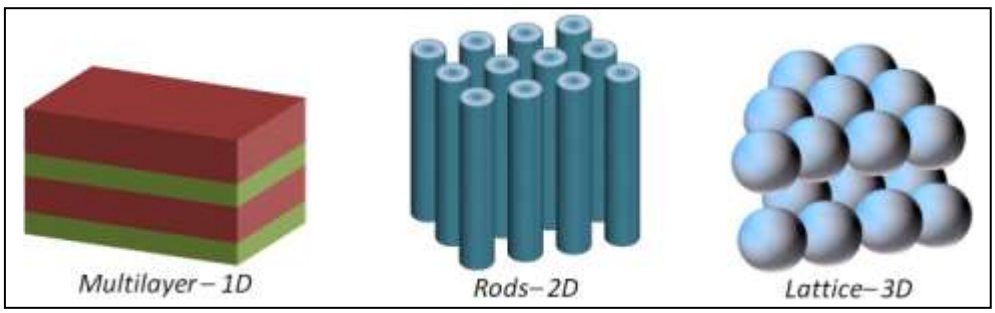

Fig. 2.2 *Examples of photonic crystals.*

A PC can be designed also as a Bragg grating (see Fig. 2.3), diffracting, in reflection or transmission, (normal) incident light according to the well known Bragg formula:

$$\sin\theta_m = {}^{m\cdot\lambda}/_{d} \tag{2.12}$$

where *d* is the grating period, *m* is the diffraction order integer and ϑ_m is the scattering angle (of order *m*) with respect to the normal direction, at which the light is diffracted. The diffracted light is the sum of the waves coherently diffracted from each of the grating elements. The total pattern is a convolution of diffraction and interference patterns, therefore the intensity of the different orders is a decreasing function of index *m*. When a PC grating is combined with a thin absorbing layer, the light, scattered at angles that ensure total internal reflection, is coupled with the quasi-guided modes of the layer (see Fig. 2.3). This means that the diffracted light is trapped inside the layer and will propagate, almost in two dimensions, on enhanced paths, having, in this way, more probability to be absorbed.

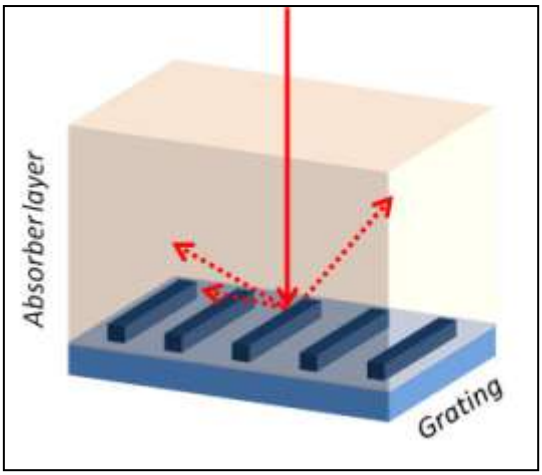

Fig. 2.3 *Dielectric diffraction grating on the back of a solar cell. The incident (full line) light is scattered (dotted line) and coupled with quasi guided modes.*

The physics underneath PC Bragg gratings, unfortunately, entails some shortcomings for light trapping and absorption amplification [4] [8]:

1. Eq. (2.12) depends on the wavelength λ;
2. gratings with large period, in spite of exciting many resonances, scatter low order resonances at small angles, thus total internal reflection and coupling with quasi-guided modes do not occur;
3. small period gratings scatter fewer (yet stronger) resonances;
4. low order diffractions, which according to point 2. are not so efficiently trapped, are the most intense for a single grating.

Recently, it has been theoretically and experimentally proven by Professor M. Krauss and co-workers that the "super-cell" design approach can overcome the problems listed above [8]. The concept of "super-cell" is based on the argument that the diffraction pattern of a single grating, in which the low order resonances are the most intense, can be properly modulated by means of interference effects. In fact, a "super-cell" grating, resulting from the superposition of sub-gratings, spatially shifted from one another, can design destructive interference for the lower order diffractions and constructive interference for the higher ones (see Fig. 2.4). Destructive interference occurs because the low order diffractions from every sub-grating, result out of phase with one another (see Fig. 2.4).

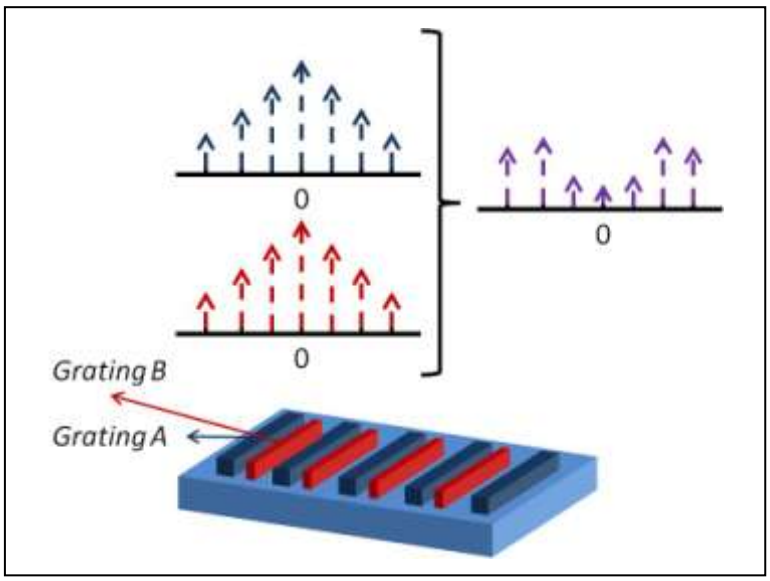

Fig. 2.4 *The super-cell grating as superposition of sub-gratings. The total diffraction pattern is the result of interference between the sub-gratings patterns.*

Coupling of the incident light with quasi-guided modes of the photoactive layer can be fulfilled also patterning the photoactive region itself into a PC [4] (see Fig. 2.5). Mode coupling, that is light confinement inside the absorbing layer, is possible due to the scattering of incoming radiation by the dielectric filler structures inserted among the active film of the cell. The propagation of matched quasi-guided modes in the cell is a complex interplay between in-plane multiple scattering, electro-magnetic field localization phenomena and out-of-plane leakages [9]. In particular, if the field concentration takes place inside the active regions, high amplification of cell absorption will arise. Optimization of the structural parameters of the patterned active layer filled with a PC lattice, allows, in general, to modulate the PDOS of the layer and to tune its amplified spectral response to a desired frequency band. Furthermore, thanks to this third use of PC in thin-film solar cells, compared to the previous approaches, one has more mode profiles tuning [4].

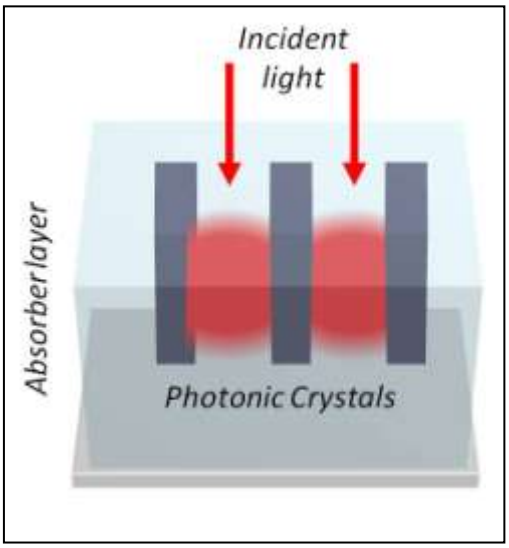

Fig. 2.5 *Solar cell with photonic crystals patterned inside the absorber layer. The incident light is coupled with the quasi-guided modes of the patterned layer. The result is a concentrated and enhanced electro-magnetic field in the absorbing volume.*

Not long ago, Wiersma and co-workers [9], performing finite-difference-time-domain methods, showed that remarkable results, in terms of light trapping and absorption enhancement in thin films, can be achieved with a manageable approach very similar to the latest described. In the structure depicted in Fig. 2.5, they simply substituted the filler dielectric material, constituting the interpenetrating PC, with voids, arranged in specific manners. In this case light is confined in the plane of the perforated thin film since the holes, like the PC filler structures, serve as scattering centres, coupling the incident waves with the film quasi-guided modes [9]. When the structural parameters, as the hole size and disposition, are optimized for the incident radiation, the arising field pattern resembles the concentrated pattern typical for the film patterned into a PC (see Fig. 2.6). A further interesting outcome from the study [9] of Wiersma group is that the properties of coupling between the incident free radiation and the film modes depend on the spatial arrangement of the holes. On the film, holes can be disposed randomly, with short-range spatial correlation (amorphous) or conforming to an ordered lattice. Each of this design give absorption enhancement factors of different extents with respect to the case of a continuous layer. Both Random and amorphous holes dispositions give higher amplification factors compared to the ordered holes lattice case (see Fig. 2.7). In particular, the disordered arrangements make the coupling efficiency weakly depending on the light incidence angle, because the excitable resonances are uniformly distributed over the planar wave vector component of the incident light [9].

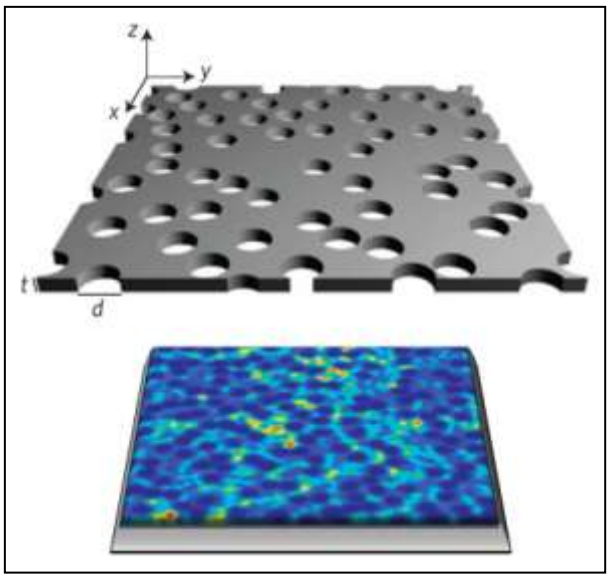

Fig. 2.6 *The image on the top is a view of the nano-structured film proposed by Wiersma and co-workers. Below it is depicted the top view of the electro-magnetic energy density inside the above film invested by a orthogonal plane wave at frequency t/λ = 0.15 (images taken from Ref. [9]).*

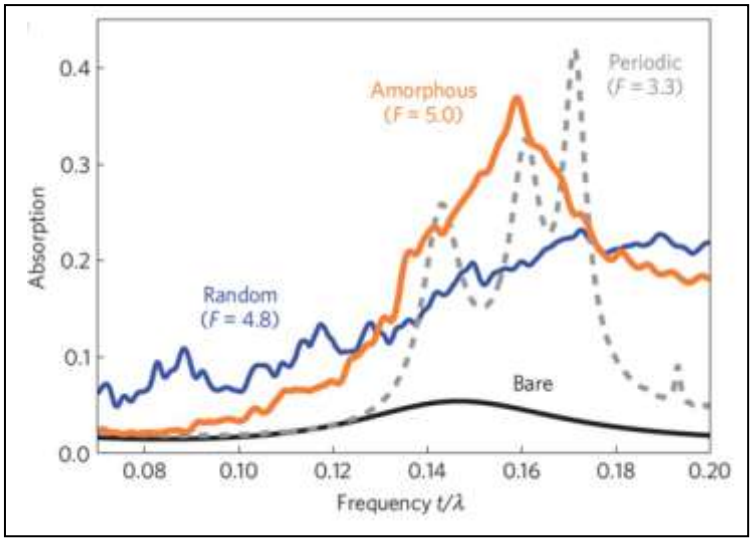

Fig. 2.7 *Absorption spectra of the three kinds of film studied by Wiersma and co-workers: bare film (black line), film with random holes (blue line), film with ordered lattice of holes (dashed line) and film with amorphous lattice of holes (orange line) (image taken from Ref. [9]). For each film is reported the absorption enhancement factor F.*

Another approach employing dielectric structures to enhance solar cell absorption is the use of dielectric spheres, spheroids or complex shaped objects as field focusing mesoscopic lenses (see Fig. 2.8). In the last decades, it has been evidenced that these objects, having curved surfaces or sharp edges, when invested by light, are able to localize photonic plumes near their surface or to highly concentrate electro-magnetic energy inside their volume. Such radiation plumes of amplified electro-magnetic field are not evanescent and are restricted transversally into few hundreds of nanometres, that is why they are called "photonic nano-jets" (PNJ). The location, the extension and the intensity of the PNJs depend on the refractive index contrast with the surrounding medium, the size of the dielectric scattering object or its superficial features dimension respect the light wavelength. Quantitatively, the electro-magnetic field distribution inside and outside a dielectric scattering sphere can be calculated by Lorenz-Mie model [Hufmann]. Within this theory, the total field is divided into the incident, internal-diffracted and scattered fields [10]. Each of these fields is represented by an infinite series in terms of sphere eigenfunctions, and both the internal and scattered fields intensities will be many orders of magnitudes amplified if morphological resonances are excited by the incident radiation. A similar mathematics lays behind non-spherical scattering objects, however, to calculate the total field distribution, numerical approaches are mandatory.

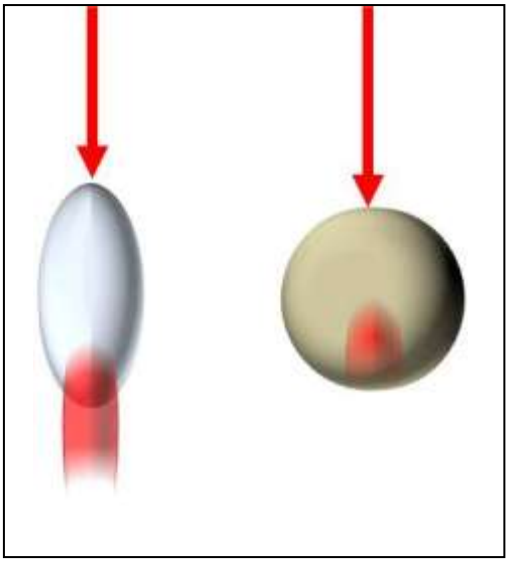

Fig. 2.8 *Dielectric structures invested by light and focusing electro-magnetic energy near the surface (photonic nano-jet) or inside their volume.*

The limit of the absorption enhancement, that can be obtained by means of these approaches in the wave regime is, in general, difficult to assess [4]. For certain cases, information theory arguments can be invoked to demonstrate that the absorption limit, when integrated over all the incidence angles, is always bound by the Yablonovitch limit [4]. Indeed, the absorption rate of an active material depends on the number of modes in the material volume that can be coupled by the incoming photons. For the kinds of light trapping approaches discussed until now, only propagating modes can exist in the cell volume. Since the field of the propagating waves has a bound number of degrees of freedom, the number of available modes in a finite volume is limited [11]. However, evanescent electro-magnetic fields (known also as near-fields) have to be described by a larger number of variables with respect to the propagating waves field. Since the minimum number of field state variables is the quantity of degrees of freedom of the field, a manner to beat the Yablonovitch limit is to employ the concentrated fields of evanescent waves in the absorbing material of a cell [4]. Such evanescent strong fields can be generated by metallic nano-particles (MNPs) or metal gratings (MGs) [12].

2.4 - Fabrication of nanostructures

In the previous section it has been discussed that each of the light trapping and cell absorption enhancement approach relies on a different and peculiar light-matter interaction. The efficiency of an approach is determined firstly by the nature of the involved light-matter interaction, but also by the approach integration with the whole structure and all the components of the cell. The successful fulfilment of a powerful light-trapping phenomenon exploitation, together with its efficacious design and integration in a thin-film solar cell has been several times demonstrated, on laboratory scale, thanks to the utilization of potent but too complex synthesis methods, such as electron-beam lithography and focused ion-beam milling [13].

Once a prototypal solar cell has shown the beneficial effects of its integrated light trapping system, a key issue for its deep impact in the energy market is the availability of a reliable and scalable technique for the fabrication of light trapping structures. For ARC films and planar PCs the scalable deposition techniques are not cumbersome and high level of know-how has been recently reached. Whereas, light trapping approaches based on fine gratings or NPs still need technological refinements or even revolutionary breakthrough concerning their large-scale synthesis and device integration. Nowadays the most promising synthesis techniques are the "nano-imprint lithography" [14], the "surface-tension-instability driven agglomeration" [13] and the "catalyzed growth by chemical vapour deposition (CVD)" [15]. Each method has pros and cons:

- Nano-imprint lithography: it allows a fine direct control on the nano-metric structure/object morphology, however it envisages multi-step procedures, sometimes difficult to apply on large areas.
- Agglomeration: the procedures require facile evaporation of ultra thin layers followed by simple thermal treatments to trigger the surface tension instabilities, necessary for the final agglomeration. Generally, the intrinsic physics laws, underneath such agglomeration mechanisms, allow size and shape related outputs, which are random or, at least, with a large indeterminacy.
- CVD with metal catalyst: among the various methods exploited so far to fabricate nano-structure it has been demonstrated to be very convenient because it does not require ultra-high vacuum, it allows to control the deposition parameters and it is a technique fully implemented in current PV production facilities.

The following arguments have taken inspiration from the second and third class of the discussed methods, since they can be applied on large areas and are cost-effective. Moreover these agglomeration or film instability based methods could take advantages from self-organization mechanisms to provide structures and particles arrays whose size distribution, shape and disposition have a certain degree of order. The fundamental point to realize this is to match the self-organization conditions with cheap processes. In the first part of my experimental activity some attempts have been made in this direction, achieving some interesting evidences on enhanced light absorption in semiconducting nano-structures synthesized by facile thermal processes able to trigger thin-film dewetting phenomena, which in turn, owns the powerful potential of self-organization and ordering.

2.5 - Efficient light trapping in silicon nano-wires produced by catalyzed chemical vapour deposition

Silicon nano-wires (NWs) layers can be used for innovative solar cell architectures, based on radial junctions. In these structures, the light is absorbed vertically by the Si NWs and the photo-generated charges are gathered horizontally, along the NWs cross section (few nanometres), where a core-shell junction is present. Since the charge carriers separation occurs in a very restricted space, their diffusion length can be not particularly large and more defective, hence cheaper, materials can be used for cell fabrication.

Another important advantage of Si NWs is their ability to increase light absorption by means of efficient trapping.

In this section, it is reported the observation of enhanced light absorption of Si NWs, obtained by the combination of chemical vapour deposition (CVD) and metal-induced growth [15]. Moreover, it is shown the relation between the light trapping phenomenon and the NWs characteristics.

2.5.a - Synthesis

Si NWs were grown on a c-Si wafer, where Au dots (areal density = $2 \cdot 10^{12} cm^{-2}$) were previously deposited. The deposition system used was an Inductively Coupled (ICP) CVD, operated at plasma powers ranging between 0 and 1000 W. Silane (SiH_4) was employed as precursor gas, mixed with argon (SiH_4/Ar = 30). The substrate was kept at 380 °C during the depositions (duration going from 15 min up to 2 h) which were performed at 20 mTorr. The list of the prepared samples is reported in Tab. 2.1.

Sample	Plasma Power (W)	Deposition Time (s)
A	*1000*	*900*
B	*100*	*900*
CI	*20*	*900*
CII	*20*	*1800*

Tab. 2.1 *List of the deposited samples.*

2.5.b - Morphologic characterization

The samples morphology was analyzed using a ZEISS SUPRA 35 FE-SEM. The SEM micrographs (see Fig. 2.9) revealed that:

- sample ***A*** consists of a continuous α-Si film (thickness = 135 nm), with no Si NWs;
- sample ***B*** is a thinner continuous α-Si layer (thickness = 15 nm), on which few Si NWs appear;
- sample ***CI*** is a dense Si NWs carpet with no continuous Si layer underneath. The Si NWs mean length resulted 260 nm;
- sample ***CII*** is also a dense Si NWs layer, directly lying on the c-Si substrate. The Si NWs mean length is 500 nm, due to the longer deposition time.

Moreover, high resolution TEM analyses unveiled that such Si NWs are crystalline.

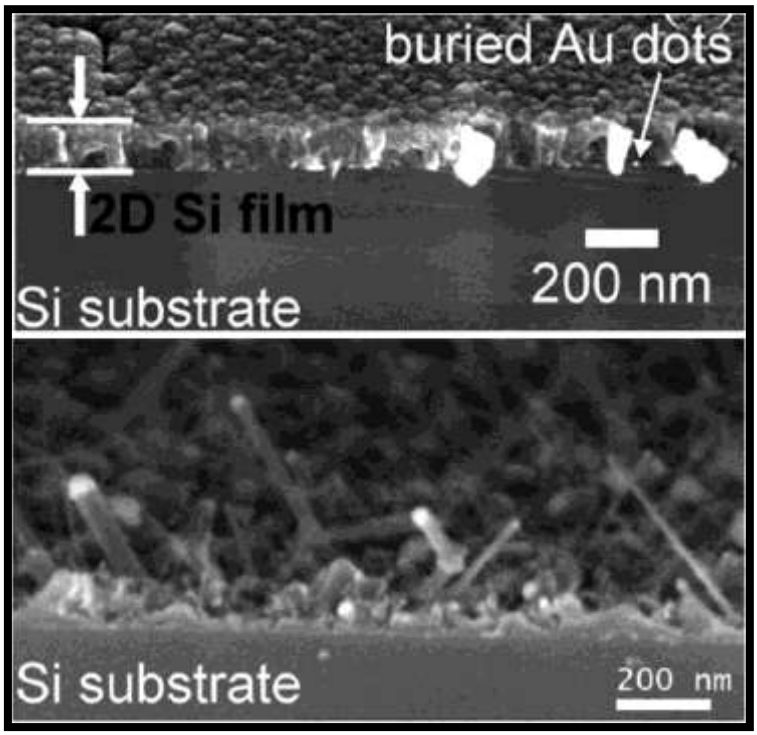

Fig. 2.9 *SEM micrographs in cross view on samples **A** (upper panel) and **CI** (lower panel).*

2.5.c - Spectrophotometric characterization

Reflectance *R(λ)* spectra were measured by an integrating sphere installed in a VARIAN Cary 500 double beam scanning UV-Visible-NIR spectrophotometer. In particular, total reflectance, $R_t(\lambda)$, and diffuse reflectance, $R_d(\lambda)$, were acquired by using two different configurations, the first including the specular component that hits the sphere and is diffused within it and the second allowing the specular component to escape through the entrance port in order to be excluded by the light detection. All the collected spectra were normalized to a standard reference material.

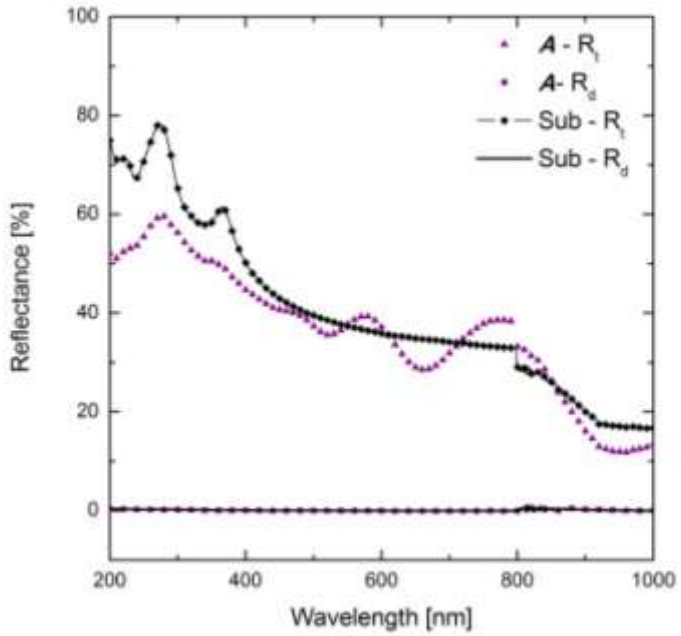

Fig. 2.10 *Total and diffused reflectance of the sample **A** and the c-Si wafer substrate.*

Figure 2.10 shows $R_t(\lambda)$ and $R_d(\lambda)$ measured on the c-Si wafer substrate and the same spectra measured on sample ***A***. For this sample, $R_d(\lambda)$ is negligible as for the substrate, being their surfaces not structured. The $R_t(\lambda)$ spectrum maintains exactly the same trend of c-Si except for a lowering at $\lambda < 500$ nm due to absorption by the thin α-Si film. Oscillations are present at higher wavelength, owing to interference effects. For sample ***B*** (see Fig. 2.11) $R_d(\lambda)$ is as well negligible, due to the very limited appearance of Si NWs. Since the α-Si layer is, in this case, thinner, $R_t(\lambda)$ appears closer to the c-Si wafer spectrum.

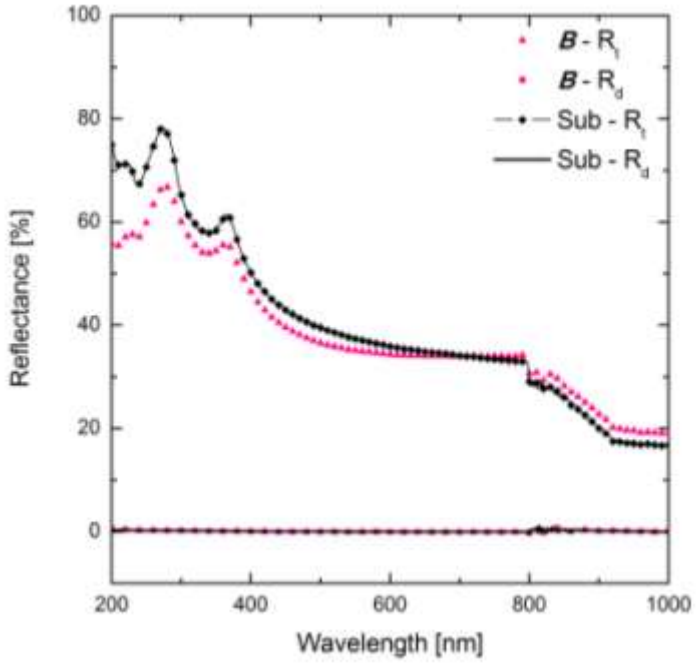

Fig. 2.11 *Total and diffused reflectance of the sample **B** and the c-Si wafer substrate.*

On the other hand, the high concentration of Si NWs in samples ***CI*** and ***CII***, heavily reduces $R_t\,(\lambda)$, which now mainly consists of the diffuse component (see Figures 2.12 and 2.13). This effect is more evident in sample ***CII***, with longer NWs.

The observed large reduction of $R_t\,(\lambda)$ corresponds to an increase of the absorbance, since incident light is efficiently trapped by dense Si NWs. In particular, longer NWs cause enhanced light diffuse scattering (that leads to amplified trapping) being, for sample ***CII***, the difference $R_t\,(\lambda) - R_d\,(\lambda)$ much smaller with respect to sample ***CI***.

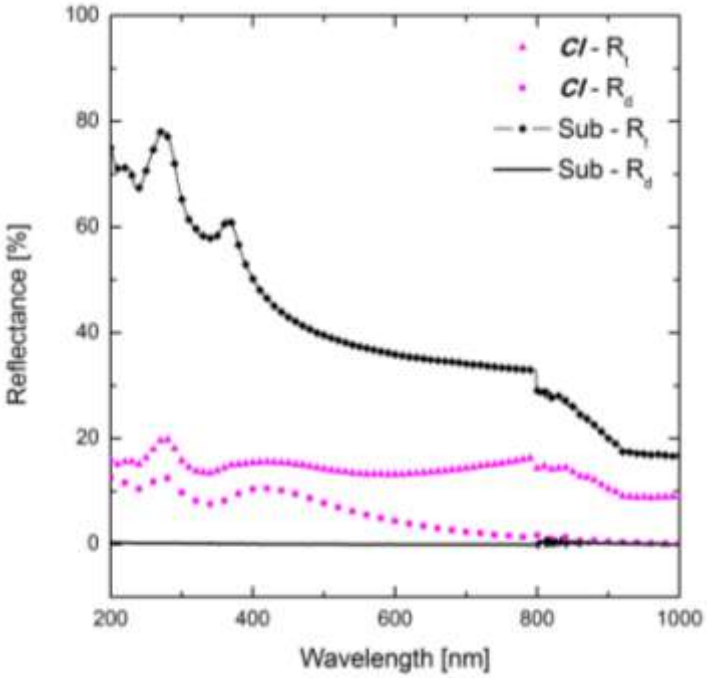

Fig. 2.12 *Total and diffused reflectance of the sample* ***CI*** *and the c-Si wafer substrate.*

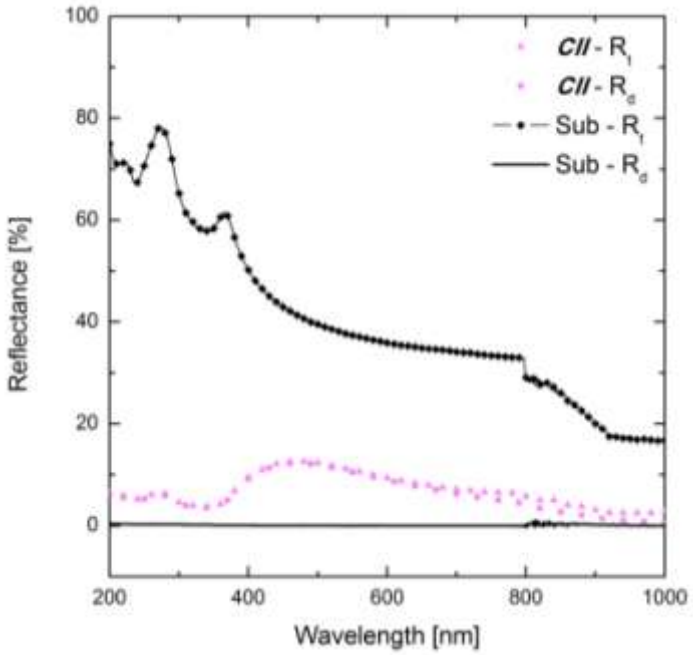

Fig. 2.13 *Total and diffused reflectance of the sample* ***CII*** *and the c-Si wafer substrate.*

2.6 - Thin-film dewetting

Nano-patterns and ensembles of NPs can be created from a uniform flat and thin layer, deposited on a substrate, if this layer, once has reached the liquid form, is able to break-up into particular features before re-solidification occurs.

The rupture of the molten layer, commonly called dewetting of the film, is essentially the formation and growth of holes triggered by film thickness fluctuations of a certain extent. After the first film break-up stages, holes coalesce and a set of droplets appears. The final solidification of this droplets leads to the formation of nano-particles ensemble. The process of dewetting starts when attractive intermolecular forces overwhelm the stabilizing effect of interfacial tension [16]. As all the spontaneous processes, it is driven by the need for the system (molten film + substrate + air) to reach the lowest free energy state. In particular, hydrodynamic dewetting occurs because the system approaches a minimum of the interface potential ϕ, pushed by the instability driving forces, appearing as the potential partial second derivative, with respect to the thickness h, is negative ($\partial_{hh}\phi(h) < 0$).

The interfacial potential $\phi(h')$ is defined as the excess free energy it takes to bring the interfaces substrate/film and film/air from $h = \infty$ to $h = h'$ [17].

Depending on the nature and intensity of the molecular interactions between the substrate and the film, together with the film surface stress amplitude, the potential $\phi(h)$ can assume three kinds of functional dependences with respect to the thickness h, all depicted in Fig. 2.14 [17].

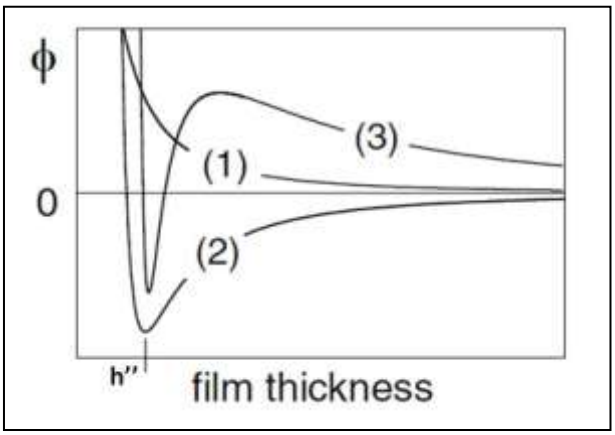

Fig. 2.14 *Interface potential φ as function of film thickness h for: (1) stable, (2) unstable and (3) metastable films (image taken from Ref. [17]).*

In Fig. 2.14, curve (1) has no minimum and any decrease of film thickness would lead to an increase of free energy. Therefore any system described by this potential is stable and dewetting does not occur for any thickness fluctuation. The potential of the second kind (curve (2) in Fig. 2.14) has one global minimum at h''. For every $h > h''$ $\partial_{hh}\phi(h) < 0$, thus the dewetting will be always spontaneous (unstable film) and proceed until the equilibrium value h'' is reached inside the holes. When $\partial_{hh}\phi(h) < 0$, all the thickness fluctuations are exponentially amplified as time passes [18]. It has been theoretically and experimentally reported that the evolution of the spontaneous dewetting consists, more or less, of the following steps [16] [17] [18] (see Fig. 2.15):

1. formation of holes and agglomeration of film material along their rims, forming a polygonal network;
2. coalescence of the growing holes and further material accumulation at the corners of the polygonal holes rims;
3. rupture of the polygons edges and complete formation of droplets at the former polygons corner sites.

The last type of potential (curve (3) in Fig. 2.14) has two minima, one at h'' and the one at $h = \infty$, which are separated by a positive bump of the curve. On the right side of the bump peak at h', $\partial_{hh}\phi(h) > 0$, i. e. the film, with thickness $h > h'$, is stable respect dewetting for thickness fluctuations smaller than $h - h'$. Whereas, for $h < h'$, the film is unstable. Since in this situation, the film is stable for a finite range of perturbations, it is metastable.

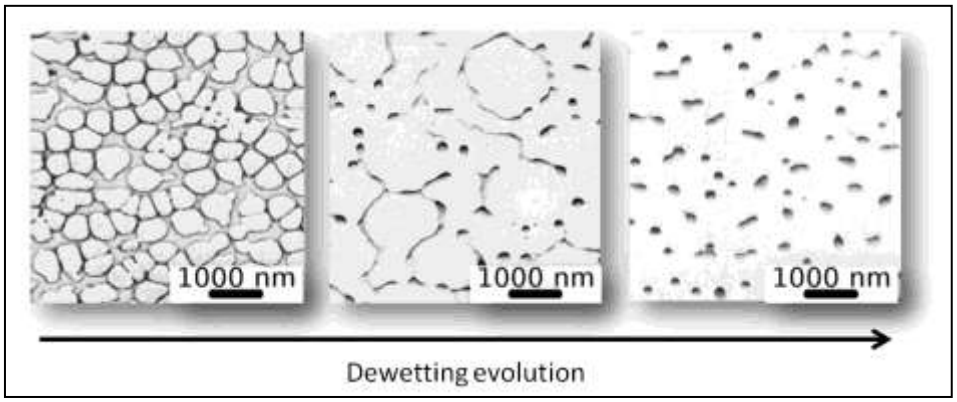

Fig. 2.15 *Dewetting steps in unstable films (images taken from Ref. [16]).*

Two types of film thickness fluctuations can be distinguished:

1. Flat film modes are periodic modulation of the thickness, each described by [18]:
   $h(\boldsymbol{r}) = h_0 + \epsilon \cdot e^{(\beta t + i\boldsymbol{k}\cdot\boldsymbol{r})}$ (2.15)
   where ϵ is the amplitude of the perturbation respect the initial film thickness h_0, $\boldsymbol{k}$ is the wave number of the mode and β is the mode growth rate. When the film is unstable $\beta > 0$ and the related mode are amplified exponentially as previously said. Among all possible modes there exists one growing faster with a certain wavelength λ_m [18]. This fact leads to a dewetting pattern with a characteristic length scale related to λ_m, thus, to a pattern with a certain degree of order and spatial correlation between its features [17]. Such length scale can be evident at every stage of film break-up; for example during the holes formation, it is apparent a correlation between the holes positions, or during holes coalescence, the polygonal network of holes rims can show non-random characteristics, such as the polygons size and shape [16]. This length scale is independent of the initial film conditions [18]. When the unstable film undergoes this kind of rupture it is said it undergoes a "spinodal dewetting". The attribute spinodal comes from the fact that the dynamic equations are based on the well-known Cahn - Hillard model for spinodal phase separation [18].
2. Finite disturbances of the film thickness are the appearances of holes in the initially uniform film surface. Holes can nucleate randomly (thermal nucleation) or at specific sites, such film defects (heterogeneous nucleation) [17]. When the flat film modes are too slow to come into play during the film break-up, these finite disturbances become predominant and the unstable rupture dynamic is said to be "nucleation-dominated" [18]. The principal characteristic of the pattern generated by this dynamic is that disposition of the holes, the size and shape of polygonal rims and the final droplets size and position are completely random and not mutually correlated [18]. When the film is metastable, the only way to dewet is through nucleation.

Dewetting can be induced on various thin films, from polymeric layers [17] to metallic films [16]. The rupture can be induced by heating in furnace a solid film [19] or by shining it with a high ultra-fast (few nanoseconds) laser pulse [16]. Both these treatments are necessary to melt the film, giving it enough mobility to make agglomeration to occur. However, laser annealing is more interesting from the theoretical and application point of views because it makes possible to perform ultra-fast melting and solidification cycles. Therefore it is possible to move and stop the dewetting process at each of its steps. For theoretical studies, it is useful, since one

can investigate each of the dewetting steps. For technologic applications, especially for light trapping in solar cells, it permits, stopping the dewetting process at a certain point, to obtain either nano-patterns (holes rims network) or nano-particles (final stages).

In the last decade it has been evidenced that spinodal and nucleation dewetting dynamics can occur in the same system, just operating few controllable changes in film and substrate characteristics (interface nature and film thickness) [17]. Not long time ago, it has been demonstrated how to exploit heterogeneous dewetting to create Si and Ge NPs from pre-patterned layers [19]. Unfortunately the pre-patterning step has been achieved by electron beam lithography, which is not a large scalable technique. What sounds much more promising, instead, is controllable exploitation of spinodal dynamic. Indeed one can create ordered nano-patterns or NPs arrays just through self-organization dynamic not driven by complex layer pre-patterning. Recently, Favazza and co-workers reported laser induced spinodal dewetting of a cobalt thin film [16].

2.7 - Pulsed laser induced dewetting for semiconductor and dielectric nano-structures - Fundamental concepts for a novel approach

In section 2.3 it has been stated that to achieve efficient light trapping and enhanced absorption in thin-film solar cells one should exploit the peculiar light-matter interactions effects, arising from the incidence of radiation upon nano-structures with specific sizes and morphologies. Moreover, in sections 2.4 and 2.6 it has been shown that various methods, with different cost and technologic effectiveness, are nowadays available to synthesize and integrate such nano-structures in solar cells. Specifically, it has been discussed how hydrodynamic thin-film instabilities, induced by ultra fast laser irradiation, appear as a promising mechanism to create a wide range of useful nano-structures, in a fast and cheap way. The fast melting/solidification cycles, caused by the laser treatment, allow one to freeze, in a controllable manner, the different stages of dewetting and the related nano-patterns, arising from the film break-up. Furthermore, as previously reported, when the film rupture dynamic is spinodal, the resulting pattern, at every stage, owns a characteristic length scale. Therefore, setting the film, substrate and laser beam properties in such a way to favour spinodal dewetting, it could be possible to create ordered or semi-ordered lattice of holes or NPs (hemispheres, spheroids, elongated NPs, etc...).

The pivotal idea at the basis of my research activity, focused on light trapping in silicon nano-structures was to utilize both spinodal and thermal nucleation dewetting, induced by ultra-fast laser irradiation, to reproduce most of the useful semiconductor and dielectric patterns previously discussed. The complete frame of this conception is schematized in Fig. 2.16.

The pierced film, obtainable at the early stages of dewetting interestingly resemble, regarding the geometry, the structure investigated by Wiersma and co-workers. Whereas, the elongated nano-structures arising at the intermediate dewetting stages, if result with an interconnection degree sufficient for charge carriers planar flow (percolative transport), can be an advantageous patterned absorber layer (silicon) for solar cells, whose absorption is enhanced. Finally, the NPs, appearing as the features of the terminal dewetting stages, could be utilized as micro or nano lenses for PNJs, directed on an underlying absorber layer.

The study here presented is a preliminary attempt to verify the validity and the feasibility extents of this idea, i. e. to prove if such method can actually design structures according to the geometries and morphologies already discussed, to give an evidence that such laser synthesized structures show light trapping and absorption

amplification and, finally, to check if peculiar morphologies, not yet presented or discussed in literature, can experience similar enhanced light-matter interactions.

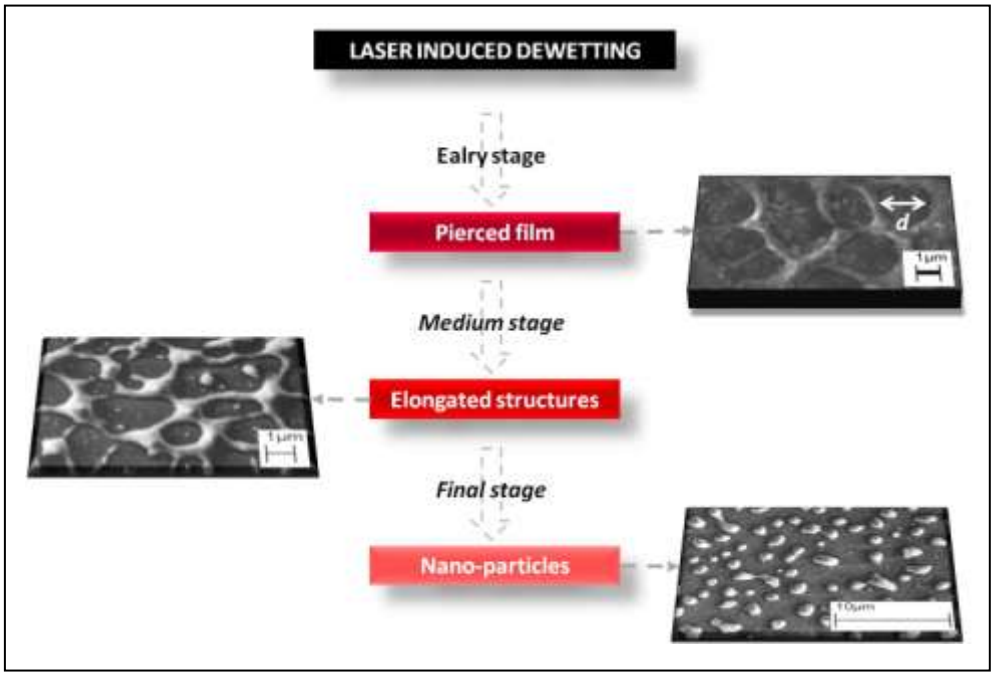

Fig. 2.16 *Production of dielectric nano-structures for light trapping and efficient scattering by pulsed laser induced dewetting: scheme of the idea. The SEM images are taken from some of our lasered silicon thin films at fluences between 450 and 1130 mJ/cm^2.*

2.8 - Enhanced light scattering in silicon nano-structures produced by pulsed laser irradiation

In this section, it is reported the innovative methodology based on pulsed laser irradiation for fabrication of Si nano-structures through dewetting phenomena. These Si nano-structures have been investigated by Raman spectroscopy and a correlation between the large enhancement in the Raman scattering cross section and the nano-structures shape are discussed [20].

2.8.a - Synthesis

Silicon nano-structures have been obtained from thin (120 nm) Si films deposited by ultra-high-vacuum magnetron sputtering of a Si target on fused silica substrate (see Fig. 2.17). In order to avoid any contamination during the synthesis, the chamber pressure, before the sputtering process, reached $1 \cdot 10^{-9}$ mbar. Whereas, the working pressure of the Argon, was maintained at $5 \cdot 10^{-3}$ mbar. The radio-frequency power, needed to erode the target, was set at 400 W, while the substrate was kept at 400 °C, by means of halogen lamps irradiation.

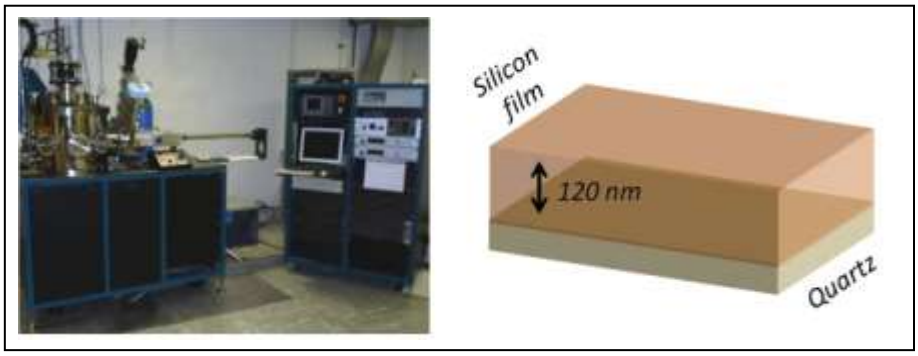

Fig. 2.17 *Photo (left) of the ultra-high-vacuum sputtering system used to deposit our samples. Schematic illustration (right) of the as-deposited samples.*

2.8.b - Laser treatment

Laser pulses were performed in air, using a Nd:YAG laser by Spectra Physics, operated with a green (λ = 532 nm) and Gaussian shaped (*FWHM* = 1 mm) beam (see Fig. 2.18). The duration of a single pulse was only 12 ns and the frequency of multiple pulses 1 Hz. The value of the beam wavelength was appropriate to melt silicon thin layers, since, at this photon energy, the material absorption is high ($\alpha \approx 10^4$ cm^{-1} [21]). On the other hand, the ultra-short duration of the single pulse allows to carry out ultra-fast melting/solidification cycles. The deposited films have been subject to four different treatments:

1) single pulse at a fluence of 425 mJ/cm^2;
2) single pulse at 900 mJ/cm^2;
3) single pulse at 1130 mJ/cm^2;
4) three repeated pulses at 1130 mJ/cm^2.

All the laser treatments produced a 2 mm wide spot on the samples. Each treated sample was labelled, according to the laser process, ***425***, ***900***, ***1130-1*** and ***1130-3***.

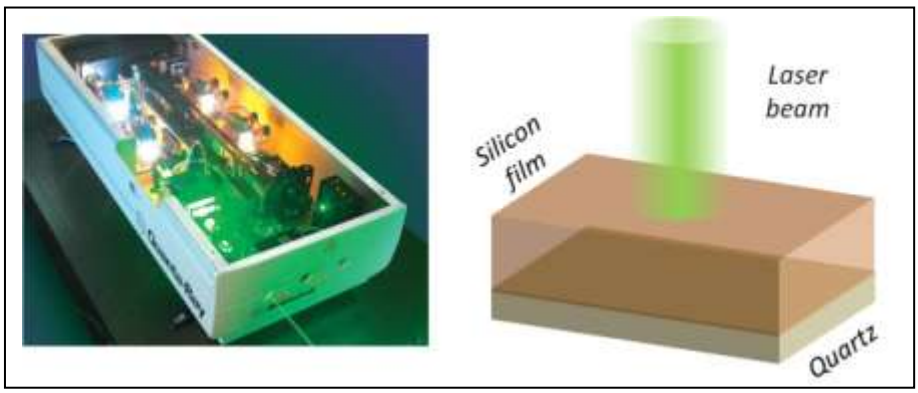

Fig. 2.18 *Photo (left) of the utilized Nd:YAG laser by Spectra Physics. On the right the it is schematized the laser treatment.*

2.8.c - Morphologic characterization

The planar samples morphology was investigated by a ZEISS SUPRA 25 Field Emission Scanning Electron Microscope (FE-SEM), while more detailed cross sectional views of the laser treated films were obtained by a 200 KV Jeol 2010F Transmission Electron Microscope (TEM), equipped with a Gatan Image Filter to perform energy filtered TEM (EF-TEM) analyses. The EF-TEM characterizations were carried out to identify, in the cross sectional view, the chemical composition of the nano-structures different parts.

SEM images, taken at the centre of the laser spot (see Figures 2.19 - 2.21 - 2.22), show that after laser irradiation the surface of samples changes from flat and continuous (as-deposited sample) to largely broken and corrugated structures, produced by film dewetting. The most apparent information conveyed by these images is that the shape and dimension of Si nano-structures drastically depend on the laser irradiation, leaving different uncovered portions of the underlying quartz substrate.

For the lowest fluence (425 mJ/cm^2), the film does not show any significant modification. But after one pulse at 900 mJ/cm^2 (sample ***900*** in Fig. 2.19 - a) the film is broken into a network of Si droplets (bumps smaller than 1 μm) often linked each other by narrow fin-like structures (about 1 - 2 μm long, with thickness down to about 100 nm) The formation of Si network with nano-drops and narrow interconnections can be better appreciated looking at the SEM images, taken in tilt configuration (sample tilted 60° out of the e-beam direction), reported in Fig. 2.20.

Increasing the laser fluence to 1130 mJ/cm^2, after one pulse (sample ***1130-1*** in Fig. 2.21) the network structure is totally lost and a population of isolated Si nano-clusters comes out. Statistical analysis of the SEM image revealed a bimodal size distribution peaked at 350 and 750 nm. This fact suggests that two families of Si nano-clusters are present with different average diameters.

After three pulses at the laser fluence of 1130 mJ/cm^2 (sample ***1130-3*** in Fig. 2.22), the morphology of Si nano-structures changes again going towards mono-disperse Si structures, as the small Si nano-clusters vanished and the large ones increased their mean diameter up to 900 nm (see Fig. 2.23). Some elongated particles are also evident, suggesting some coalescence phenomena.

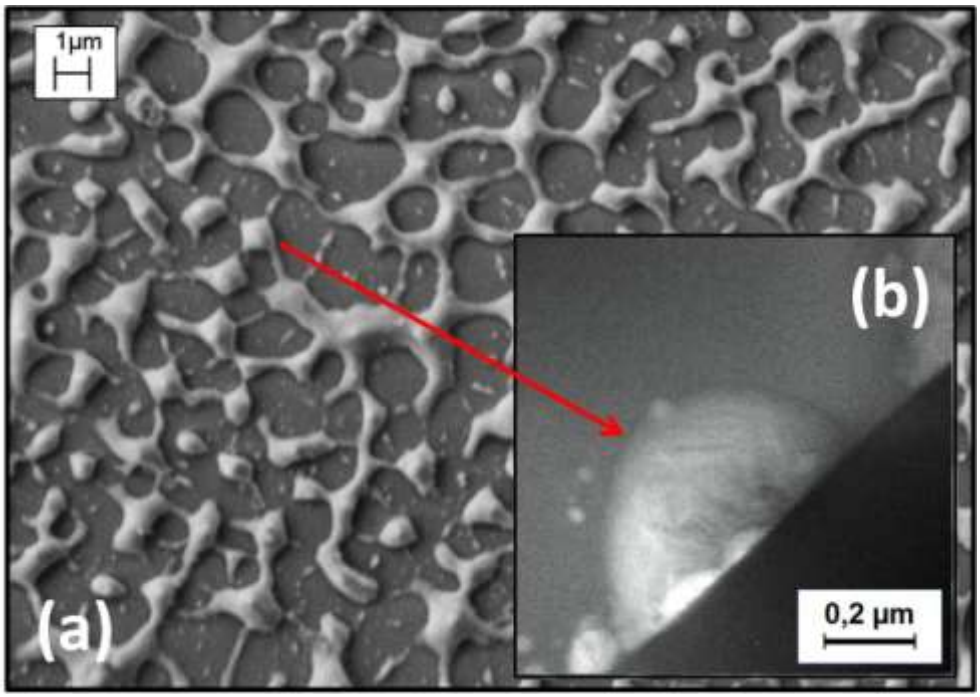

Fig. 2.19 *SEM plan view of Si thin film irradiated with nanosecond laser single pulse at energy fluence of 900 mJ/cm^2 (a). TEM cross sectional image (b) of a Si bump in sample **900** as indicated by arrow.*

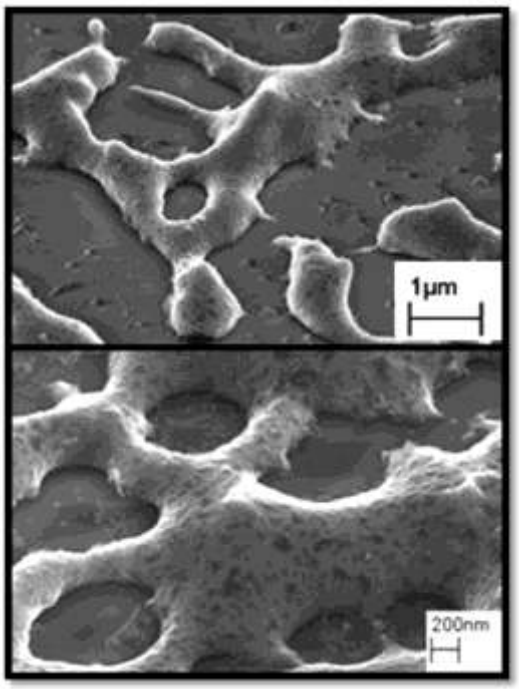

Fig. 2.20 *SEM 60° tilted views of the edge of the laser spot in sample **900**. Evidence of the Si thin film dewetting is given with the formation of broken film with disordered holes.*

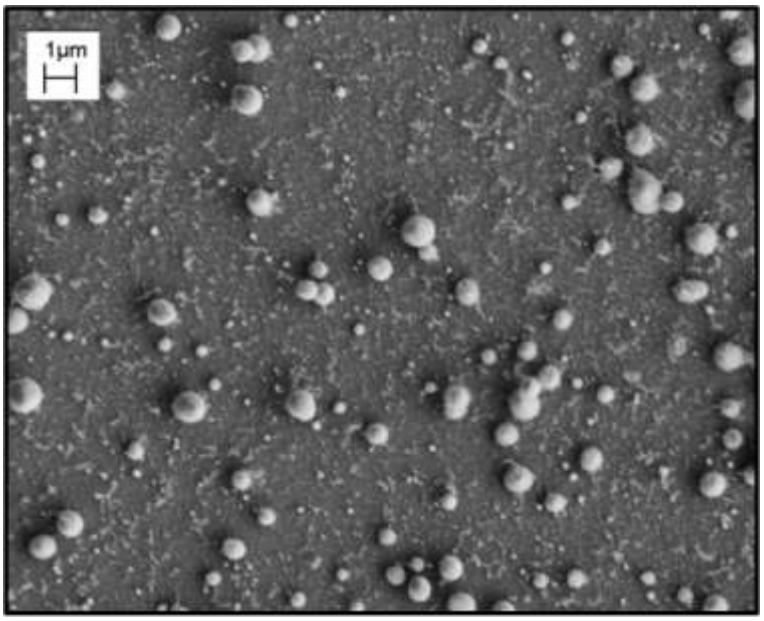

Fig. 2.21 *SEM plan view of Si thin film irradiated with nanosecond laser single pulse at energy fluence of 1130 mJ/cm^2.*

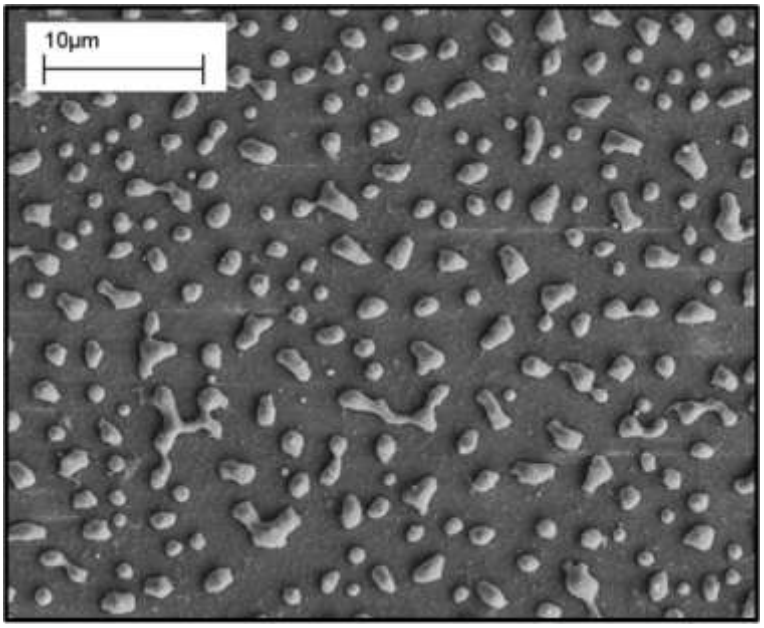

Fig. 2.22 *SEM plan view of Si thin film irradiated with three nanosecond laser pulses at energy fluence of 1130 mJ/cm^2.*

To account for the 3D shape of Si nano-structures, Fig. 2.19 - b reports the cross section EF-TEM image of sample ***900***, by selecting the 16 eV energy loss window, which corresponds to the Si bulk plasmon excitation energy. The image shows a Si cluster compatible with one of the bumps observed in Fig. 2.19 - a, exhibiting a hemispherical shape, whose diameter is about 800 nm. TEM revealed that these structures are made up of crystalline silicon, without any silicon oxide shell surrounding them, and that the substrate was uncovered except where the nano-structures are located.

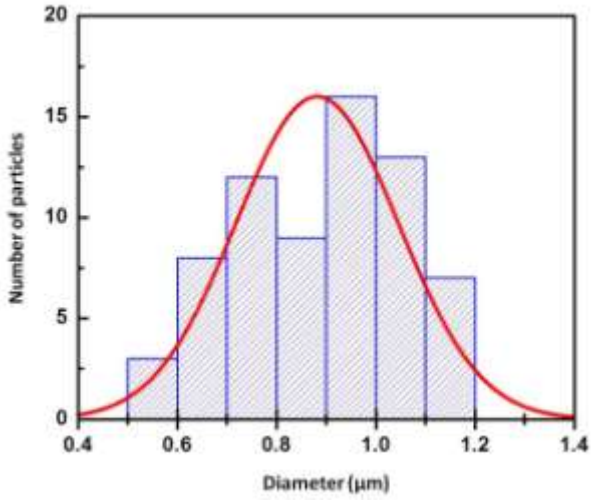

Fig. 2.23 *Size distribution of the Si nano-clusters in sample **1130-3**.*

The observed generation of Si nano-structures can be explained with the hydrodynamic dewetting instability induced by the non-equilibrium heating and ultra-rapid quenching of irradiated films. Specifically, the absorption of laser radiation suddenly leads to melting of Si film, which breaks up and evolves in various structures before the ultra-fast quenching and re-solidification. In our case, sample ***900*** shows a cellular structure, compatible with initial stages of dewetting process. Favazza and co-workers demonstrated that increasing the laser fluence increases the rate at which the patterns evolve [16]; therefore, in sample ***1130-1*** a further cracking of the melted film occurred and led to the disappearance of the network structure, with the formation of isolated particles. Once the laser irradiation was repeated in sample ***1130-3*** the size distribution significantly shrank, while coalescence process occurs leading to mean size increase.

In section 2.6, it has been argued that dewetting morphology can progress via three pathways: spinodal, thermal and heterogeneous nucleation. The former gives always patterns with a characteristic length scale, that is with ordered properties, such as holes width, clusters size and disposition. whereas the last two, if no film pre-patterning has been performed, lead to random structures. As future perspectives for this work, to deeply investigate these phenomena and to recognise the details of the dynamic involved it should be planned to:

1) produce several sets of flat Si films. Each set has to be characterized by a certain thickness. In fact, such parameter is critical for dewetting process, and the triggering of nucleation instead of spinodal dewetting depends on this factor [18];
2) be sure that as-deposited film irregularities are negligible, in order to exclude the possibility of heterogeneous dewetting to occur without control;
3) generate different irradiated samples from each set of deposited films. This step has to be carried out modulating the laser fluence and the number of pulses. In this way it is possible to observe the dewetting patterns evolution for every film thickness and, in case, point out the differences between spinodal and nucleation dynamics.

However, for our samples, it can be said anyway that both the features typical of spinodal and nucleation dewetting are present. Indeed, in sample ***1130-1*** the disposition of nano-clusters is random and their size distribution is not unimodal. On the other hand in sample ***1130-3***, the cluster size distribution is unimodal and in sample ***900***, the Si network appears with holes, more or less, of similar width. For a given film thickness, the coexistence of both spinodal and nucleation features, in the progressive dewetting patterns, is possible according to the theoretical analysis carried out by Thiele and Velarde [18]. Hence it can be stated that our cases are evidences of the spinodal and nucleation mixed dynamic.

2.8.d - Rutherford backscattering spectrometry

To investigate if some Si loss occurs during laser irradiation, Rutherford backscattering spectrometry measurements (RBS, 2.0 MeV He^+ beam, 165° backscattering angle) were performed on samples before and after laser irradiation. RBS spectra simulations were performed by "SimNRA" software [22].

A reference sample, here called ***ref*** was obtained by annealing an as-deposited Si thin-film at 900 °C for 1h in N_2 ambient to ensure a complete crystallization. In Fig. 2.23, the RBS spectra (symbols) is reported for the sample ***ref*** (Fig. 2.24 - a), which is unchanged in comparison with the as-deposited spectrum, and for the sample ***900*** (Fig. 2.24 - b). Signals at 1.14 or 0.74 MeV are related to He^+ backscattered from Si or O atoms at the sample surface. In the sample ***ref***, it is clear that Si is present at the surface but O is not, as O signal appears at energy below 0.67 MeV (being related to O in the substrate). Thus, this sample was simulated (line) as a 120 nm Si film over a SiO_2 quartz substrate, as drawn in panel (a). Conversely, in the sample ***900*** (Fig. 2.24 - b) the signal at 0.74 MeV indicates that O is present at the surface, as quartz has been partially uncovered. Moreover, in the same sample, the signal height relative to Si at surface (1.14 MeV) is lower than in the reference sample and it has a long tail at lower energies, due to breaking of the thin film and formation of Si nano-structures higher than 120 nm (as drawn in panel (b)). In Fig. 2.24 - b, the simulation (line) is reported only for He^+ backscattered from Si and O atoms in the substrate, accounting for its partial coverage. The difference between simulation and the RBS spectrum is related to He^+ backscattered from Si atoms above the substrate. By comparing RBS data and simulation, one can extract the residual dose of Si above the substrate (as reported in the table) with an error lower than 3%. From these data, it can be concluded that, in comparison to the reference sample, the laser treatment causes a maximum Si loss of 17% in sample ***1130-3*** irradiated with three pulses.

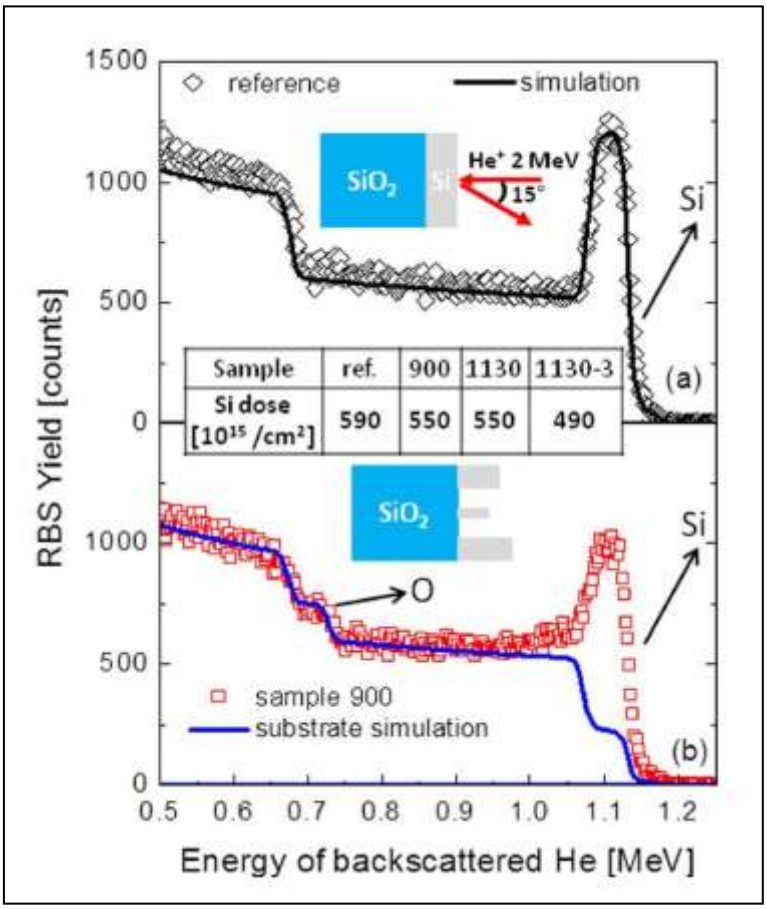

Fig. 2.24 *RBS performed on (a) reference sample **ref** or (b) **900**. Data (symbols) have been fitted (continuous line) assuming the sample structure drawn in each panel. Table reports the dose of Si atoms on top of the quartz substrate for each sample.*

2.8.e - Raman spectroscopy and optical characterization

Spontaneous inelastic light diffusion, as Raman scattering, from a dielectric arises from an incoherent summation over the fields radiated from a distribution of induced polarization sources at the red-shifted frequency ω' with a strength proportional to the local internal field at the incident frequency ω [23]. Since, as it has been discussed in section 2.3, the internal field can become greatly amplified when the incident frequency approaches one or more of the electro-magnetic eigen-frequencies of the dielectric nano-structure, the inelastic scattering intensity can be in turn strongly enhanced [23]. Moreover, the enhanced scattered field at ω' can be further amplified if its red-shifted frequency is resonant with an eigen-frequency of the nano-structure. Indeed, such resonant excitation produces also sharp and intense features in elastic-scattering spectrum. The scattering and absorption efficiencies $Q_{scattering}$ and $Q_{absorption}$ can be analytically calculated for a single dielectric sphere or for single scattering from a mono-dispersed collection of spheres according to the following expression provided by Mie theory [23]:

$$Q_{scattering} = \left(2/_{x^2}\right)\sum_{l=1}^{\infty}(2l+1)[|a_l|^2 + |b_l|^2] \qquad (2.16\text{-a})$$

$$Q_{absorption} = \left(1/_{2x^2}\right)\sum_{l=1}^{\infty}(2l+1)[2 - |a_l - 1|^2 + |2b_l - 1|^2] \qquad (2.16\text{-b})$$

where x is the size parameter $\pi \cdot r/\lambda$ of the sphere of radius r while a_l and b_l are, respectively, the complex electric and magnetic multipole expansion coefficient from the Mie theory.

In Fig. 2.25 the plots of scattering and absorption efficiencies in function of the diameter of a Si sphere in air and invested by a plane wave with λ = 632 nm are shown. The value of λ is the same as the wavelength of the laser probe used, in this work, for Raman spectroscopy measurements. The calculations for the plots were performed by means of the software MiePlot v4.3 [24].

Enhanced Raman scattering, due to the excitation of low-order-structure resonances, were observed and analysed according to this approach on various Si nano-structures by Murphy and Brueck [23]. The variety of the investigated nano-structures included Si spheroids with diameters between 100 and 200 nm, randomly distributed ellipsoidal Si posts with 100 nm radii of curvature and Si rectangular gratings with periods of 320 and 160 nm.

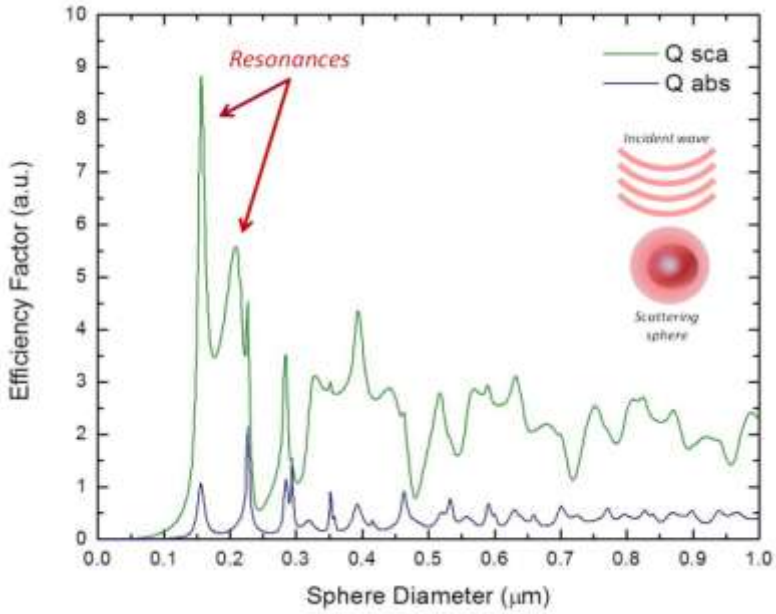

Fig. 2.25 *Plots of scattering and absorption efficiencies as function of the dielectric sphere diameter, invested by a plane wave of wavelength 632 nm.*

Nevertheless, the theoretical approach based on Eq. 2.16 is limited to a single nano-structure or nano-cluster, because it neglects the multiple scattering phenomena and the coupling process between the incident light and the nano-pattern quasi-guided modes.

As Wiersma and co-workers investigated through 3D finite-difference time-domain simulations on a pierced thin dielectric layer (section 2.3) [9], another source of field enhancement and concentration can be the in-plane multiple scattering events. In these situations, the coupling process is not merely a property of the single scatterer, but that of a network or pattern of neighbouring scatterers.

In order to investigate the interaction of light with our Si nano-structures, we employed Raman spectroscopy on lasered samples, as quantitative measurement can account for enhanced Raman scattering, if any. Raman spectroscopy was carried out with a HR800 integrated system by Horiba Jobin Yvon in a backscattering configuration. The excitation wavelength was supplied by a He-Ne laser (λ = 632.8 nm) focused on the sample with spot size of 8 μm (X50 objective, with numerical aperture of 0.75). The area sampled by the laser is well larger than the Si nano-structures size, hence, the Raman scattered light intensity is expected to be independent of the single nano-structure volume (see Fig. 2.26). In fact, Raman analyses performed in different

regions of the samples gave fair comparable results, meaning also that the patterns morphologies are quite constant inside each spots. Moreover, the intensity of the Raman laser, even if focused on micrometer spot, was low enough not to modify the Si nano-structures.

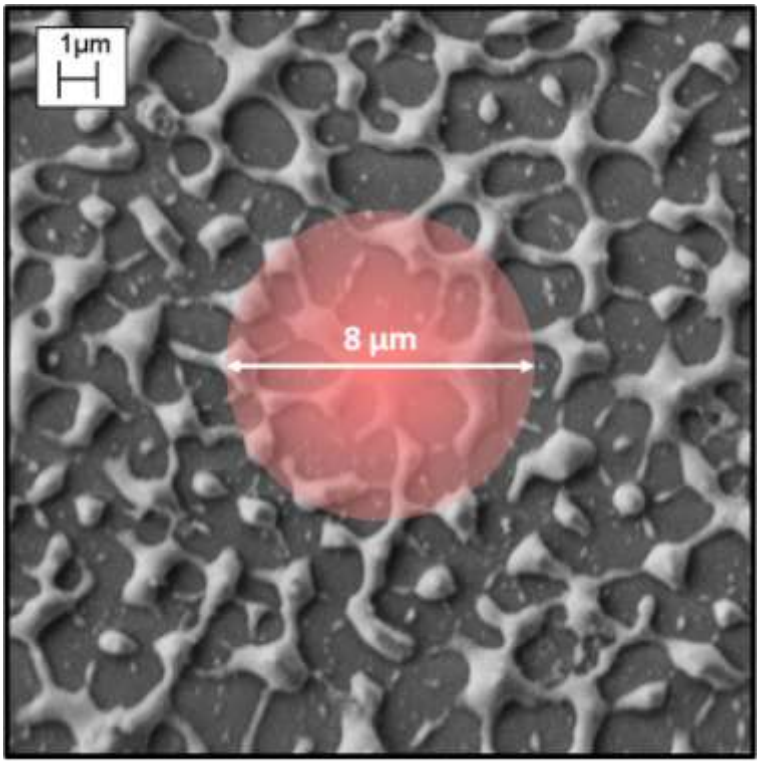

Fig. 2.26 *SEM plan view of sample **900**.The red circle indicates the laser spot size of the Raman system probe.*

A first effect is the amorphous-crystalline transition, since as-deposited film presents a large bump around 470 cm^{-1} (see Fig. 2.27), characteristic of amorphous Si, while after thermal annealing (reference sample ***ref***, Fig. 2.27) or laser processing (Figures 2.28 and 2.29) the samples present the typical crystalline Si one-phonon Raman peak, near 520.5 cm^{-1}. The crystalline Si Raman peaks relative to samples ***1130-1*** and ***1130-3*** appeared shifted to lower energies with respect to the ***900*** and ***ref*** samples, probably due to structural tensile strain or local heating of isolated particles or to different size of crystalline domains [25]. Bulk Si is not the most appropriate reference for comparison of Raman intensity among the investigated samples, since all of them are able to absorb about one tenth of the He-Ne laser beam intensity, For this reason, the 900 °C annealed sample was taken as reference for Raman scattering cross section in lasered samples. If normalized to the He-Ne laser light absorbed through its thickness, this reference sample shows a Raman peak height comparable with that of bulk crystalline Si.

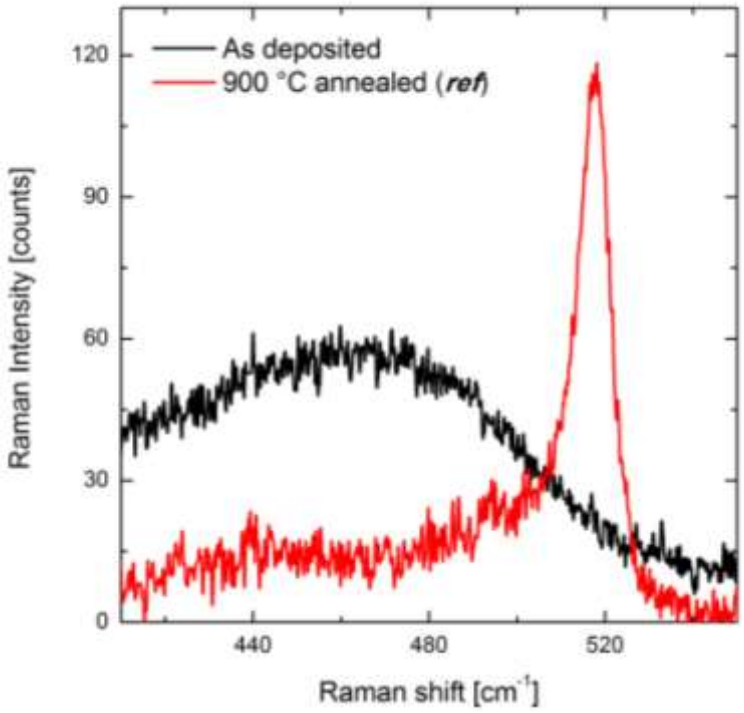

Fig. 2.27 *Raman spectroscopy on* as deposited *and* ***ref*** *sample.*

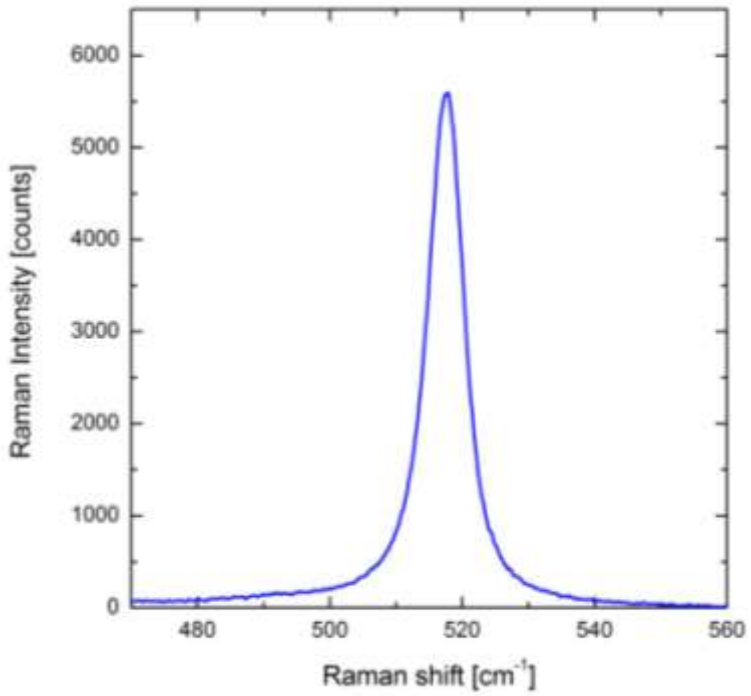

Fig. 2.28 *Raman spectroscopy on sample **900**.*

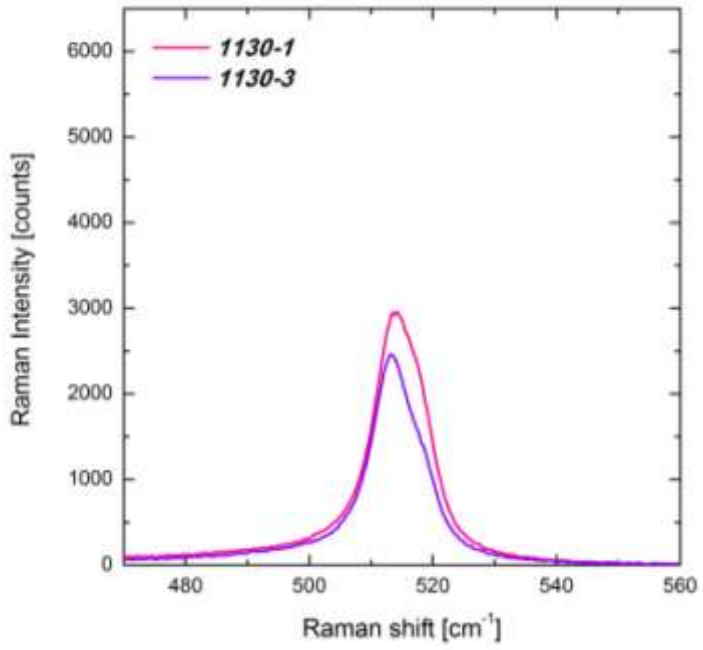

Fig. 2.29 *Raman spectroscopy on samples **1130-1** and **1130-3**.*

When a lasered sample is considered it is evident that the Raman peak height (up to 5500 count) is much higher than in the reference one (around 110 counts). In order to quantify the enhancement factor *EF* of Raman scattering cross section, the Raman intensity (peak area) has to be normalized to the scattering volume, which is proportional to the Si atomic dose *D*. Actually, slightly different Si doses are present in the samples (see table in Fig. 2.23), thus:

$$EF = {}^{I}/_{I_{ref}} \cdot {}^{D_{ref}}/_{D} \tag{2.17}$$

where *I* is the Raman intensity of lasered samples, I_{ref} is the Raman intensity of sample ***ref*** and D_{ref} its Si dose.

Sample	Raman EF
ref	*1*
900	*50*
1130-1	*20*
1130-3	*25*

Tab. 2.2 *List of the calculated enhancement factors (EF).*

The so extracted *EF* values have been reported in Tab. 2.2, showing a maximum enhancement factor of 50 in the sample with interconnected Si nano-drops. It is clear that, here, the *EF* depends on the shape, dimensions and disposition of the Si nano-structures involved in the Raman scattering process. By comparing samples ***1130-1*** and ***1130-3***, with similar *EF*, one can conclude that the small Si clusters (present only in sample ***1130-1***) do not play a significant role and that Raman enhancement should be due to strong scattering from large Si hemispheres. On the other hand, sample ***900***, with the highest value of Raman enhancement factor, presents a net-like structure, with large Si clusters often connected by narrow and sharp protuberances. This points out that interconnections should play a significant role.

Despite the fact the calculations based on Eq. 2.16 are valid only for a single Si sphere in air, they can be useful to roughly estimate the range of nano-structure dimensions at which resonances are excited for a given wavelength. From Fig. 2.20 it is evident that the sizes of our nano-structures and their features, produced by laser irradiation, fall outside the range of strong structure resonances, therefore our experimental results on enhanced Raman scattering cannot be explained by single particle Mie theory. On the other hand, due to the morphology and material similarities, the in-plane field concentration, caused by the collective multiple scattering in a pierced dielectric layer, reported by Wiersma and co-workers [9], can trustworthy justify our experimental outcomes (see Fig. 2.30).

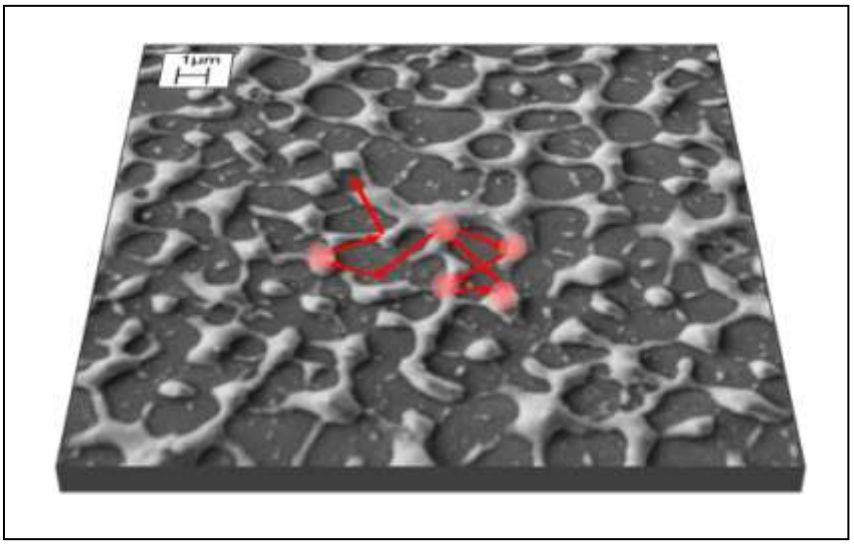

Fig. 2.30 *SEM plan view of sample **900**.The red arrows represent the in-plane light multiple scattering on the nano-structures.*

Multiple light scattering in our Si structures can be assured by measuring the fraction of direct transmitted light *T(λ)*through UV-Vis/NIR spectrophotometry. Figure 2.31 reports *T(λ)* for samples ***900*** and ***1130-1*** and for the reference one. As expected for the reference sample ***ref***, *T(λ)*is null for λ < 400 nm (due to absorption above Si band gap), while for longer wavelength the interface pattern gives account for the continuous film structure. In lasered samples no interface appears (as films are broken), and an almost flat transmittance comes out, also for λ < 400 nm where all photons should be absorbed except those passing through the holes of the film. In lasered samples, the uncovered fraction area (where holes are present) is larger than 60% (as measured by the SEM images), which should give, for λ < 400 nm, *T(λ)*values much higher than what measured (30% or 20% in ***1130-1*** or ***900*** samples, repsectively). This evidence claims for efficient light multiple scattering stimulated by Si structures and holes.

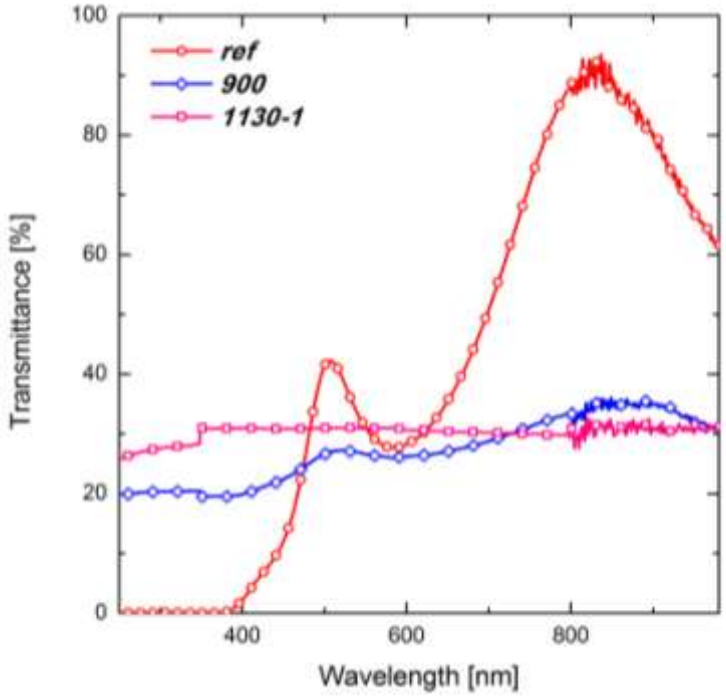

Fig. 2.31 *Direct transmittance spectra for samples **ref**, **900** and **1130-1**.*

2.9 - Conclusions

In the first section (2.5) dedicated to the experimental work on light trapping, it has been shown that dense Si NWs, synthesized by metal-induced CVD growth, present strongly reduced total reflectance $R_t(\lambda)$ along a wide wavelength range, that is of great interest for solar cells. In particular, the $R_t(\lambda)$ at λ = 500 nm, which is the peak of the solar spectrum irradiance, falls to the small values (10% - 20%) generally obtained by means of the best optimized ARCs [3]. The great advantage of such property is that if these Si NWs are used as the active part in a solar cell , they already own efficacious anti-reflection ability, without the need of being covered by a dedicated material. Moreover, in the fabricated Si NWs, the great decrease of $R_t(\lambda)$ and the vanishing of its specular component are ascribed to the strong light diffusion and trapping, owing to the multiple scattering events occurring when light meets the tangled Si NWs.

While, in the following section (2.8), it has been reported an unprecedented methodology for low-cost fabrication of Si nano-structures able to enhance light scattering and trapping phenomena. The formation of Si nano-structures, based on sputtering and pulsed laser irradiation in air ambient of thin Si film, is compatible with dewetting process, whose kinetics can be modulated by the laser fluence producing from still interconnected to well isolated Si nano-clusters. The intensity of Raman scattering from these Si nano-structures has been evaluated, demonstrating a large enhancement up to a factor of 50, particularly in the early stage of the dewetting process where an interconnected Si structure is produced. Light trapping in this structure, due to collective multiple scattering and interference effects (wave optic regime), is proposed to explain the observed enhanced Raman scattering.

Bibliography

[1] E. Yablonovitch, Journal of Optical Society of America, Vol. 72, No. 7, (1982)

[2] Physics of Solar Cells; From Principles to New Concepts - P. Würfel - Wiley-VCH (2005)

[3] J. Zhao and M. A. Green, IEEE Transactions on Electron Devices, Vol. 38, No. 8, (1991)

[4] S. B. Mallick, N. P. Sergeant, M. Agrawal, J.-Y. Lee and P. Peumans, MRS Bulletin, Vol. 36, (2011)

[5] A. Polman and H. A. Atwater, Nature Materials, Vol. 11, (March 2012)

[6] ARC Photovoltaics Centre of Excellence - Annual Report (2009).

[7] Photonic Crystals, Molding the Flow of Light - J. D. Joannopoulos, S. G: Johnson, J. N. Winn, R. D. Meade - Princeton University Press (2008)

[8] E. R. Martins, J. Li, Y.-K. Liu, J. Zhou and T. F. Krauss, Physical Review B, **81**, 041404 (R), (2012)

[9] K. Vynck, M. Burresi, F. Riboli, and D. S. Wiersma, Nature Materials, Vol. 11, (December 2012)

[10] Y. E. Geints, E. K. Panina, A. A. Zemlyanov, Optics Communications 283, 4775-4781, (2010)

[11] M. D. Migliore, IEEE Transactions on Antennas and Propagation, Vol. 56, No. 10, (2008)

[12] Plasmonic, Fundamentals and Applications - S. A. Maier - Springer (2007)

[13] H. A. Atwater and A. Polman, Nature Materials, Vol. 9, (March 2010)

[14] S. Chou, P. Krauss, W. Zhang, L. Guo and L. Zhuang; Journal of Vacuum Science & Technology B **15**, 2897 (1997)

[15] C. Garozzo, A. La Magna, G. Mannino, V. Privitera, S. Scalese, P. M. Sberna, F. Simone, R. A. Puglisi, Journal of Applied Physics **113**, 214313 (2013)

[16] C. Favazza, R. Klyanaraman and R. Sureshkumar, Nanotechnology, **17**, 4229-4234, (2006)

[17] R. Seemann, S, Herminghaus, K. Jacobs, Physical Review Letters, Vol. 86, No. 24, (2001)

[18] U. Thiele and M. G. Velarde, Physical Review Letters, Vol. 87, No. 1, (2001)

[19] I. Berbezier, M. Aouassa, A. Ronda, L. Favre, M. Bollani et al., Journal of Applied Physics **113**, 064908, (2013)

[20] P. M. Sberna, G. G. Scapellato, N. Piluso, S. Boninelli, M. Miritello et al., Applied Physics Letters **103**, 221902 (2013)

[21] Handbook of Photovoltaic Science and engineering - A. Luque and S. Hegedus - Wiley (2003)

[22] M. Mayer, AIP Conference Proceeding **475**, 541 (1999)

[23] D. V. Murphy and S. R. J. Brueck, Optics Letters, Vol. 8, No. 9, (1983)

[24] MiePlot v4.3 - P. Laven - http://www.philiplaven.com/mieplot.htm

[25] M. N. Islam and S. Kumar, Applied Physics Letters **78**, 715 (2001)

3 - CUPROUS OXIDE

3.1 - Introduction

At the beginning of the last century, cuprous oxide was the first compound known to have semiconducting characteristics. During the twenties, rectifiers diodes, containing this oxide, were industrially produced, albeit their life cycle was too short. At that time Cu_2O potential for photovoltaic applications was foreseen; however, when in the early fifties, a fine and advanced control of Si and Ge synthesis and doping was achieved, the attention on Cu_2O relentlessly declined in favor of the former materials. Later, while the oil crisis in the seventies was shading a negative light on fossil fuel sources, the interest on Cu_2O as absorber layer in low-cost solar cells arose again [1] and it continued to grow until present days. Especially in the last ten years, Cu_2O became even one of the major candidates for thin-film solar cells, mainly due to the fact that recent advances in synthesis techniques and the development of novel chemical deposition methods, opened up the road for a large scale and cheap production of devices based on such abundant and non-toxic material.

The range of application of Cu_2O in solar cells is wide, since it embraces three categories:

1. Conventional structure cells: they are p-n hetero-junctions (see Fig. 1.4-c), where the Cu_2O layer is the p-type absorbing layer and an n-type oxide (such as ZnO, In_2O_3, SnO_2, CdO and Ga_2O_3) thin film serves as window layer on the cell front [2]. The maximum theoretical efficiency is 20%, because the material band gap does not perfectly match the solar spectrum peak [1]. Taking into account the principal deleterious phenomena that increase the saturation current J_0 (and in turn, reduce V_{oc} and the overall efficiency), i.e. recombination centers at the junction and the injection of minority charge carriers, the cell efficiency drops to 17% [1]. The highest Cu_2O hetero-junction experimental efficiencies were reported by Minami and co-workers. The record values of 5.83% and 3.83% were achieved by these authors, respectively, for the hetero-junctions Ga_2O_3 / Cu_2O and ZnO / Cu_2O [3] [4].
2. Polycrystalline multi-junction cells: they are tandem or triple junctions made from CIGS alloys and Cu_2O, which is the absorber of the top cell, thanks to the high value of its band gap (2.1 eV) [1].
3. Intermediate band cells: they are simple hetero-junctions, but the absorber layer has an intermediate narrow band of states in the middle of its band gap.

This intermediate band comes out when the doping concentration is sufficiently high and the introduced defects levels overlap, forming a band of electronic states. In this way the absorption of photons with energy lower than the original band gap can be accomplished by a two steps mechanism. According to theoretical studies, one of the optimal materials, due to its band gap value, to accommodate an efficient intermediate band is Cu_2O [1].

Since the efficiencies of conventional Cu_2O based cells are too much below the highest possible limit, the advanced applications of points *2.* and *3.* are only nice outlooks. The road towards a complete and determinant optimization of Cu_2O for solar cells, is still long and any advances in this direction is slowed down by the lack of a deep and coherent insight of its point defects and related electronic properties.

A systematic investigation into each loss mechanism involved in Cu_2O based hetero-junctions leads to the following considerations:

- Low conductivity of Cu_2O films causes large values of cell series resistance. To overcome this problem one should increase the film conductivity, for example, by doping, without reducing the minority charge carriers lifetime.
- High resistivity metal/Cu_2O contacts cause large power losses in the cell. The solution is to succeed in forming low resistivity ohmic contacts, using metals with high work function (to minimize the Schottky barrier height) and with low reactivity with Cu_2O, in order to avoid the generation of metallic copper at the contact interface by means of spontaneous reduction [5]. Furthermore, it is fundamental to deposit this metal contact on a low resistivity Cu_2O area [5].
- When the material used for the window layer has a high band gap, non-ideal band alignment at the junction with the adjacent Cu_2O layer can occur. This fact causes the formation of a potential barrier for the photo-generated charges, that, consequently, undergo fast recombination at the junction interface. Macroscopically this phenomenon results in a large decrease of V_{oc}. In order to avoid this recombination source, it is mandatory to grow between Cu_2O and the window material a buffer layer, such as TiO_2, amorphous Zinc-Tin oxide or Ga_2O_3, to provide better band alignment [6].
- Generally, with all the deposition techniques, the junction interface has a high concentration of defects, which act as trap states for the photo-generated charge carriers. In particular, the formation of a nanometric CuO layer on Cu_2O surface (on which the window layer is later grown), introduces deep trap states in the band gap. If proper chemical treatments and etching are not performed before the deposition of the n-type film, the cell will have low performances. Even though post-deposition chemical treatments are able to

remove the undesired CuO superficial layer, the high rate of Cu_2O oxidation into CuO, even at standard conditions, induces, anyway, the formation of nanometric CuO domains on the surface. To overcome such a big issue, it is necessary to keep the Cu_2O surface modification under control during the fabrication of the cell. Recently, it has been reported that a deep ad smart control on the Atomic Layer Deposition (ALD) reaction conditions allows to tune the chemical state of the junction interfacial layer [6]

Each of these issues still demands deeper analysis and understanding, leaving a wide range of possibilities for further theoretical and experimental investigations.

Moreover, cuprous oxide, due to its physical properties, is considered a versatile compound, with the possibility to become a key material in emerging technologies such as transparent electronics [7] and photo-catalysis for H_2 production [8] [9].

3.2 - Bulk properties

Cuprous oxide crystallizes in a cubic structure (see Fig. 3.1 - a) with cell parameter a = 4.27 Å. Cu_2O lattice can be ideally divided in two sub-lattices, a face centred cubic (fcc) lattice of Cu cations (see Fig. 3.1 - b), where O atoms occupy tetrahedral interstitial sites, and a body centred cubic (bcc) lattice of O anions (see Fig. 3.1 - c), where Cu atoms form O - Cu - O ribbons (connecting the central O atom with the corner O atoms). It comes out that in this kind of crystalline structure, oxygen has a coordination number equal to four and copper equal to two, which is an unusual value for the cation in metal oxides.

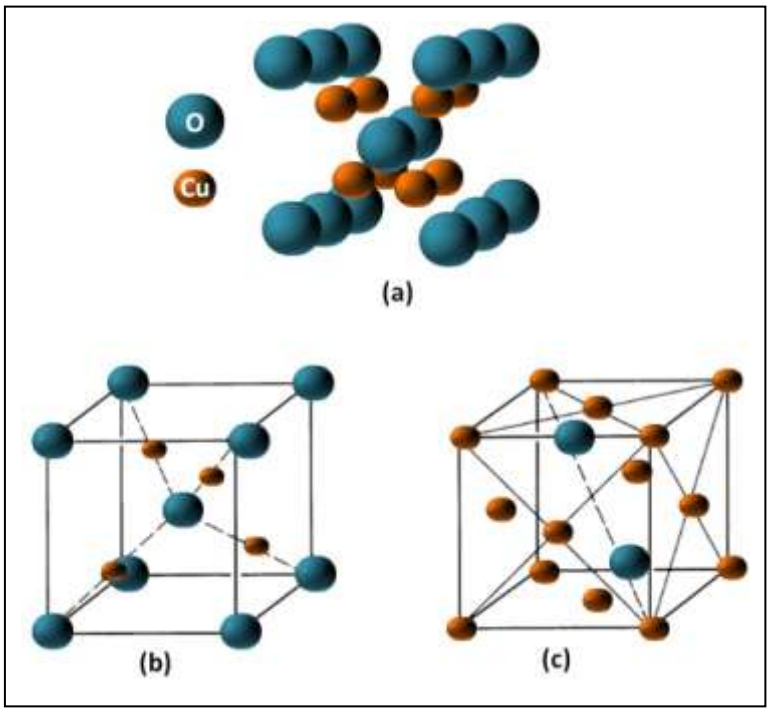

Fig. 3.1 *(a) Cu_2O cubic lattice, (b) Cu fcc sub-lattice and (c) O bcc sub-lattice.*

If the total lattice is properly rotated, it is easy to realize that the structure consists of two interpenetrating Cu_2O networks (see Fig. 3.2) with anti-cristobalite (Si_2O) atomic arrangement. Each network is held together by ionic-covalent bond between O^{-2} and Cu^{+1} ions, whereas there is not any chemical bond linking the two networks [10]. The two interpenetrating Cu_2O structures are loosely bound together by dispersive Cu - Cu electrostatic (van der Waals-like) interactions, involving the copper orbitals *3d*, *4s* and *4p* [10]. The weakness of such bonds makes it easier to displace one network with respect to the other than to modify the Cu - O bond length. As it will be discussed in the following sections, disruption of internetwork Cu - Cu interactions causes changes in material optical properties [11].

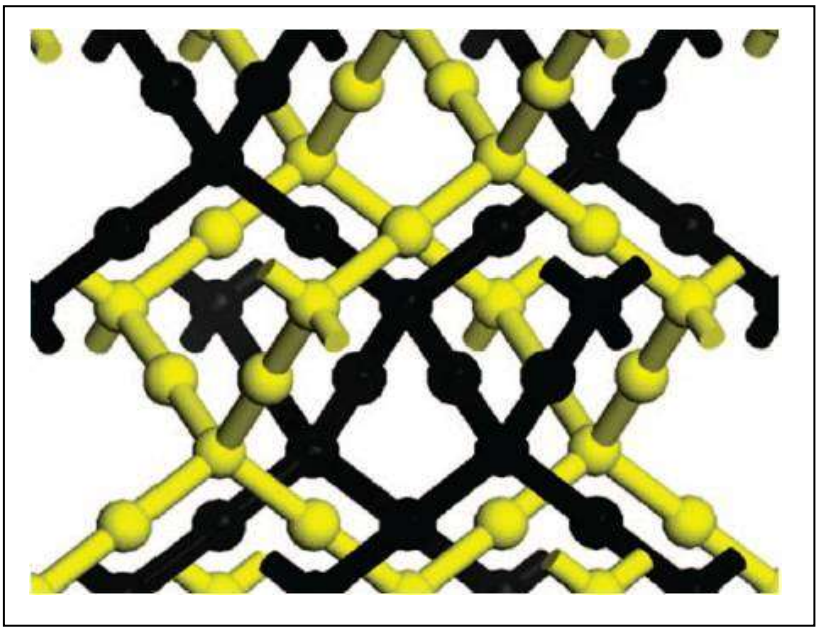

Fig. 3.2 *Cu_2O interpenetrating networks, respectively depicted in yellow and black (image taken from Ref. [11]).*

In cuprous oxide, the ionic bonds occur between the ion Cu^{+}, whose electronic structure ends $3d^{10}$ - $4s^{0}$, and the anion O^{-2}. The Cu *3d* full levels, undergoing hybridization with the oxygen *2p* orbitals, give birth to the valence band (VB). However, the copper orbitals contribution dominates at the higher valence band levels. The Cu_2O valence band is six-fold degenerate, but the spin orbit coupling lifts such degeneracy, separating two states from the other four ones (133.8 meV of difference) [1]. On the other hand, the empty Cu *4s* and *4p* levels form, respectively, the lowest and the higher conduction bands. The bands edges maxima and minima are at the center of the Brillouin zone (point *Γ*), meaning that Cu_2O is a direct gap material. The band structure *E(k)* is reported in Fig. 3.3.

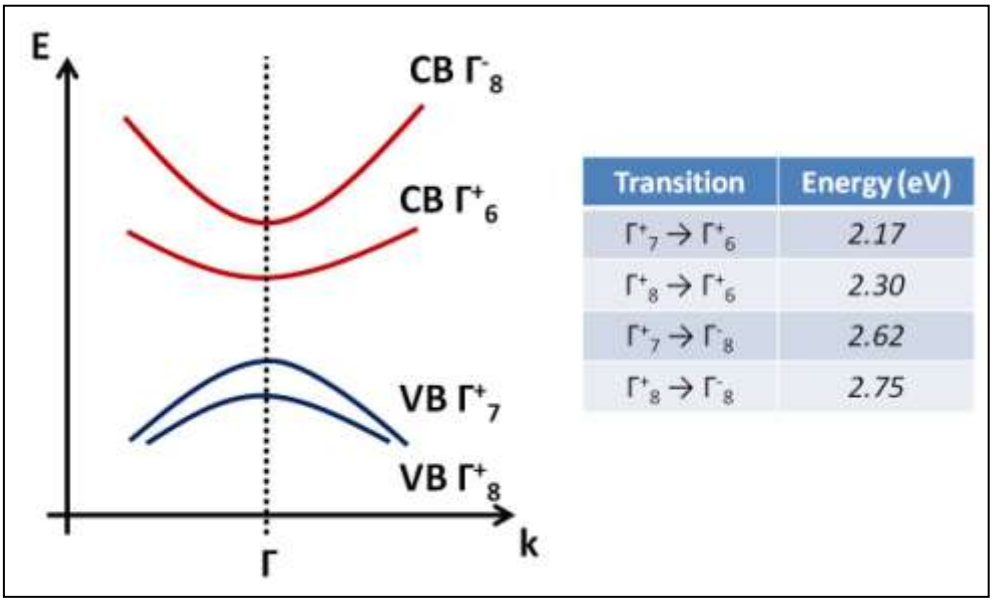

Transition	Energy (eV)
$\Gamma^{+}_{7} \rightarrow \Gamma^{+}_{6}$	2.17
$\Gamma^{+}_{8} \rightarrow \Gamma^{+}_{6}$	2.30
$\Gamma^{+}_{7} \rightarrow \Gamma^{-}_{8}$	2.62
$\Gamma^{+}_{8} \rightarrow \Gamma^{-}_{8}$	2.75

Fig. 3.3 *Cu_2O band structure (left side) and energies of the various inter-band transitions at a temperature of 4.2 K (right side).*

Since the two valence bands and the lowest conduction band have the same parity, the transition between them are not dipole-allowed. The electrical transitions from the valence bands levels to the upper conduction band states are direct allowed instead. For these reasons, for photon energies below 2.4 eV [1], the absorption coefficient α is proportional to $(\hbar\omega - E_g)^{3/2}$, that is, it increases very slowly with energy $\hbar\omega$. As a result, direct forbidden absorption edges are not generally easy to observe. Nevertheless, at low temperature, near the absorption edge a series of strong excitonic peaks emerges. Recently, Malerba and co-workers demonstrated that, just above the optical band gap of 2.17 eV, the energy dependence of absorption

coefficient deviates from $(\hbar\omega - E_g)^{3/2}$ due to the existence of several different absorption mechanisms, i. e. indirect transitions and excitonic contributions [12]. For photon energies higher than 2.4 eV, the absorption coefficient is proportional to $(\hbar\omega - E_g)^{1/2}$. In this case the dependence of α on $\hbar\omega$ is stronger, thus the direct allowed optical band gap of 2.6 eV is easily observed (for bulk Cu_2O) [1].

Since for Cu_2O, in contrast with most of the metal oxides, the valence band comes mainly from the more diffused and less directional Cu *d* orbitals, instead of oxygen *p* orbitals, the hole effective mass is lower. This fact gives, in turn, to cuprous oxide a higher hole mobility compared with the majority of metal oxides, such as ZnO and SnO_2 [13], making Cu_2O a promising material as p-type absorber layer in hetero-junction cells and for transparent electronic implementation in C-MOS technology [13].

Point defects, induced by thermal disorder or by non-stoichiometry, greatly influence Cu_2O physical properties. At equilibrium, for certain oxygen partial pressure and temperature, there is a fixed point defects concentration. However deviation from the equilibrium values may be produced by sudden temperature changes, mechanical deformation, irradiation or impurities incorporation. Such high variability makes Cu_2O optical and electrical properties greatly dependent on synthesis conditions.

The intrinsic point defects can be copper vacancies (V_{Cu}), oxygen vacancies (V_O), interstitial copper atoms (Cu_i), interstitial oxygen atoms (O_i) and anti-site defects (Cu_O and O_{Cu}). Furthermore, the lattice can contain defects complexes, which are a combination of two of the previously listed defects (i.e. V_{Cu} - V_O [14]). Each point defect can exist either in neutral (*) or charged (+*n*, -*m*) state (for example V^*_{Cu} and V^-_{Cu}) and the lattice generally can accommodate both species.

Porat and Riess [15] performed comprehensive experimental investigations on the stoichiometry deviation of Cu_2O as function of external oxygen partial pressure p_{O2} and temperature *T*.

Their data analysis showed that:

- for low p_{O2} the principal defect is Cu^*_i at low *T* and V^*_O at high *T*;
- for high p_{O2} (also atmospheric) the dominant defect, regardless of *T*, is V^*_{Cu}.

Therefore, it has been experimentally demonstrated that Cu_2O, at standard conditions, is intrinsically copper-deficient. This fact is coherent with structural inorganic chemistry, which states that a metal oxide will be naturally cation-deficient if its cation is oxidizable (i. e. Cu^+ in Cu^{+2}) [1].

Copper vacancy can assume two different configurations, respectively simple (V_{Cu}) and "split" (V^{s}_{Cu}). Simple V_{Cu}, created by removing a Cu atom, has two neighboring triply coordinated (instead of four) O atoms; while V^{s}_{Cu} is formed when a nearby Cu atom shifts toward the vacancy site and bonds with four O atoms [16] (see Fig. 3.4).

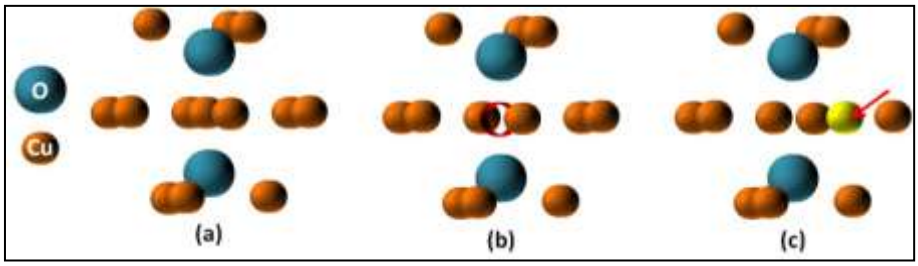

Fig. 3.4 *a) regular Cu_2O lattice, b) simple copper vacancy (red circle), c) split copper vacancy (the relaxed Cu atom in yellow).*

In literature, the experimental formation enthalpy of copper vacancy spans over the range between 0.39 and 0.97 eV/defect [16]. It has been pointed out that such variability comes from the fact that the samples analyzed in the various studies were prepared at different conditions.

Furthermore, one of the most recent and accurate theoretical study [16] reported that the split vacancy should be less stable than the simple vacancy. In fact, it was calculated, for V^{s}_{Cu}, a formation enthalpy 0.21 eV smaller in respect to the simple V_{Cu}. Since the formation enthalpies of the two kind of copper vacancies slightly differ, both defects can exists in a sample. On the other hand, certain synthesis methods, post-deposition treatments or doping may favor the generation of one type of vacancy.

Cuprous oxide is a natural p-type semiconductor because the dominant charged defects are ionized copper vacancies (V^{-}_{Cu}) [17], which introduce shallow acceptor states in the band gap. Analyzing the curve of conductivity as a function of temperature (between 100 and 400 K), Brattain calculated that this acceptor state is 0.3 eV above the valence band maximum (VBM) [18]. Moreover, by means of capacitance-voltage measurements on Cu_2O-based Schottky junctions, he realized also that cuprous oxide is a compensated semiconductor, that is, along with acceptor states, a slightly smaller density of donor states exists. According to Brattain's studies [18], the donor states are 2 eV above the VBM (see Fig. 3.5).

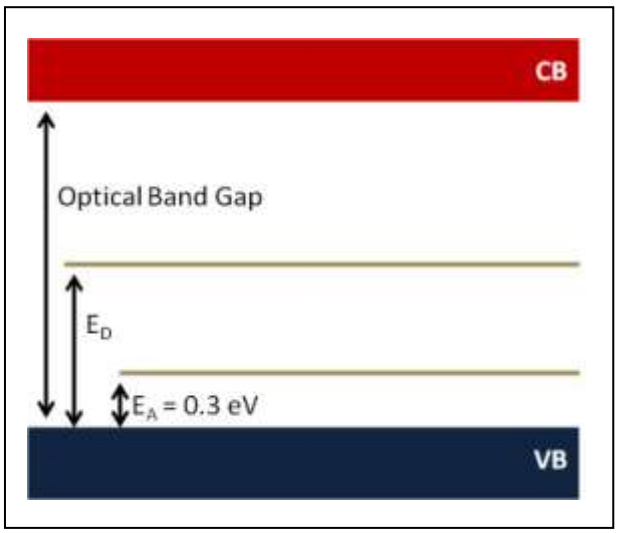

Fig. 3.5 *Cu_2O band scheme according to Brattain [18].*

After the pioneering work of Brattain, the conductivity measurements as a function of temperature on Cu_2O single-crystal, reported in Ref. [19] and [20], revealed a much more complex electronic structure for this material. In fact, it was reported that the ionization energy of V^{*}_{Cu} (which is related to the acceptor state position in the gap), at low temperatures, ranges between 0.2 and 0.5 eV (see Fig. 3.6), strongly depending on the sample preparation conditions. Furthermore, absorption and photoconductivity measurements revealed that the acceptor state introduced by V_{Cu} lies between 0.55 and 0.61 eV above the VBM [16].

A partial explanation for these scattered results could come from a recent study based on density functional theory (DFT) by Isseroff and Carter [16]. The authors, analyzing the electronic density of states in the Cu_2O band gap, realized that the split vacancy, V^{s}_{Cu}, introduces a single acceptor state about 0.55 eV above the VBM, while, the simple vacancy, V_{Cu}, generates a small band of states around the Fermi level, below the V^{s}_{Cu} state. This V^{s}_{Cu} state position in the gap is, indeed, consistent with the level experimentally identified between 0.55 and 0.61 eV. Whereas, the small band of states, generated by simple vacancies, can be related to the range of acceptor states designated by Brattain [18], O'Keeffe [19] and Bloem [20].

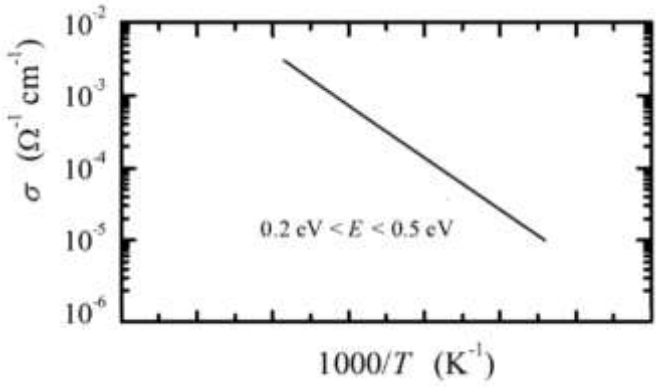

Fig. 3.6 *Conductivity of Cu_2O single crystal as a function of temperature (taken from Ref. [19]).*

Due to the structure of the electronic density of states calculated by Isseroff and Carter [16], the hole provided by V^{s}_{Cu} is strongly localized around the defect, whereas, in the case of simple V_{Cu}, it extends to some of the Cu atoms nearby the vacancy.

This fact means that the defect generated by V^{s}_{Cu} acts as a trap state for electrons [16]. Therefore, the formation of V^{s}_{Cu} increases the minority charge carriers recombination rate, limiting the Cu_2O photo-conductivity. For well performing solar cells, based on Cu_2O thin films, it would be, thus, preferable to have simple V_{Cu} as dominant vacancies.

3.3 - Thin-films deposition methods

One of the characteristics that makes Cu_2O a versatile material is the ease to deposit it utilizing various techniques, spanning from physical methods, as sputtering, to chemical techniques, such as spray pyrolysis and hydrothermal bath. Each method, shows some advantages, compared to the others as well as, certain drawbacks. The best choice among these deposition techniques has to take into account, not only the synthesis of a good quality Cu_2O film, but also its efficient implementation in a well performing solar cell. Indeed, cell production demands several thin-films deposition steps, generally employing different methods, therefore the technique chosen for the synthesis of Cu_2O layer ought to suite to the overall fabrication process.

- The simplest way to produce micrometric polycrystalline Cu_2O films is oxidizing a copper thin sheet in oxygen atmosphere at elevated temperatures (about 300-1000 °C) for hours.
  Cuprous oxide films produced by thermal oxidation have very large grains, ranging between 1 and 100 mm^2. Mainly for this reason, the hole mobility typically reaches the stunning value of about 100 $cm^2/V{\cdot}s$. However, the hole densities are generally low (of the order of 10^{13} cm^{-3}), making the films resistivity to stuck at too high values (10^3 - 10^4 $\Omega{\cdot}cm$) to obtain high fill factor for solar cells [21]. As regards the optical properties, it was measured a direct optical band gap of 2.1 eV [12].
  Although this technique is simple, it requires, as starting material, a ultra pure Cu foil and does not allow an accurate control of doping and oxidation state at the nanometric scale. However, the ZnO/Cu_2O hetero-junction with the highest reported solar to electric power conversion efficiency (3.83%) has been realized by Minami and co-workers [4], synthesizing Cu_2O absorbing layer by furnace thermal oxidation.

- Cuprous oxide thin films can be also synthesized by sputtering Cu_2O or Cu targets on different substrates, such as glass and polymeric foils; indeed one of the great advantages of this technique is the possibility to deposit, even at low temperatures (< 100 °C), Cu_2O thin films with good electrical qualities [22].
  Unlike the previous technique, sputtering allows effective control of the film chemical composition and high deposition rates. Nevertheless, all these advantages cost the high increase of film production price, due to the required high vacuum system.
  If the deposition conditions are properly optimized, sputtered Cu_2O thin films have mobility in the range between 1 and 10 $cm^2/V{\cdot}s$ [23]. Furthermore, it is easy to generate high concentrations of copper vacancies, thus the typical resistivity is

between 1 and 10^3 Ω·cm [23]. While, the direct optical band gap, experimentally measured from Tauc plots, falls in the range 2.1 - 2.6 eV [24] [25].

- Electro-deposition has always been considered a potential candidate for cheap and environmental-friendly Cu_2O synthesis. In this case, Cu_2O is deposited at low bath temperatures (< 100°C) on a conductive substrate.
  Due to the solution based growth, the film electrical quality is lower in respect to the one obtained by the previous techniques. On the other hand, the low bath temperature allows also the formation of nano-structured Cu_2O layers, since the self-organization driving forces prevail on the thermal disorder. The production, by electro-deposition, of Cu_2O nano-structures with high aspect ratio opened up the possibility to obtain nano-structured p-n hetero-junctions with large effective area [23]. Solar cells with this kind of architecture would have good performances, in spite of containing low quality absorber material, because photo-charges collection occurs in few nanometers. Moreover, electro-deposition allows to grow Cu_2O inside nano-porous matrixes [26].

- Spray pyrolysis is another cost-effective and green chemical technique suitable to design nanometric Cu_2O films on molecular level and it is able to perform large scale depositions on various substrates. The typical equipment includes a moving atomizer and a substrate heater. The deposition of Cu_2O thin films consists of a programmed repetition of spray cycles, each involving the following steps:

  1. a precursor solution of copper based salts (either inorganic or organic) is atomized in small droplets by the vibrating atomizer;
  2. the aero-sol, formed at the exit of the atomizer, is conveyed, by a carrier gas (compressed air or nitrogen jet) onto the heated substrate;
  3. the solution droplets impact on the substrate surface and spread into a disk. Once deposited on the hot surface, the chemical species undergo pyrolysis and oxi-reduction reactions, forming a ultra-thin copper oxide layer, while the solvent evaporates together with the by-products. The final film is composed of overlapping layers, deposited at each spray cycle.

     Cuprous oxide thin films, deposited by spray pyrolysis, commonly show an optical band gap around 2.6 eV [27] and have the electrical resistivity ranging between 10^2 and 10^3 Ω·cm [27] [28]. Even though spray pyrolysis is a solution based method, the reported Cu_2O films mobility can reach considerable values between 1 and 6 $cm^2/V{\cdot}s$ [28].

3.4 - Doping: an overview

The introduction of foreign atoms in Cu_2O can modify significantly the physical properties of the semiconductor. The oxide characteristics that can be, in principle, altered by doping are electrical conductivity, type of majority charge carriers, optical absorption, minority charge carriers mobility and oxidation state of copper atoms.

These possible doping effects, are important goals to improve the quality of photovoltaic cells based on Cu_2O. Indeed, a p-type doped Cu_2O film, having low resistivity, is a key component for solar cells with high fill factor and short circuit current. On the other hand, n-type Cu_2O permits the fabrication of homo-junctions, which, compared to hetero-junctions, would contain less interfacial defects. Moreover, doped Cu_2O films, with improved charge carriers life-time, allow the fabrication of cells with lower non-radiative recombination rates.

3.4.a - Electrical conductivity modulation by doping

Hole density can be increased, for example, doping Cu_2O with nitrogen atoms, which, having oxidation state *-3* and if substitute oxygen atoms, behave as acceptors. This was experimentally observed by Ishizuka and co-workers [29], who deposited Cu_2O thin films by RF magnetron sputtering in O_2/N_2 atmosphere. The electrical characterization of their samples, revealed that the hole density, thanks to nitrogen doping, increased from 10^{15} cm^{-3} (undoped concentration) to a maximum of about 10^{17} cm^{-3} (see Fig. 3.7), accompanied by a resistivity maximum reduction of one order of magnitude. Furthermore, they observed that nitrogen introduces an acceptor level at 0.14 eV above the VBM, in accordance with the theoretical model considering nitrogen that substitutes oxygen [1]

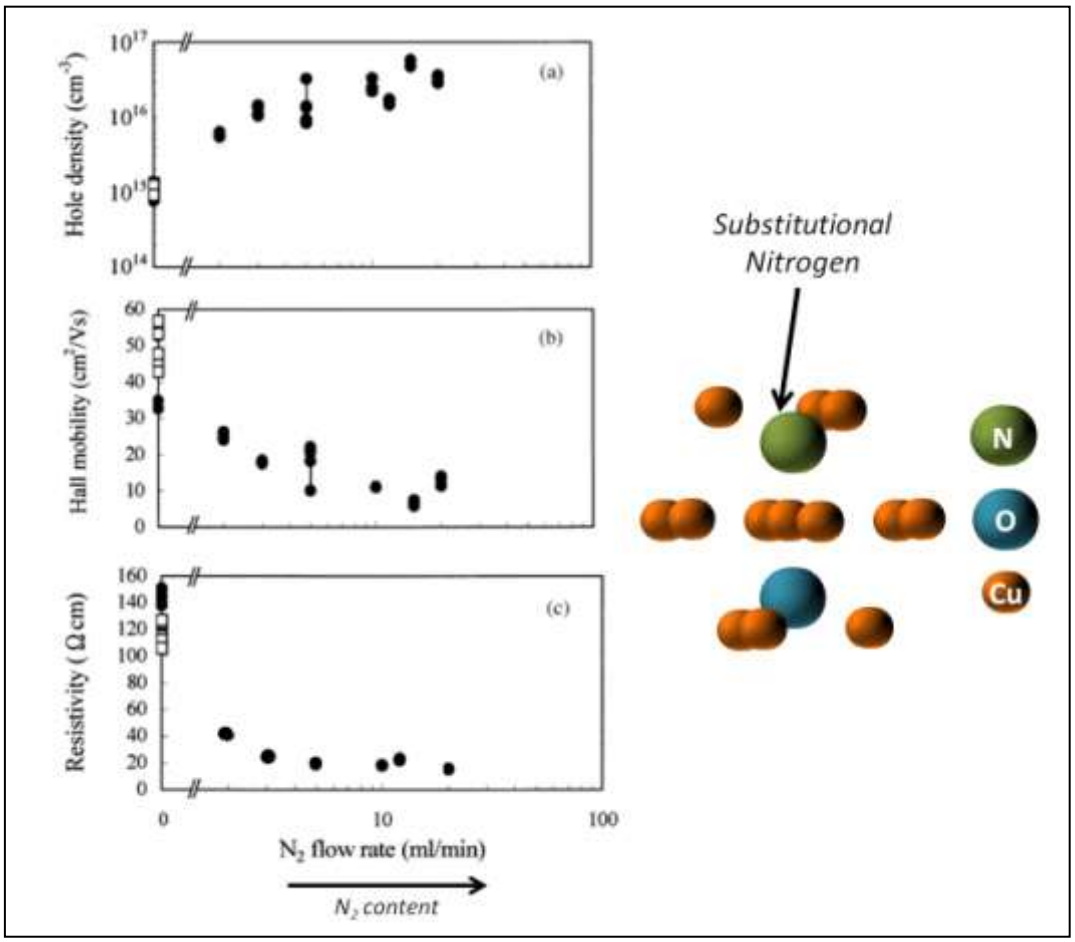

Fig. 3.7 *a) Hole density, b) hole mobility and c) resistivity for Cu_2O thin films deposited by sputtering at various N_2 flow rates (taken from Ref. [29]).*

3.4.b - n-type doping

In principle, n-type doping of Cu_2O occurs when cations with oxidation states higher than *+1* (aliovalent dopants) substitute copper atoms, or if the dopants are stabilized at interstitial sites, creating negatively charged point defects, that act as donors.

The formation energy $\Delta H_f(D)$ of defect states in Cu_2O can be calculated by *ab-initio* methods (density functional theory approaches) according to this formula:

$$\Delta H_f(D) = E(D) - E_{ref} + \sum_i n_i \cdot \mu_i + q(E_V - \Delta E_f) \quad (3.1)$$

where *E(D)* is the total energy of the super-cell containing the defects, E_{ref} is the total energy of the stoichiometric super-cell, n_i is the number of atoms (constituent and impurities) removed or added (in this case the sign becomes negative) to the host super-cell to create the defects, μ_i is the chemical potential of the atom removed or added, q is the charge state of the point defect, E_V is the valence band edge energy and ΔE_f is the Fermi energy shift. A defect state is spontaneously created if $\Delta H_f(D)$ is negative and it is easily formed if, in spite of being positive, is small. The value of $\Delta H_f(D)$ depends on the system energy costs to accommodate the point defect in its structure (accounted by *E(D)*), on the growth conditions (reflected by μ_i) and on the position of the Fermi energy shift induced by doping.

Obviously, an impurity will occupy the least energetic-costly (thus the most thermodynamically favored) lattice sites (i.e. substitutional or interstitials).

The ability to dope a material, in general, can be limited by the ease of the system to generate compensating native defects, whose formation energy is also calculated by Eq. (3.1) but setting:

$$2 \cdot \mu_{Cu} + \mu_O = \mu_{Cu_2O} \tag{3.2}$$

for the most common Cu_2O synthesis processes (vacuum-based and spray pyrolysis).

In the specific case of cuprous oxide, grown at conditions described by Eq. (3.2), shifting the Fermi level towards the conduction band (as a consequence of n-type doping) leads to negative formation energy for copper vacancies, which are acceptor states (see Fig. 3.8) [30] [1]. Therefore, the electrons provided by the impurity donor states will be compensated by the holes supplied by the spontaneously generated V_{Cu}. As can be seen from Fig. 3.8, the V_{Cu} formation energy becomes negative when the Fermi level reaches just the middle of the band gap (about 1 eV), thus, it is impossible to achieve n-type doping in Cu_2O synthesized by thermal oxidation, sputtering and spray pyrolysis.

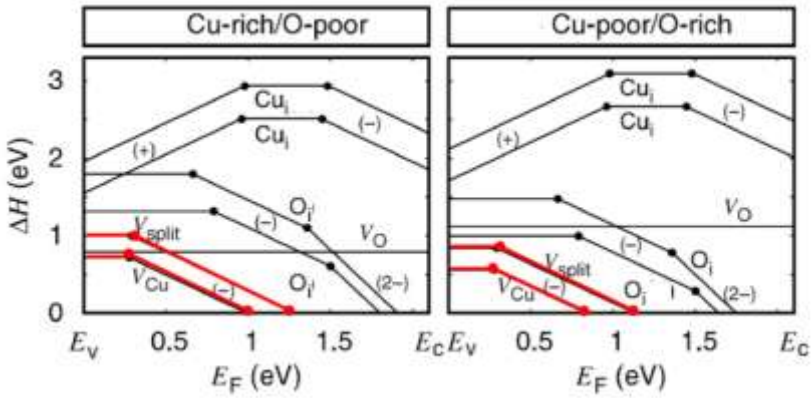

Fig. 3.8 *Calculated formation energies of defects in Cu_2O (grown at Cu-rich and Cu-poor conditions) as a function of Fermi level position (taken from Ref. [1]).*

Similarly, Nolan and Elliott [11], using a theoretical approach based on density functional theory and on Eq. 3.1 and 3.2, calculated the formation energies of the first compensating copper vacancy for several aliovalent cation dopants (see Tab. 3.1).

Dopant Cation	V_{Cu} ΔH (eV)
Sn^{+2}	-0.95
Zn^{+2}	-0.78
Mg^{+2}	-0.46
Ca^{+2}	-0.62
Sr^{+2}	-0.65
La^{+3}	-0.76

Tab. 3.1 *Formation energies of the first compensating copper vacancy for some aliovalent cation dopants, calculated by Nolan and Elliott [11].*

For divalent cations, the compensating vacancy is only one, while for cations with oxidation states *+n*, the first compensating vacancy is the $(n-1)^{th}$.

All the formation energies, calculated by Nolan and Elliott, are negative or extremely small, demonstrating that n-type doping is not feasible under the most common cuprous oxide synthesis conditions, owing to the compensation mechanism.

Moreover, these authors [11] computed also the formation energies of the consecutive copper vacancy (see Tab. 3.2), which, being the donor already compensated, dopes the system p-type.

Dopant Cation	V_{Cu} ΔH (eV)
Sn^{+2}	*0.15*
Zn^{+2}	*0.22*
Mg^{+2}	*0.26*
Ca^{+2}	*0.23*
Sr^{+2}	*0.14*
La^{+3}	*-0.57*

Tab. 3.2 *Formation energies of the copper vacancy, consecutive to the first compensating, for some aliovalent cation dopants, calculated by Nolan and Elliott [11].*

Even though some of the formation energies listed above are not negative, their values are comparable with the V_{Cu} formation energy for undoped Cu_2O. Hence the system, doped with n-type impurities, easily will further generate non compensated acceptor states, resulting p-type doped.

3.4.c - Doping effects on the optical band gap

Band gap modifications in Cu_2O, induced by impurities doping, can be attributed to two factors:

1. Dopants with large ionic radius, when accommodated in the oxide lattice, induce structural distortions, disrupting copper-copper internetwork interactions around the dopant site. Since the high lying valence band and the low lying conduction band positions depend on the intensity of such internetwork interactions [11], their doping induced disruption leads to band

gap widening. The ionic radius of a dopant impurity is determined by its oxidation state and coordination number in the compound.

2. The dopant electronic states can hybridize with the valence or conduction band or can even form defect states in the band gap [11]. Each of these phenomena can lower or rise the bands edges.

Still Nolan and Elliott [11] theoretically calculated the cation-doped Cu_2O band gap shift taking into account the two factors above (see Tab. 3.3).

Dopant Cation	ΔE_g (eV)
Sn^{+2}	*0.11*
Zn^{+2}	*-0.03*
Mg^{+2}	*0.04*
Ca^{+2}	*0.11*
Sr^{+2}	*0.13*
La^{+3}	*0.15*

Tab. 3.3 *Optical band gap shift (positive sign means widening, negative sign narrowing) induced by incorporation of various cation dopants (from Ref. [11]).*

Furthermore, it has been recently computed in detail the effects of nitrogen doping on the Cu_2O band gap by Li and co-workers [31]. They firstly realized that nitrogen incorporation, as substitutional for oxygen atoms, causes small structural distortion, yet, the electronic states of defects modify the band gap. In particular, they analyzed two possible cases:

1. Nitrogen substitutes oxygen (atomic concentration around 2%). A small shift of the VBM, towards higher energies, occurs because nitrogen *2p* states mix with the oxygen *2p* states, increasing the width of the valence band. The total band gap narrowing results 0.04 eV.
2. Nitrogen substitutes oxygen (atomic concentration around 2% - 3%) and induces the generation of a nearby oxygen vacancy. In addition to the nitrogen effects on the valence band edge, the oxygen vacancy introduces a state close to the CBM, rising the latter of 0.77 eV. The resulting band gap modification is a widening of 0.67 - 0.68 eV.

For each of these two N-doped structures the authors calculated the formation energies, respectively at copper-rich and oxygen-rich conditions, revealing that for the latter conditions the first structure is much more stable (and favored) than the second one.

The complex scenario depicted by these density functional theory (DFT) studies about nitrogen doping effects on the Cu_2O band gap is reflected by the outcomes of various experimental works. In fact, Ishizuka and co-workers [29], characterizing nitrogen doped Cu_2O sputtered films, together with hole density enhancement, did not observe any significant band gap modification. This result should be explained by the first case reported in Ref. [31]. On the other hand, Nakano and co-workers [32], again for nitrogen doped Cu_2O sputtered films, measured a widening (about 0.4 eV) of the band gap. According to the authors of Ref. [31], their result seems to reproduce the second case predicted by the DFT study, that is, the formation of oxygen vacancies along with nitrogen doping. Therefore it appears that both the cases, substitutional nitrogen and substitutional nitrogen together with oxygen vacancy, would be reproducible, changing the growth and doping conditions of sputtered films.

3.4.d - Doping effects on the copper oxidation state

Another study [33], on nitrogen doping of sputtered Cu_2O thin films, proved that impurities incorporation, during the films synthesis, can influence the stoichiometry of the oxide. In this study, the authors observed that nitrogen is responsible for the suppression of CuO phase, which has been recorded by X-ray diffractometry only in the undoped film.

The observation of the doping effects, reported by this study, in general, unfolds the tangible possibility of controlling the chemical state of copper atoms during the deposition of cuprous oxide, favoring such phase instead of cupric oxide. Hence, if the growth and doping conditions are synergistically arranged, one could prevent the formation of CuO domains that could strongly deteriorate charge carriers transportation.

3.4.e - Doping effects on the minority charge carriers lifetime

As anticipated at the beginning of this section, incorporation of impurities not only can modify the absorption coefficient, the charge carriers density and the copper atoms chemical state of the cuprous oxide, but can also influence the equilibrium of the point

defects. This possibility, recently, was theoretically investigated by Isseroff and Carter [16], which realized that cation dopants like Mg and Zn have a positive effect in favoring the generation of simple copper vacancies instead of split vacancies. In the latter defects, the relative hole is strongly localized around the defect site, thus the presence of split copper vacancies shortens the photo-generated electrons life time, that easily recombine with holes at such trap states.

Mg and Zn atoms, in spite of being ideally n-type dopants, augment the overall hole density in Cu_2O, since each atom, when substitutes one copper atom, easily generates two copper vacancies. The first vacancy compensates the introduced electron, whereas the second vacancy dopes the system p-type. The configuration that costs less energy to the system consists of the dopant occupying the nearby empty site left by the first vacancy, which in this way cannot be split, that is, any neighboring Cu atoms cannot move towards the site already occupied by the dopant (see Fig. 3.9). Furthermore, the second vacancy appears next to the relaxed dopant and is not split. Even though Isseroff and Carter found that all the configurations containing split vacancies have higher energy, the energy gain, by the system assuming the already described configuration with only simple vacancies clustered around the impurity, is less than 1 eV. Therefore, in principle, one should not expect a strong impact of Mg and Zn on the photo-generated electrons life time and in turn, on the photo-current.

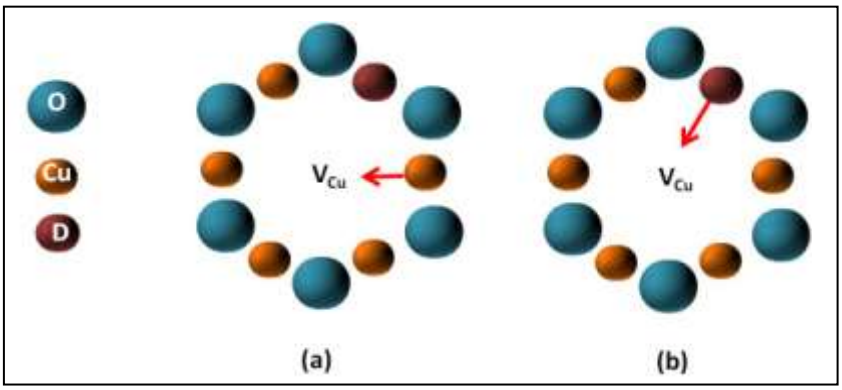

Fig. 3.9 *Nearest neighbors around a V_{Cu}. There are two possibilities for the atoms to relax: a) moving a Cu atom toward V_{Cu}, which becomes V^{s}_{Cu} or b) moving the dopant D toward V_{Cu} (taken from Ref. [16]).*

3.5 - Cu_2O thin films synthesized by RF sputtering

This section is dedicated to the synthesis of undoped Cu_2O films deposited by RF magnetron sputtering and the optimization of subsequent furnace annealing, in terms of temperature, oxygen flux and duration.

3.5.a - Synthesis

Thin films have been deposited by RF sputtering of a Cu_2O target (99.99 % purity) in a non-reactive atmosphere on Corning glass substrates (see Fig. 3.10). During the deposition the argon pressure was 5.0×10^{-3} mbar and the radiofrequency power was 200 W.

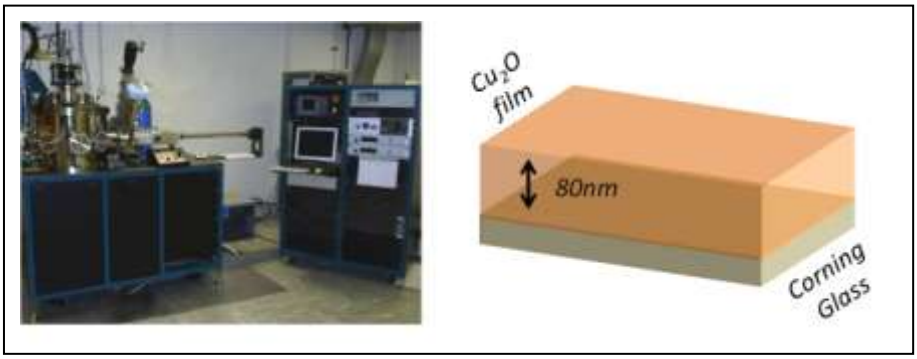

Fig. 3.10 *Photo (left) of the ultra-high-vacuum sputtering system used to deposit our samples. Schematic illustration (right) of the as-deposited samples.*

The substrate was kept at 100 °C during the deposition, since this thermal supply is compatible with a film synthesis on the majority of flexible polymeric substrates. This temperature also guarantees that the crystalline quality is much higher if compared to the sample deposited at room temperature. This fact was assured by x-ray diffraction analyses, performed with a Bruker-AXS D5005 diffractometer, by using Cu K_α radiation at 1.54 Å, with a grazing incidence angle of 1°.

Figure 3.11 reports the XRD spectra of two as deposited samples. Compared to the film deposited at room temperature, the sample sputtered with a substrate temperature of 100 °C shows much more intense Cu_2O peaks, respectively related to the families of planes (111) and (200), because it has a larger number of Cu_2O crystalline grains.

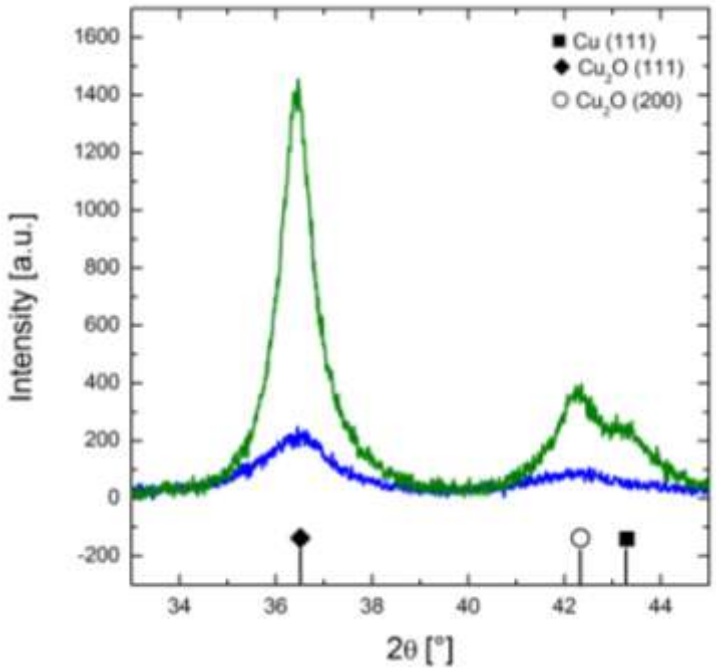

Fig. 3.11 *XRD spectra of the as deposited samples synthesized at room temperature (blue line) and at 100 °C (green line).The tabulated peaks are reported for Cu_2O (ref. code 00-005-0667) and Cu (ref. code 00-004-0836).*

To investigate the Cu:O ratio of the films composition, Rutherford backscattering spectrometry measurements (RBS 2.0 MeV He^+ beam, 165 ° backscattering angle) were performed on samples sputtered at the conditions already described on c-Si substrate. In Fig. 3.12 the RBS spectrum of the as deposited sample is reported. The signal at 1.03 MeV is related to He^+ backscattered from Si atoms of the substrate surface, while the signals at 0.74 and 1.55 MeV are associated to the ions backscattered respectively from O and Cu atoms of the film surface.

RBS spectra simulations, preformed by "SimNRA" software [34], revealed that the film thickness is 80 nm and the Cu:O ratio is about 2:1. Therefore, the sputtered samples preserved the stoichiometry of the Cu_2O target at the selected deposition conditions also without the insertion of reactive O_2.

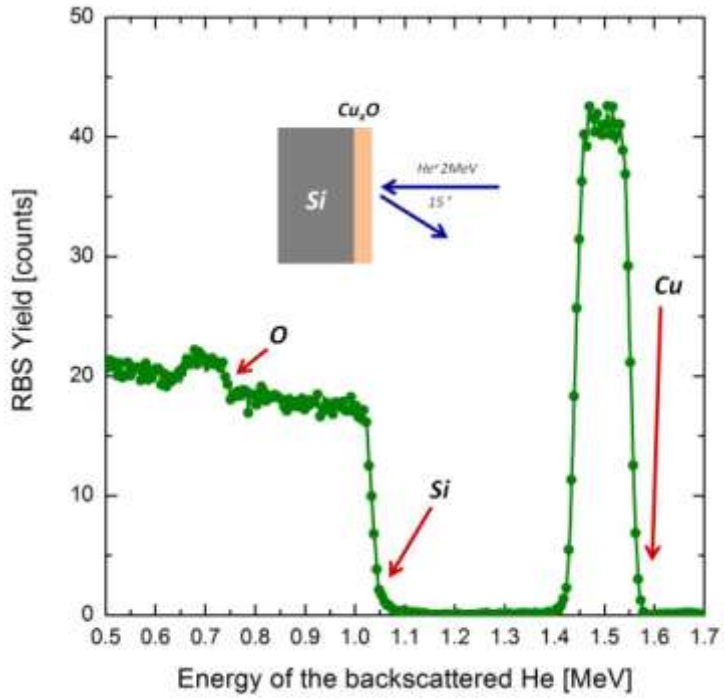

Fig. 3.12 *RBS performed on as deposited sample, sputtered on c-Si substrate*

The deposited films were successively annealed in a conventional furnace in O_2 ambient (constant flux of 2.5 litres per minute) in order to improve their optical, structural and electrical properties (see Fig. 3.13). The role of various annealing temperatures, 200°C, 250°C and 300°C, combined with two different treatment durations (1 h and 4 h) were taken into account.

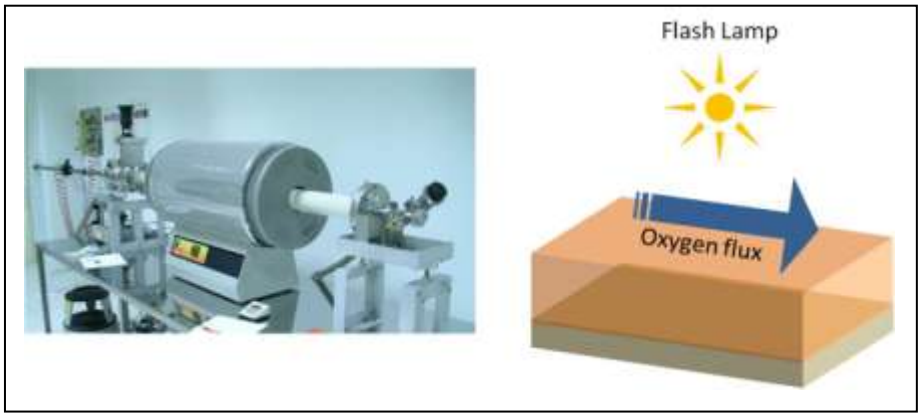

Fig. 3.13 *Photo (left) of the horizontal furnace used to anneal our samples. Schematic illustration (right) of the annealing process.*

3.5.b - Structural characterization

The XRD spectra of all the samples annealed for 1 h are reported in Fig. 3.14. In all the cases they are polycrystalline.

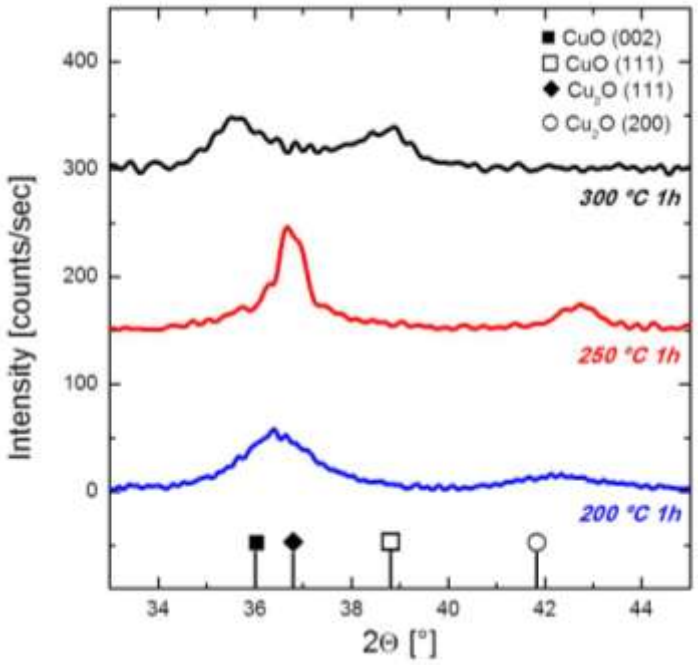

Fig. 3.14 *XRD spectra of the samples annealed for 1 h at 200 °C, 250 °C and 300 °C. The tabulated peaks are reported for Cu_2O (ref. code 00-005-0667) and CuO (ref. code 01-0800076).*

After the annealing for 1h at 200 °C, the XRD spectrum in Fig. 3.14 shows only diffraction peaks associable to the most intense peaks of the polycrystalline Cu_2O phase, which are relative to the families of planes (111) and (200). No preferential growth direction of the crystallites is present, since the relative intensities of the peaks have values close to those ones expected. The same (111) and (200) peaks of the Cu_2O phase are still the only ones detected in the diffraction pattern for the sample annealed at 250 °C for 1h (see Fig. 3.14). In this case both peaks are more intense by a factor of two and narrower. In particular, by using the Debye-Scherrer formula, an increase of grain size by a factor of three can be estimated. Moreover, a slight shift is evident of about 0.2° of 2θ toward higher angles in respect to the tabulated positions of Cu_2O, that can be associated to a strain accumulated in the film. These facts suggest that, due to the higher furnace temperature, the formation of a higher number of crystalline Cu_2O grains, having wider sizes, is favoured in respect to the 200 °C case (see panels (a) and (b) in Fig. 3.15). Therefore we can deduce that, after one hour, the

lower 200 °C annealing temperature is not sufficient for a complete crystallization of all the film volume.

By further increase the annealing temperature at 300°C for 1h, the peaks relative to the Cu_2O phase disappear and the only detectable XRD signals are relative to the (111) and (002) peaks of the monoclinic CuO phase (see Fig. 3.14). Hence this temperature, for the oxygen flow set in this case, is so high that the Cu_2O polycrystalline phase is not anymore stable and, reacting with the oxygen in the furnace, is fully converted into CuO (see panel (c) in Fig. 3.15). Similar phase transition, in sputtered copper oxide thin films was observed, for furnace annealing in air, by Pierson and co-workers [35].

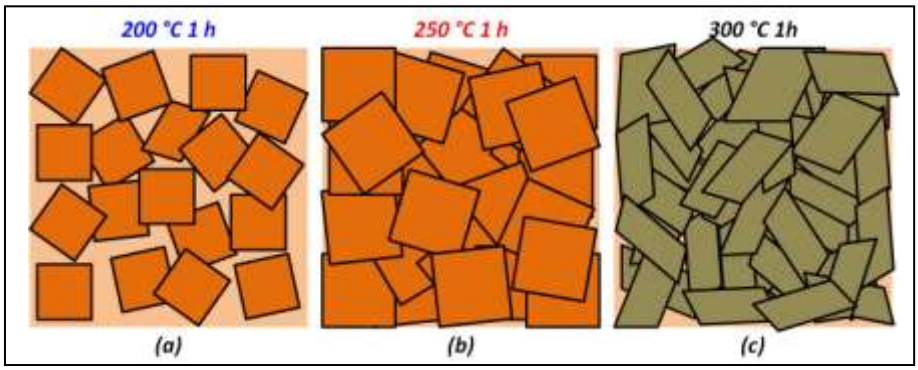

Fig. 3.15 *Schematic illustration of the polycrystalline structure of samples annealed for 1 h at 200 °C, 250 °C and 300 °C. The orange squares represent the Cu_2O grains, the grey monoclinic polygons are the CuO grains, while the background is the amorphous matrix.*

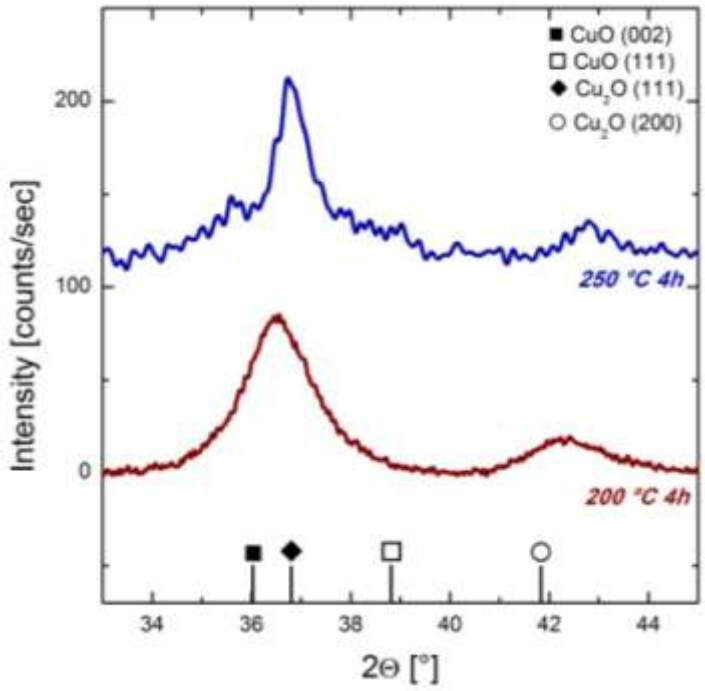

Fig. 3.16 *XRD spectra of the samples annealed for 4 h at 200 °C and 250 °C. The tabulated peaks are reported for Cu_2O (ref. code 00-005-0667) and CuO (ref. code 01-0800076).*

The XRD spectra of all the samples annealed for 4 h are instead reported in Fig. 3.16. As regards the sample treated for 4 h at 200 °C, the XRD pattern still shows the same (111) and (200) Cu_2O peaks having unchanged width but doubled intensities if compared to the pattern of the sample annealed at the same temperature but for 1 h. Thus the longer annealing allows the formation of a larger population of Cu_2O grains with comparable dimensions (compare both panels (a) in Fig. 3.15 and in Fig. 3.17). Therefore, in order to obtain a complete crystallization of the Cu_2O film at 200 °C, an annealing duration of 4 h is necessary. The upper spectrum in Fig. 3.16, relative to sample annealed at 250 °C for 4 h, appears as the superposition of the (002) and (111) CuO peaks to the Cu_2O diffraction pattern. The Cu_2O peaks have the same shape and intensity observed for 1 h long treatment at 250 °C. These results suggest that even though the oxidant annealing at 250°C produces a high number of large polycrystalline grains of Cu_2O, this temperature is sufficient to trigger also the oxidation into CuO (see panel (b) in Fig. 3.17). Since the conversion of Cu_2O into CuO results from the progressive diffusion of oxygen into the films [35], CuO crystalline grains, still not present in the sample annealed at 250 °C for 1 h, are formed and visible after 4 h long treatment at the same temperature. Therefore we can conclude that 4 h long oxidizing treatment in all the considered temperature range is necessary to reach the complete

crystallization of the film. Nevertheless, to preserve the Cu_2O phase without the formation of CuO, the temperature of 200 °C must be used.

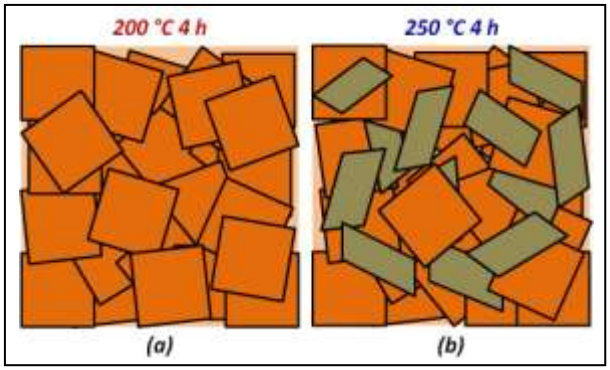

Fig. 3.17 *Schematic illustration of the polycrystalline structure of samples annealed for 4 h at 200 °C and 250 °C. The orange squares represent the Cu_2O grains, while the grey monoclinic polygons are the CuO grains.*

3.5.c - Optical characterization

The optical direct transmittance *T(λ)* and specular reflectance *R(λ)* were measured, in order to evaluate the optical absorption coefficient α, by using a VARIAN Cary 500 double beam UV-Vis- NIR spectrophotometer in the wavelength range from 200 nm to 2000 nm. Direct transmittance spectra were normalized to 100% baseline obtained by mounting the empty sample holder, while for the absolute reflectance spectra a calibrated standard sample was used as reference. The optical absorption coefficient α was calculated according to the approximated expression [36]:

$$T = (1 - R)e^{-\alpha \cdot d} \tag{3.3}$$

In Fig. 3.18, as an example, it is reported the absorption coefficient versus *hv* ranging between 1.7 and 3.5 eV, for the sample annealed at 200 °C for 1 h.

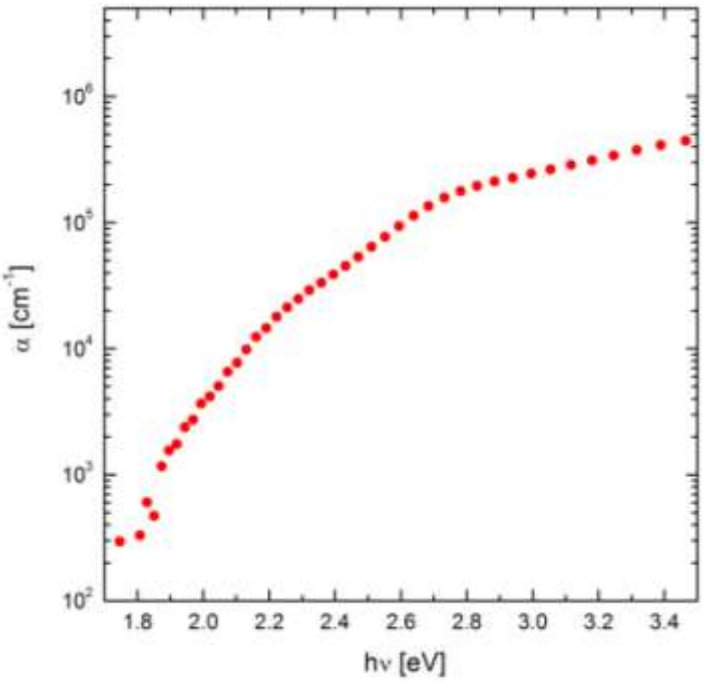

Fig. 3.18 *Absorption coefficient of the sample annealed at 200 °C for 1 h.*

In order to estimate optical absorption edges in amorphous or polycrystalline films the $(\alpha \cdot h\nu)^{1/n}$ versus $(h\nu)$ curves (Tauc plots) are generally plotted, where $h\nu$ is the incident photons energy and n is a properly chosen integer [37]. The optical band gap of the samples can be extrapolated from the $h\nu$ axis intercept of the line fitted on the linear portion of the Tauc plots. In a Tauc plot, the exponent denominator n can assume different values, depending on the nature of the band - band optical transition. For direct allowed transitions, n is 1/2, whereas, for direct forbidden transitions n is 3/2. Finally, for indirect allowed transitions, n is 2. Each of these Tauc models, in order to be valid, have to be adopted for high absorption coefficient values ($\alpha > 10^4$).

The lowest band gap of single crystalline Cu_2O is, in principle, direct not allowed, yet the successive gap is direct allowed. As stated in section 3.2, for single crystalline bulk Cu_2O, the optical transition relative to the second band gap is much stronger and the first band gap is, on the contrary, weakly visible ($\alpha < 10^4$). Moreover, if the Cu_2O film is thin and polycrystalline, the bands edges can be blurred and the optical transitions rules, valid for single crystalline bulk Cu_2O, break down. For these reasons, in literature it is commonly employed the $(\alpha \cdot h\nu)^2$ vs $(h\nu)$ plot for sputtered and chemically grown Cu_2O thin films [24], [25], [27].

Figure 3.19 reports the Tauc plots of the samples annealed for 1 h at 200 and 250 °C. Since, in these samples, the single Cu_2O polycrystalline phase was preserved, as proved by the XRD analysis, their optical band gaps were calculated fitting the linear part of the curve $(\alpha \cdot h\nu)^2$ vs $(h\nu)$. The optical band gap energies, E_g, are evaluated as 2.44 (±0.02) eV and 2.52 (±0.02) eV, respectively at 200 °C and 250 °C. These values are consistent with those ones reported in literature for sputtered Cu_2O films [24] [35]. Moreover, the increase of about 3% recorded in the value of E_g at 250°C means that this higher annealing temperature for 1h is more effective in producing a Cu_2O phase free from sub-gap optical defects [25]. Whereas, for the highest used temperature, 300 °C, the same $(\alpha \cdot h\nu)^2$ vs $(h\nu)$ plot does not present a linear region. It confirms the negligible presence of Cu_2O phase, as suggested by XRD analysis, that revealed only CuO phase, which owns an indirect band gap. The Tauc plot $(\alpha \cdot h\nu)^{1/2}$ versus $(h\nu)$ is reported in Fig. 3.20. The value n = 2 for indirect transition was chosen, because only in this case the data show a linear relationship up to energies $h\nu$ = 3.2 eV. It gives an optical gap equal to 1.30 (±0.02) eV, that is compatible with other studies [35], [38].

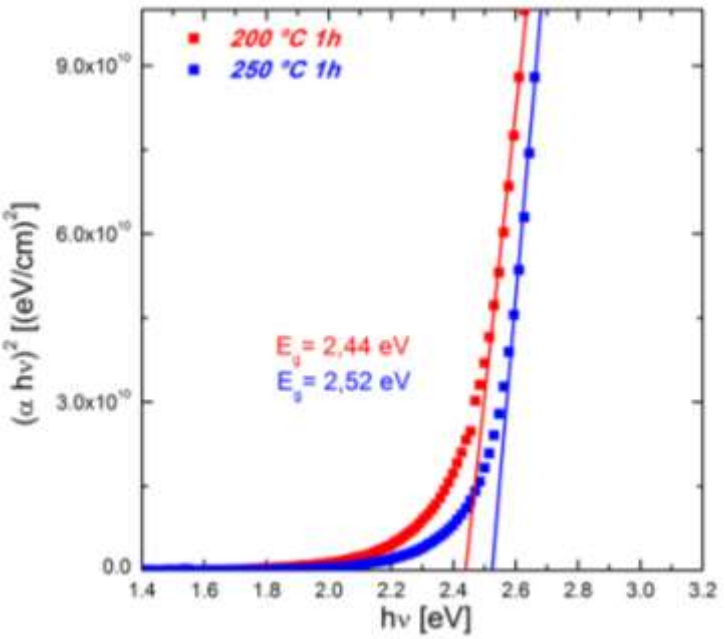

Fig. 3.19 *Plots of $(\alpha \cdot h\nu)^2$ as a function of hν (dotted curves) and the lines fitted on the linear portion of the Tauc plots for the samples annealed for 1 h at 200 °C and 250 °C.*

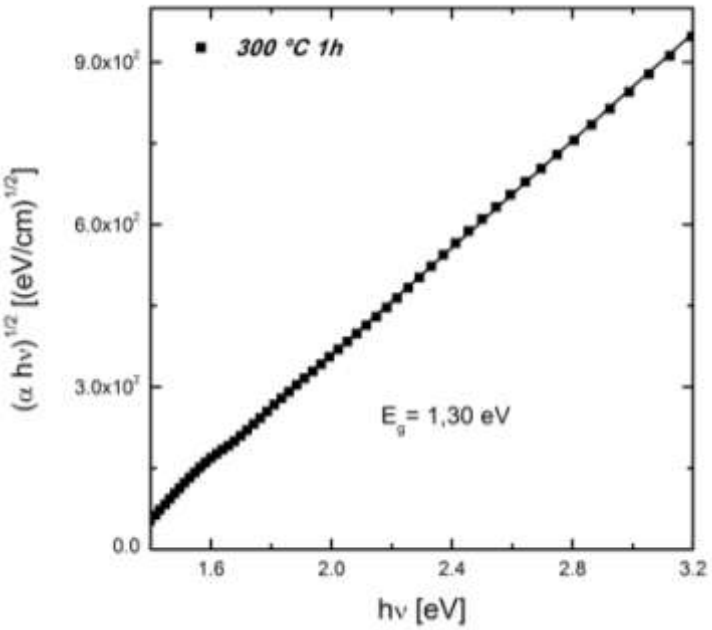

Fig. 3.20 *Plot of $(\alpha \cdot h\nu)^{1/2}$ as a function of hν (dotted curve) and the line fitted on the linear portion of the Tauc plot for the sample annealed for 1 h at 300 °C.*

Figures 3.21 and 3.22 show the Tauc plots of the samples annealed for 4 h. Owing to the fact that only at 200°C the Cu_2O single phase is preserved, (see Fig. 3.21), from the plot $(\alpha \cdot h\nu)^2$ vs $(h\nu)$ a direct band gap energy E_g = 2.49 (±0.02) eV was extrapolated.

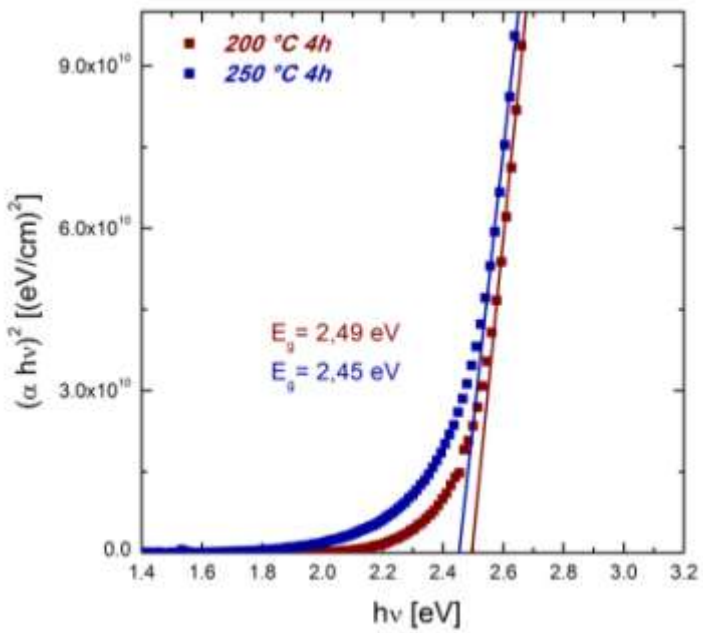

Fig. 3.21 *Plots of $(\alpha \cdot h\nu)^2$ as a function of hν (dotted curves) and the lines fitted on the linear portion of the Tauc plots for the samples annealed for 4 h at 200 °C and 250 °C.*

This value is, within the experimental errors, equal to the gap of the film treated at 250° for 1 h, that is the optimized value for our samples. Whereas, for the sample annealed at 250 °C for 4 h, the Tauc plots with n = 1/2 gives a direct gap value of 2.45 (±0.02) eV, compatible again with the typical values of Cu_2O band gap energy [24] [35]. However, for this sample, because of the co-presence of the two Cu_2O and CuO phases, (see the XRD pattern in Fig. 3.16), also the Tauc plot with n = 2 has been plotted, as reported in Fig. 3.22. In this case a linear fit, extended in the lower energy region between 1.4 eV and 3.2 eV, can be done, and it was obtained again the CuO indirect gap value of 1.30 (±0.02) eV. Also in this case, the presence of oxides crystalline phases identified by XRD measurements are confirmed.

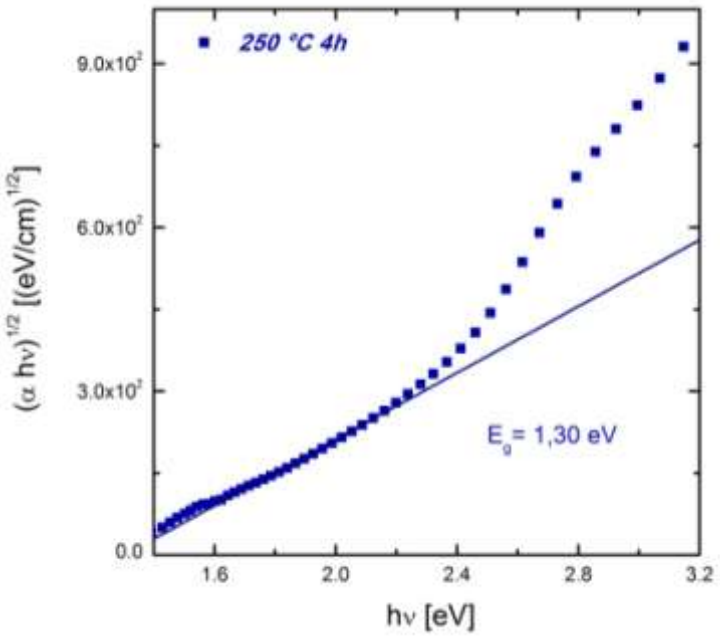

Fig. 3.22 *Plot of $(\alpha \cdot h\nu)^{1/2}$ as a function of hν (dotted curve) and the line fitted on the linear portion of the Tauc plot for the sample annealed for 4 h at 250 °C.*

Therefore, we can conclude that both the crystalline structure, analysed by XRD, and the optical parameters, investigated through the Tauc plots, confirm that the Cu_2O polycrystalline phase can be preserved for 1 h long treatment up to 250 °C, but 4 h long annealing guarantees a more complete crystallization at the annealing temperature of 200 °C.

Tab. 3.4 summarizes the structural and the optical properties of all the annealed samples.

Sample	Phase	Optical Band Gap (eV)
200 °C 1 h	Cu_2O	2.44
250 °C 1 h	Cu_2O	2.52
300 °C 1 h	CuO	1.30
200 °C 4 h	Cu_2O	2.49
250 °C 4 h	Cu_2O/CuO	2.45/1.30

Tab. 3.4 *List of the annealed samples with the relative detected crystalline phases and the measured optical band gap.*

3.5.d - Electrical characterization

The electrical properties of all the annealed samples, containing exclusively cuprous oxide were studied by the sheet resistance measurements, performed with a Keithley 4200-SCS (Semiconductor Characterization System) at room temperature by using the 4-point collinear probe technique. The estimated resistivity of the sample annealed for 1 h at 200° C is equal to 400 Ω·cm, at 250° C for 1 h and at 200° C for 4 h the values are one order of magnitude lower, respectively 20 Ω·cm and 64 Ω·cm (see Tab. 3.5). These results suggest that the improvements in the Cu_2O crystalline quality, observed at higher temperature or longer annealing time, determine a better conductivity, due to the increase of the number or of the size of the Cu_2O crystallites (hence with less grain boundaries) [39] and also owing to the removal of other lattice defects. Here is also why the resistivity of the film annealed at 250°C for 1h is a factor of three lower than the value recorded at 200°C 4h. All these quantities are coherent with the best results reported in literature [24].

Sample	Resistivity (Ω·cm)
200 °C 1 h	400
250 °C 1 h	20
200 °C 4 h	64

Tab. 3.5 *Resistivity of the samples annealed for 1 h at 200 °C and 250 °C and for 4 h at 200 °C.*

Therefore, the study of the influence of temperature and duration of annealing on the structural, optical and electrical properties allowed to understand the optimal post-deposition treatment conditions needed to obtain good conductivity performances.

3.6 - Nitrogen doping of sputtered Cu_2O thin films

In this section the experimental activity concerning nitrogen doping of cuprous oxide sputtered films is presented. Nitrogen has been chosen as dopant since it is non-toxic, abundant and, as discussed in section 3.4, its incorporation mainly leads to a significant increase of the holes density, offering the possibility to synthesize a high conductive material for oxide-based solar cells. The methodology we have employed to insert nitrogen atoms in the oxide deeply differs from the in-situ techniques, such as reactive sputtering typically reported in literature [29], [32] [33]. Indeed, by ion implantation followed by furnace annealing in oxygen rich atmosphere, in respect to the other approach the following aims are achieved:

1. to make the impurity atoms to arrange in the oxide lattice in such a way that they generate shallow acceptor states in the band gap;
2. to hinder some side effects of doping, such as the formation of oxygen vacancies;
3. to recover the structural defects caused by energetic nitrogen atoms beam, during the implantation.

Compared to the doping methodologies where nitrogen atoms are inserted during the oxide deposition, the technique here reported owns the following peculiar features:

- out-of-equilibrium incorporation of the impurity dopants in the Cu_2O layer;
- more accurate control of nitrogen atomic concentration in the films, because ion implantation allows to fix the atomic concentration simply setting the implanted ionic dose. In this way it was possible to investigate a wide range of doping concentrations, without being capped by any film growth-related condition.

Deposited films were nitrogen doped by ion implantation with a 400 kV HVEE ion implanter (see Fig. 3.22). The ion energy was set at 46 keV, because, according to SRIM [40] simulations (see Fig. 3.23), the implanted nitrogen density distributions result inside the film thickness. In particular the implantation projected range is equal to 38 nm with a straggling of 25 nm. Then the distribution profile, as shown in Fig. 3.23, is a Gaussian-like curve centred at the middle of the film thickness with a *FWHM* of 50 nm. The implanted doses were $0.45 \cdot 10^{16}$ N/cm^2, $0.91 \cdot 10^{16}$ N/cm^2 and $1.89 \cdot 10^{16}$ N/cm^2. I will refer to these samples with an average concentration, obtained by considering the nitrogen density distribution mediated on the thickness and the estimated volume atomic density. The corresponding approximated average atomic concentrations are, respectively, 0.6 N %, 1.2 N % and 2.5 N % (see Tab. 3.6).

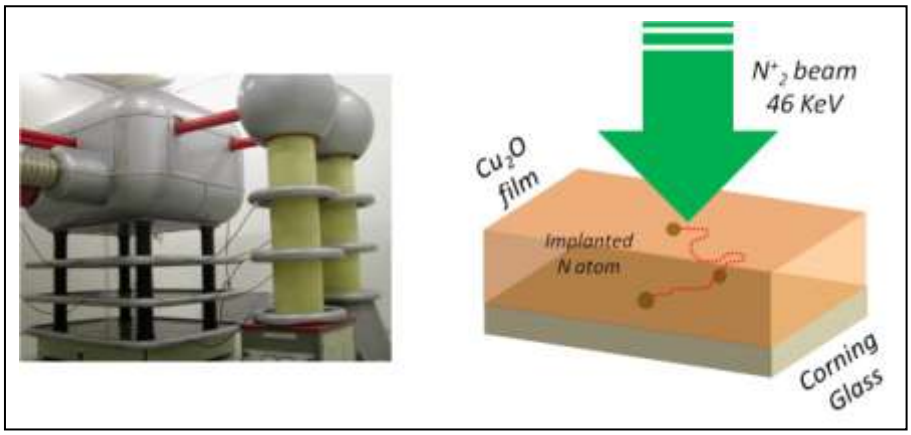

Fig. 3.22 *Photo (left) of the Cockroft-Walton multipler voltage generator of the ion implanter used to insert nitrogen atoms in our samples. Schematic illustration (right) of the implantation process.*

After the implantation all the samples were treated at the same annealing condition, 200 °C 4h, that was demonstrated to optimize the quality of the undoped sputtered Cu_2O. This thermal treatment is also long enough to recover the implantation induced structural defects and to achieve the electrical activation of the nitrogen atoms inside the Cu_2O lattice.

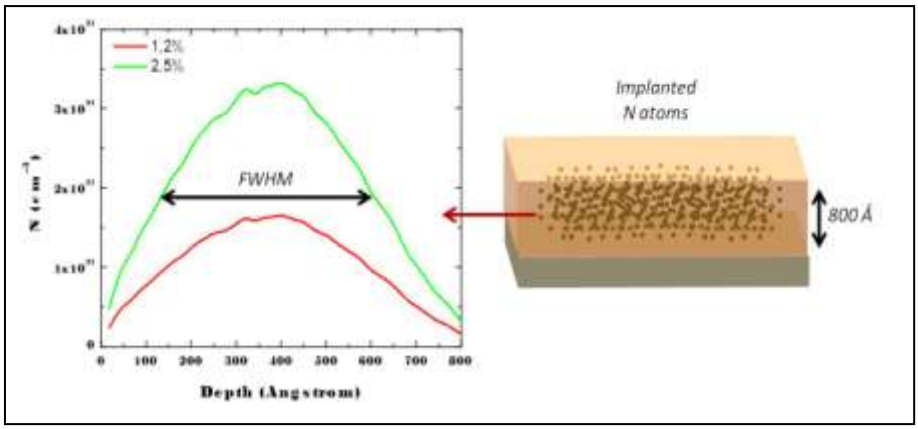

Fig. 3.23 *Nitrogen atoms density distributions, for two concentrations (2.5% and 1.2%) along the film thickness (right) as calculated by SRIM [39] simulations.*

Dose (N/cm^2)	Atomic Concentration (%)
$0.45 \cdot 10^{16}$	0.6
$0.91 \cdot 10^{16}$	1.2
$1.89 \cdot 10^{16}$	2.5

Tab. 3.6 *List of the implanted doses of nitrogen atoms, with the corresponding list of atomic concentrations.*

3.6.a - Structural characterization

In order to analyse the structural properties, Fig. 3.24 compares the XRD patterns of all the nitrogen doped and undoped films after annealing. No diffraction peak related to the Cu_3N phase was found for nitrogen doped samples in all the investigated 2θ range between 20° and 60°.

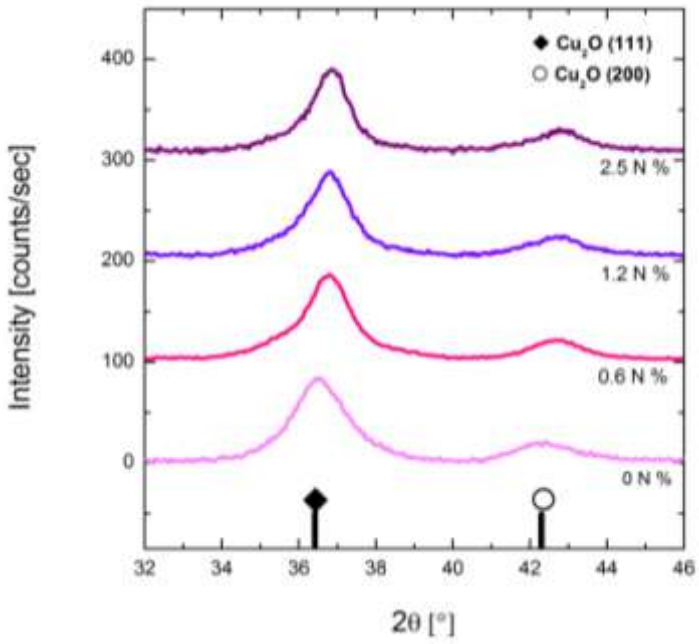

Fig. 3.24 *XRD spectra of the undoped and doped samples, annealed for 4 h at 200 °C. The tabulated peaks are reported for Cu_2O (ref. code 00-005-0667).*

Independently by the nitrogen content, between 0 N % and 2.5 N %, the XRD spectra are the same with only the (111) and (200) peaks relative to the Cu_2O phase. But while in all the cases these peaks have the same intensities and widths, their positions are shifted of about 0.3° to higher 2θ angles for all the implanted samples in respect to the undoped one. This fact indicates that after the ion implantation and subsequent annealing the Cu_2O crystalline quality is preserved, while only a little strain is induced.

3.6.b - Optical characterization

By the optical measurements, the $(\alpha \cdot h\nu)^2$ vs $(h\nu)$ plots of the annealed Cu_2O:N films were also analysed. Tauc plots corresponding to two nitrogen contents are reported as examples together with the undoped case in Fig. 3.25. Direct energy gaps, E_g, were estimated by linear fits of the Tauc curves and reported as a function of nitrogen content in Fig. 3.26. Independently of N concentration, the doped samples exhibit a value of E_g equal to 2.43 (±0.02) eV, that is 0.06 eV lower than that one measured for the annealed undoped sample.

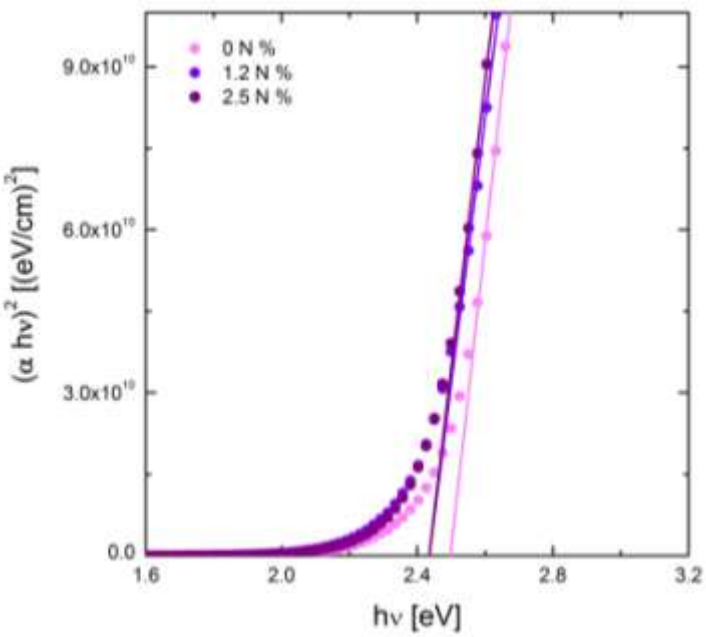

Fig. 3.25 *Plots of $(\alpha \cdot h\nu)^2$ as a function of hν (dotted curves) and the lines fitted on the linear portion of the Tauc plots for the undoped film and for the samples doped with 1.2% and 2.5% of nitrogen atomic concentration.*

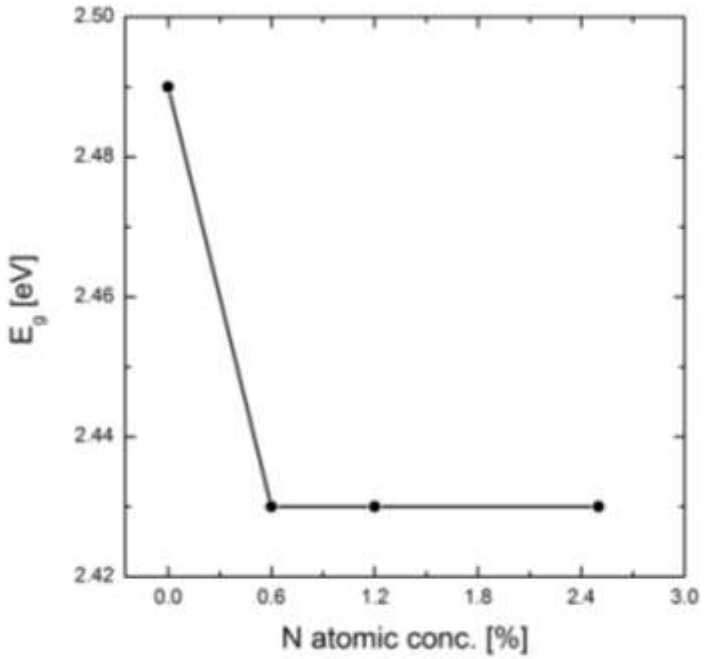

Fig. 3.26 *Optical band gap of doped samples as a function of the nitrogen atomic concentration.*

The observed decrease in the E_g value results comparable to that one calculated by Li and co-workers [31] for the model of N atoms substituting some O atoms in the Cu_2O lattice without generation of oxygen vacancies (0.04 eV). The same DFT study expects that, when N doping leads to the formation of V_O, the E_g widening can be provided. However, this second situation can be excluded due to the furnace annealing performed in oxygen rich atmosphere. In fact, as discussed in section 3.4, at oxygen-rich conditions, the structure consisting only of nitrogen substituting oxygen has a formation energy 1.85 eV smaller than the energy relative to the structure with V_O.

3.6.c - Electrical characterization

Regarding electrical properties, the resistivity measured for doped and successively annealed samples containing 0.6 N%, 1.2 N% and 2.5 N% are respectively 42 Ω·cm, 12 Ω·cm and 7 Ω·cm. These values are lower than that one measured for the annealed undoped film, 62 Ω·cm (see Tab. 3.7). In order to understand if implantation induced defects in the crystalline structure that can influence the resistivity values, we measured the resistivity of a film that was firstly annealed and then implanted. Its resistivity worsened if compared to the undoped annealed sample. This latter result

reveals that N interstitial atoms and the possible defects created by the N ions bombardment are counter-productive for the improvement of conductivity.

Atomic Concentration (%)	Resistivity (Ω·cm)
0	64
0.6	42
1.2	12
2.5	7

Tab. 3.7 *Resistivity of the undoped film and samples doped with 0.6%, 1.2% and 2.5% of nitrogen atomic concentration..*

Whereas, the decreasing trend of the resistivity of the doped samples, annealed after the implantation, proves that the used thermal treatment not only recovers deleterious defects caused by implantation but also makes a fraction of inserted N to migrate from interstitial positions to oxygen Cu_2O lattice sites, as already deduced by optical measurements. Indeed, it is well accepted that substitutional N doping of Cu_2O increases the free charge carriers density by introducing shallow acceptor states in the band gap [29].

Some estimations can be done considering the data reported in literature for sputtered Cu_2O and Cu_2O:N thin films. In particular in ref. [24] for a Cu_2O single phase thin film having a resistivity value of about 1 Ω·cm, the authors report a mobility of 0.3 $cm^2V^{-1}s^{-1}$ and a hole density of about $7 \cdot 10^{18}$ cm^{-3}. If we suppose that the mobility of our undoped optimized sample is of the same order of magnitude, and being our measured resistivity 62 Ω·cm, it can be assumed that the hole density is of the order of 10^{17} cm^{-3}.

As regards the doped samples, we demonstrated that the introduction of the higher nitrogen content determines a decrease of the resistivity, up to a factor 10. It was associated to the increase of the hole density, thanks to the substitutional arrangement of nitrogen atoms. Thus we can argue that the hole density increases of about a factor 10 since, as confirmed in literature (see for example [17]), no significant change in mobility values is expected.

Considering the results obtained from optical and electrical measurements, we can declare that the N doping performed with the method here described consists of the following steps (see Fig. 3.27):

1. the impinging N^+_2 molecule, breaks into two N atoms, each having half of the parent molecule energy;
2. the N atoms are incorporated at the interstitial sites;
3. furnace annealing in oxidant atmosphere causes the substitution of some O atoms with N atoms, avoiding V_O generation.

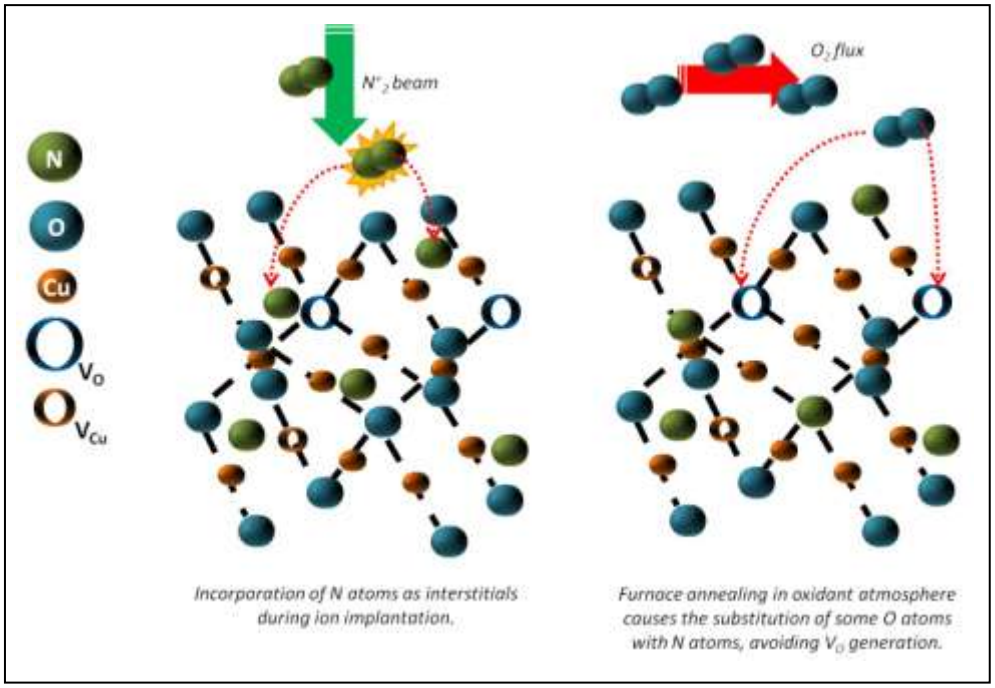

Fig. 3.27 *Schematic illustration of the processes occurred during the ion implantation and the subsequent furnace annealing in oxidant atmosphere.*

3.6.d - Conclusions

In this work, we firstly achieved the optimization of the crystalline, optical and electrical quality of the sputtered films, by the control of temperature and duration of post-deposition annealing treatment. Due to the high reactivity of Cu_2O with oxygen, only a strict range of operations (during the synthesis or after the deposition) guarantees the optimal crystalline quality and conductivity performance.

The results concerning doped samples clearly indicate that the N incorporation through ion implantation, followed by thermal annealing, in the Cu_2O films has a relevant effect in controlling the electrical properties without large modification of the optical band gap. The decrease of resistivity (up to one order of magnitude) coherently with the increase of the N doping concentration has been explained by annealing-driven substitution of oxygen atoms with implanted N atoms.

Since optical band gap widening, theoretically predicted for V_O density increase [31], has not been observed, the generation of V_O, induced by N incorporation, has been here excluded. In particular, we claim that the high concentration of V_O, expected for specific N doping conditions, was avoided, in our samples, due to the thermal treatment carried out in oxidant atmosphere.

Finally, it is worth to say that the small values of the resistivity, reached for the N doped samples, represent an essential step toward the formation of low-resistivity contacts on Cu_2O films for efficient photovoltaic applications.

3.7 - Cu_2O thin films synthesized by spray pyrolysis

This section deals with the optimization of undoped samples synthesis, carried out through a systematic study of the spray pyrolysis deposition conditions. Eventually, the fine-tuning of the deposition parameters has led to the growth of high quality Cu_2O layers on glass and kapton (polyimide) foil, whose chemical name is "*4,4'-oxydiphenylene-pyromellitimide*". This achievement is important considering the facts that glass is the most common substrate for commercial solar cells and kapton foils are widely used in flexible printed devices, thus it offers a practical possibility to employ cuprous oxide for pliable solar cells or for flexible transparent electronics (in particular for p-type channel thin film transistor).

3.7.a - Synthesis

Cuprous oxide undoped films were synthesized by spray pyrolysis using a *SonoTek-ExactaCoat* system with an ultra-sonic spray nozzle, firstly on Corning glass substrates (see Fig. 3.28).

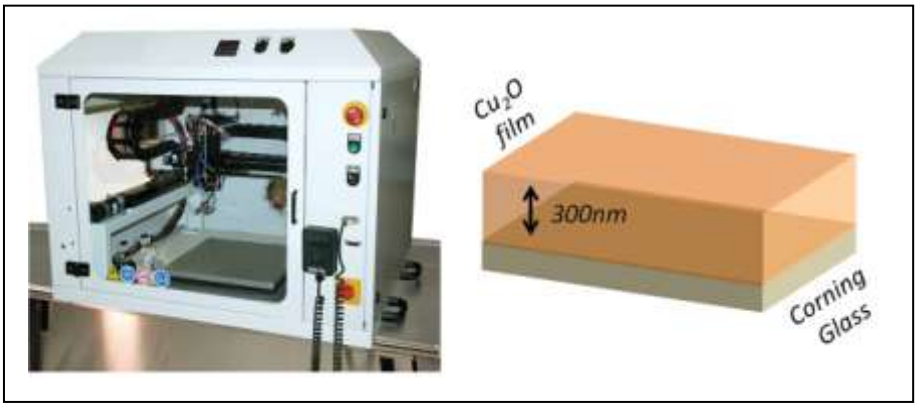

Fig. 3.28 *Photo (left) of the ultra-sonic spray system, by SonoTek, used to deposit our samples. Schematic illustration (right) of the as-deposited samples.*

In order to uniformly deposit the thin films on the glass area (2.5 x 2.5 cm^2), at each cycle, the spraying nozzle is moved along a raster, covering all the substrate surface (see Fig. 3.29).

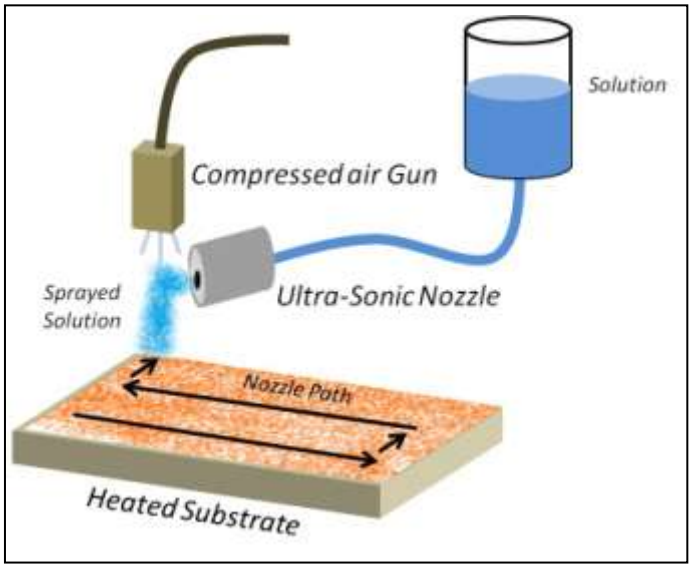

Fig. 3.29 *Spray pyrolysis deposition cycle on an extended substrate area.*

The deposition cycle was repeated until the thickness (measured by *Dektak* profilometer) reached the aimed value of about 300 nm.

Since the pyrolysis reactions take a definite time and the carrier gas blow cools down the surface, a certain dead time t_d has to elapse from the end of a cycle to the beginning of the next, in order avoid quenching and alteration of good formation of the film.

The fulfilment of good Cu_2O synthesis strongly depends also on the size of the droplets impacting the substrate surface. If too big droplets splash on the substrate, its surface will be excessively cooled and the solvent evaporation would lead to rough or even not adherent film [41].

Therefore, to achieve high quality films, the sprayed droplets have to be small enough. Typical ultra-sonic generators, as that mounted of the *SonoTek* system, produce droplets with narrow size distribution, whose mean diameter *D* is given by [42]:

$$D = A \cdot \left({}^{8\pi \cdot \gamma}\!\Big/_{\rho \cdot f^2} \right)^{1/3} \tag{3.4}$$

where *γ* is the droplet surface tension, *ρ* is the solution density and *f* is the ultra-sonic frequency.

Little diameters (units of microns) were obtained, not only thanks to the high generator frequency, but also decreasing the surface tension *γ*, adding to the solution a certain percentage of isopropil alcohol (IPA).

The precursor solution was prepared mixing in deionised water:

- copper acetate, $Cu(CH_3COO)_2$;
- D - (+) glucose, $C_6H_{12}O_6$;
- 2-propanol (IPA).

All these chemical components where provided by *Sigma Aldrich* with a purity higher than 99%.

According to Kosugi and Kaneko [27] the Cu_xO film synthesis, using this solution, could be separated into five steps (see Fig. 3.29):

1. The droplet arrives at the substrate and the heat, immediately, triggers the reduction of Cu^{+2} ions into metallic copper atoms Cu^0, by means of glucose, which, once oxidized, is vented together with the solvent.
2. The metallic copper atoms clusterize.
3. Each cluster oxidizes into Cu_2O, reacting with the oxygen.
4. Each Cu_2O cluster is further oxidized into CuO.
5. The Cu_xO clusters grow and become denser.

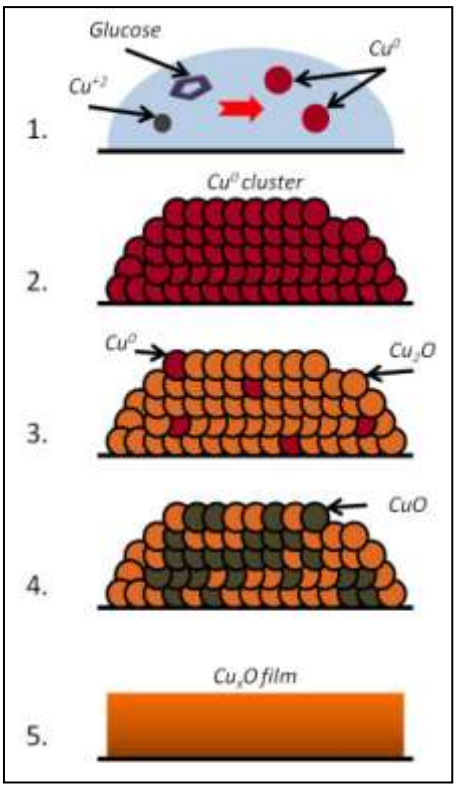

Fig. 3.29 *Scheme of the Cu_xO film formation process.*

Such film growth model is quantitatively described by the following system of equations [27]:

$$\begin{cases} [Cu] = e^{(-k_1 t_r)} \\ [Cu_2O] = {k_1}/{(k_2 - k_1)} \cdot \left[e^{(-k_1 t_r)} - e^{(-k_2 t_r)}\right] \\ [CuO] = \left[1 - {1}/{(k_2 - k_1)}\right] \cdot \left[k_2 \cdot e^{(-k_1 t_r)} - k_1 \cdot e^{(-k_2 t_r)}\right] \end{cases} \tag{3.5}$$

where the quantities in square brackets are the respective mole fractions of copper, cuprous and cupric oxides and t_r is the overall reaction time (proportional to the inverse of the copper acetate concentration). Finally, k_1 and k_2 are the reaction rate constants, dependent on the substrate temperature T_s.

Hence, according to the model by Kosugi and Kaneko [27], the Cu_2O mole fraction is a precise function of the substrate temperature, copper acetate, glucose and IPA concentration in the solution.

In our case, the depositions were carried out in air fixing the solution feed rate at 1 ml/min and the nozzle speed at 70 mm/s in order to minimize the substrate cooling during the solution spray. On the contrary, the substrate temperature T_s, the compounds concentration in the precursor solution and the dead time t_d, between two deposition cycles, were systematically modified in order to find out the best combinations, in terms of Cu_2O purity and quality. A detailed prospectus of the parameters kept constant or progressively changed in this work is reported in Tab. 3.8.

Deposition Parameters	
Solution Feed Rate	***1 ml/min***
Nozzle Speed	***70 mm/s***
Substrate Temperature	*250 → 275 °C*
Dead Time	*15 → 60 s*
Solution Parameters	
Copper Acetate	*0.02 → 0.04 M*
Glucose	***0.02 M***
2-propanol	***20%***

Tab. 3.8 *List of the deposition and solution parameters. The parameters that were not changed throughout all the work are written in bold character.*

Furthermore, some Cu_2O thin films were deposited on a flexible Kapton foil. In this case, the solution feed rate was lowered down to 0.5 ml/min, in order to again avoid excessive cooling of the substrate during the solution spray. In fact, it was observed that Kapton is more sensible, compared to Corning glass, to the cooling effect of the deposited solution.

3.7.b - Structural and morphologic characterization

The crystalline structure of all the samples was investigated by a *PANalytical X'pert Pro* diffractometer, in Bragg-Brentano configuration, using Cu K_α radiation in the 2θ range of 20° - 90°.

In order to investigate the effect of the substrate temperature on the film phase and crystalline quality, the first set of samples was deposited at fixed values of copper acetate concentration (0.02 M), IPA volume percentage (20%) and dead time t_d. The substrate temperature T_s was instead varied between 250 and 275 °C.

The XRD patterns of this ensemble of films are shown in Fig. 3.30 and clearly reveal that only at 250 °C the polycrystalline film is made up of Cu_2O single phase.

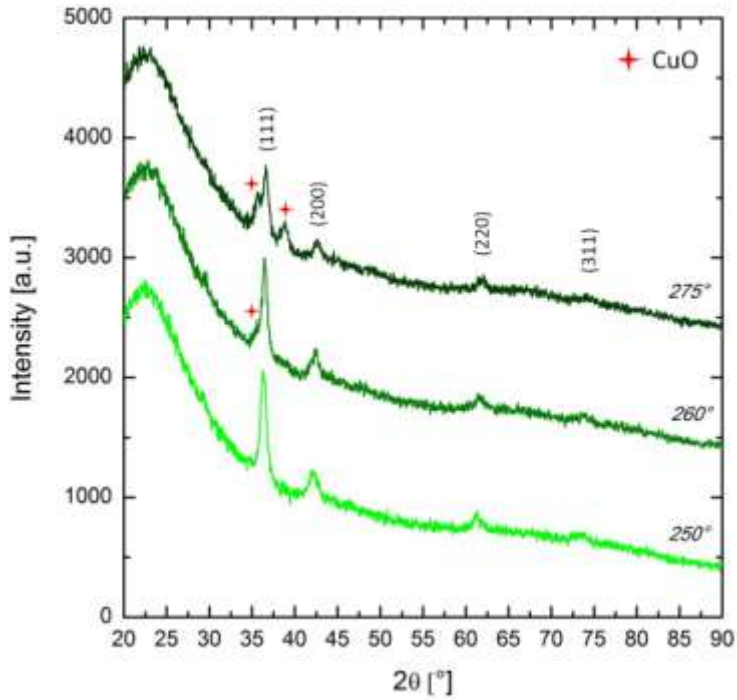

Fig. 3.30 *XRD spectra of films deposited at various substrate temperatures. Solution conditions were: copper acetate, 0.02 M; glucose, 0.02 M; and 2-propanol, 20% vol. Cu_2O peaks (ref. code 00-005-0667) are labeled with relative Miller indices.*

At higher temperatures, the polycrystalline CuO fraction increases at the expense of Cu_2O content, according to the growth model proposed by Kosugi and Kaneko [27] (see Fig. 3.31).

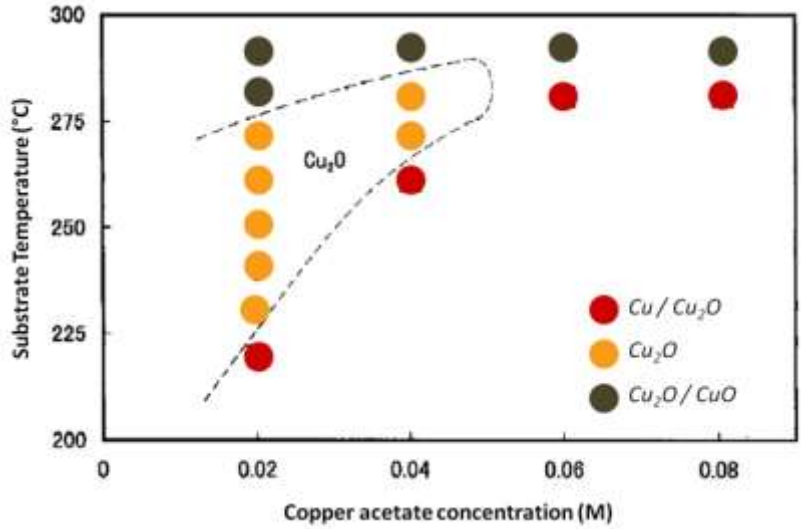

Fig. 3.31 *Phase relations in the copper-oxygen system under various copper acetate concentrations and substrate temperatures (taken from [27]). The dashed line designates the phase boundary inside which the Cu_2O molar fraction is, according to Eq. (3.5), higher than 95%.*

Then, fixing the copper acetate concentration at 0.02 M, the IPA volume fraction at 20% and T_s at 250 °C, we studied the influence of t_d. It was observed that the best crystalline quality of Cu_2O is obtained for t_d = 30 s. On the other hand, for higher t_d values, CuO phase appears; while, for shorter times, in spite of Cu_2O being the unique detected phase, the grains mean size is smaller. Indeed, in Fig. 3.32, the Cu_2O (111) peak, of the sample deposited at shorter t_d, appears to be wider.

These results revealed that the proper conditions to deposit a high quality Cu_2O film, from a solution containing 0.02 M of copper acetate and 20% of IPA, are T_s = 250 °C and t_d = 30 s. We will call this sample ***U1***.

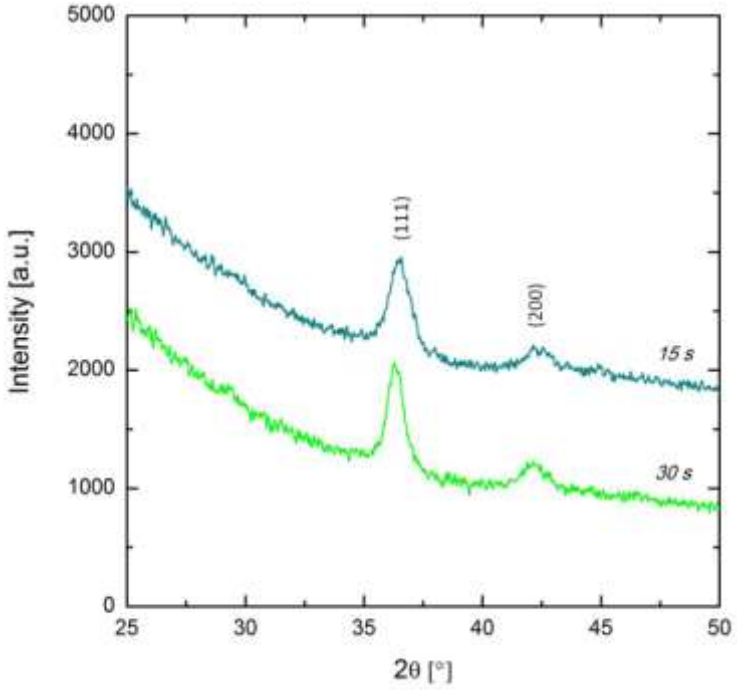

Fig. 3.32 *XRD spectra of films deposited at 250 °C and at various dead time values. Solution conditions were: copper acetate, 0.02 M; glucose, 0.02 M; and 2-propanol, 20% vol. Cu_2O peaks (ref. code 00-005-0667) are labeled with relative Miller indices.*

Subsequently, further deposition optimization attempts were done for a precursor solution with 0.04 M of copper acetate and 20% of IPA. In this case, single phase Cu_2O film (see Fig. 3.33), with the best qualities, were synthesized setting T_s = 275 °C and t_d = 30 s (sample ***U2***). Therefore, as reported by Kosugi and Kaneko [27], it was verified that there are various combinations of acetate concentration and substrate temperature to deposit single phase Cu_2O.

Moreover, the phase relation in the copper-oxygen system, under the used combinations of copper acetate concentration and T_s, resembles the relation experimentally determined and theoretically calculated by the same authors [27]. Thus, the growth model defined by Eq. (3.5) can be used to describe the oxides synthesis performed by our set-up.

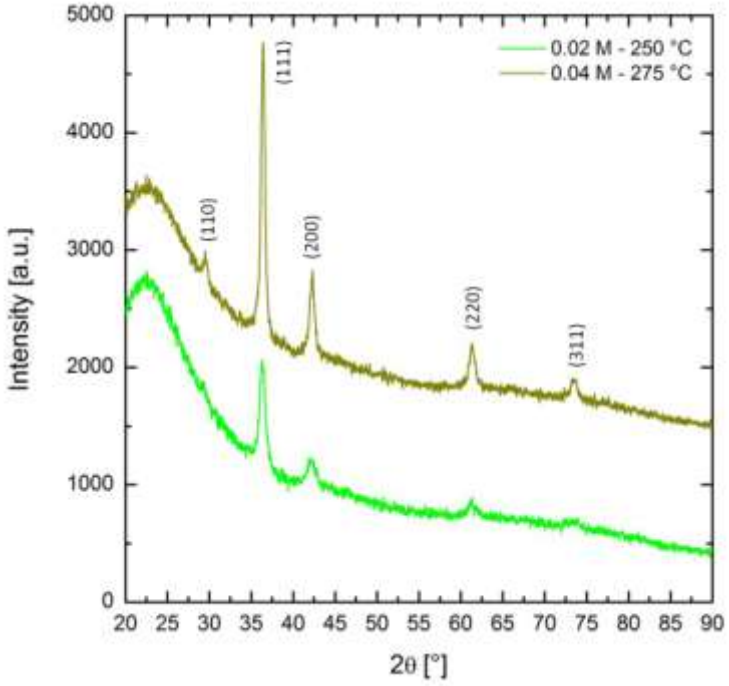

Fig. 3.33 *XRD spectra of films deposited at various substrate temperatures and different copper acetate molarity. Solution conditions were: glucose, 0.02 M; and 2-propanol, 20% vol. Cu_2O peaks (ref. code 00-005-0667) are labeled with relative Miller indices.*

However, the single phase Cu_2O films, ***U1*** and ***U2***, are not equivalent in terms of crystalline quality. Indeed, as can be noticed in Fig. 3.33, the cuprous oxide peaks of sample ***U2*** are narrower (the higher intensity reflects only a difference in thickness). In fact, using the Debye-Scherrer formula, it resulted that sample ***U2*** has grains with average size equal to 15 nm; thus they are bigger than sample ***U1*** grains, whose average size is 10 nm. This fact can be easily justified taking into account that the synthesis of sample ***U2*** was performed at higher temperature, thus the oxide received a higher thermal energy to form wider crystallites.

In order to check the contingent presence of non crystalline compounds in our samples IR analyses, in the attenuated total reflectance configuration, were performed by a Nicolet 6700 FTIR system.

FT-IR spectra of all the deposited samples (not shown) report no traces of precursor salts, indicating that the by-products decomposition and elimination processes were complete.

Finally, the morphology of all the films was investigated by scanning electron microscopy. The system used was an *AURIGA Cross Beam* workstations (Carl Zeiss). SEM images (see Fig. 3.34-a) show that all the deposited films uniformly cover the substrate surface, with a roughness of about 20 nm. Moreover, cross section images reveal that the films are dense without voids and cracks (see Fig. 3.34-b).

Single phase polycrystalline Cu_2O film (see the XRD pattern in Fig. 3.48) was deposited also on Kapton foil at T_s = 250 °C and t_d = 30 s, from a solution with 0.02 M of copper acetate and 20% of IPA. Also for this deposition, the film resulted uniform (see the plan view SEM image of Fig. 3.48) and compact, without cracks even with the bending of the substrate.

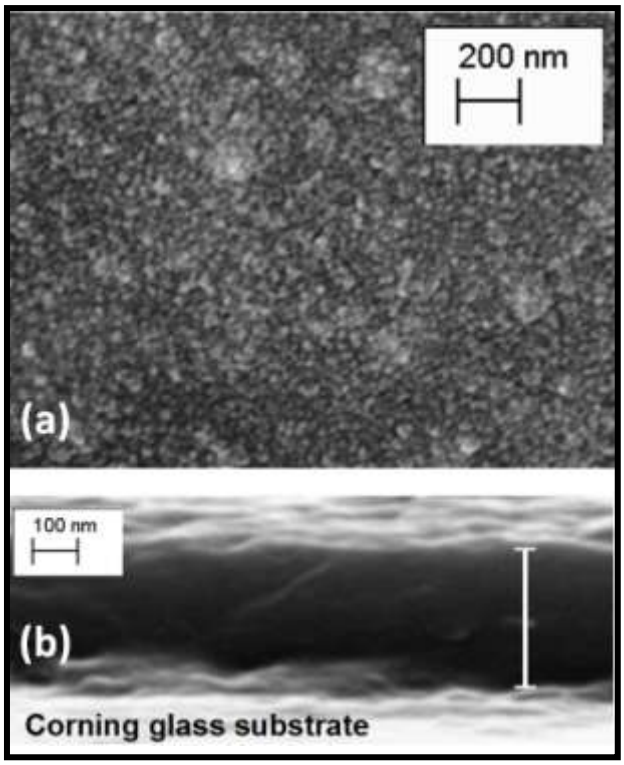

Fig. 3.34 *SEM micrographs of films deposited at 250 °C, (a) surface and (b) cross section. Solution conditions were: copper acetate, 0.02 M; glucose, 0.02 M; and 2-propanol, 20% vol.*

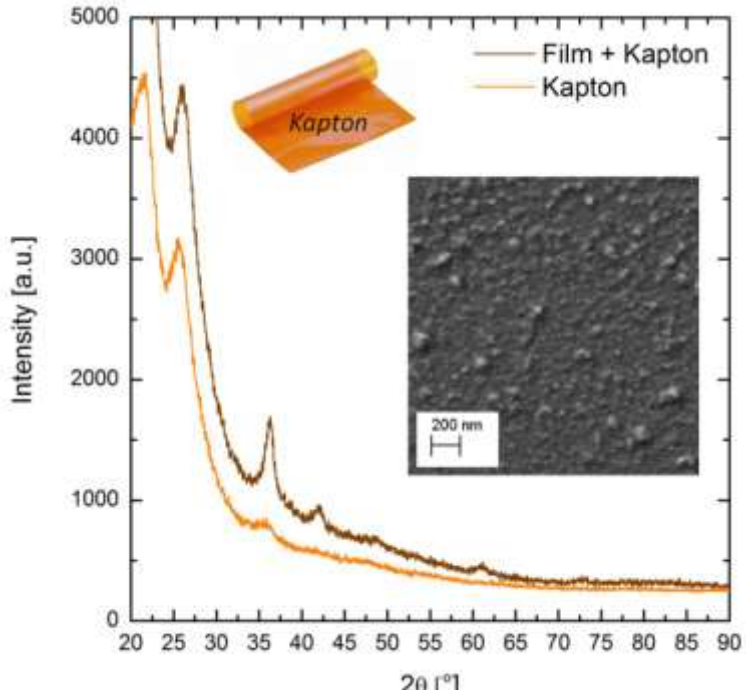

Fig. 3.35 *XRD spectra of films deposited on Kapton and of Kapton bare foil. Cu_2O peaks (ref. code 00-005-0667) are labeled with relative Miller indices. The inset shows the surface SEM micrograph.*

3.7.c - Optical and electrical characterization

UV-visible-NIR transmission and reflection spectra, for the determination of the absorption coefficient, were acquired in the wavelength range of 300 nm – 2000 nm by a Perkin Elmer – Lambda 950 spectrophotometer.

For the reasons discussed in section 3.5, concerning the Tauc plot, $(\alpha \cdot hv)^2$ vs (hv) curves were analysed to determine the optical band gap of single phase Cu_2O samples. Both ***U1*** (see Fig. 3.35) and ***U2*** have direct band gap equal to 2.58 eV. This value is coherent with the band gap reported in literature [27].

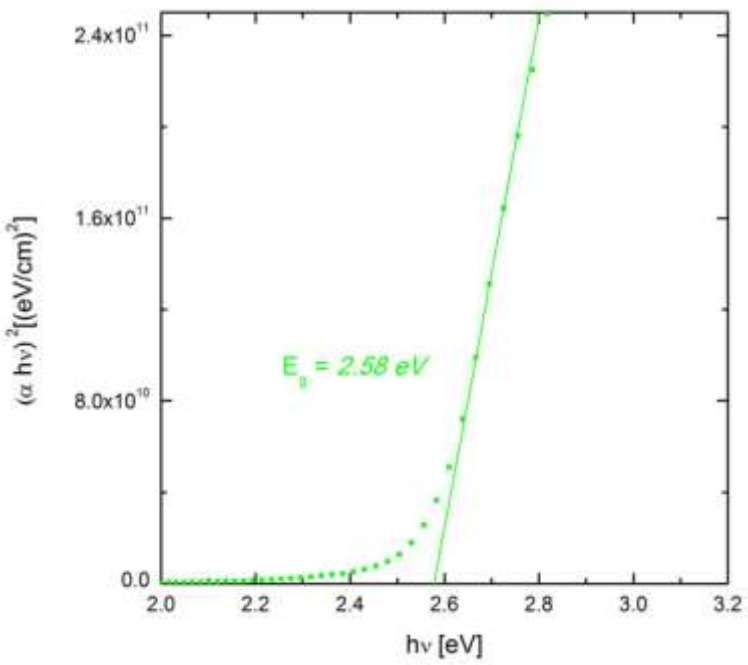

Fig. 3.35 *Plot of $(\alpha \cdot h\nu)^2$ as a function of hv (dotted curve) and the line fitted on the linear portion of the Tauc plots for sample **U1**.*

The resistivity of the same films was then measured according to the four – points probe method. Sample ***U1*** has a resistivity of 172 Ω·cm, while sample ***U2*** has the lower value of 126 Ω·cm, owing to the fact of having bigger grains (15 vs 10 nm), hence less grain boundaries. The Hall mobility was measured, using a *Bio-Rad HL 5500* Hall system, for single phase Cu_2O films deposited in a preliminary work at very similar conditions as for sample ***U1***. It was observed a Hall mobility of about 5 $cm^2/V \cdot s$ and it can be argued that such value can closely describe the mobility of sample ***U1***, having been deposited at similar conditions. Whereas, for the Cu_2O film deposited on Kapton it was measured a resistivity of 180 Ω·cm and a Hall mobility of 1.6 $cm^2/V \cdot s$, that is of the same order of magnitude of the typical mobility of amorphous silicon employed in commercial thin film transistors [43].

The temperature dependence of the conductivity, in the range of 250 K – 400 K, was analysed using a CS8900 Bio – Rad cryostat. For both samples ***U1*** (see Fig. 3.36) and ***U2***, it resulted that the conductivity follows the Arrhenius law:

$$\sigma = \sigma_0 \cdot e^{\left(-E_a/K \cdot T\right)} \tag{3.6}$$

with an activation energy E_a of 0.23 eV. This value, which falls into the range determined by O'Keeffe (compare with Fig. 3.6), indicates the acceptor state

(generated by V_{Cu}) position respect the VBM [1]. The activation energy, measured for our samples, is compatible also with the referred values for Cu_2O thin films deposited by sputtering and chemical methods [27].

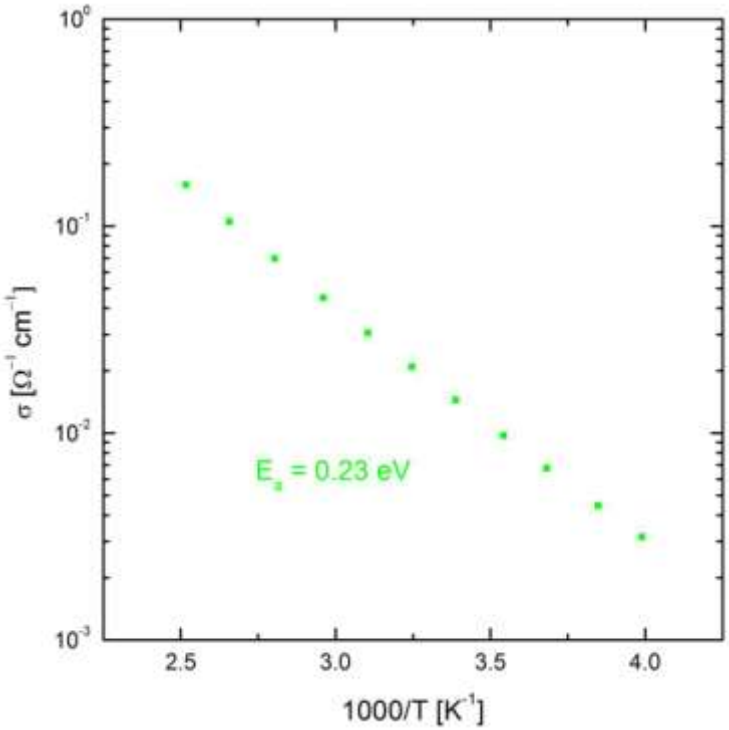

Fig. 3.36 *Relationship between the conductivity of sample U1 and reciprocal substrate temperature.*

3.8 - Mg, Zn and Ca doping of Cu_2O thin films synthesized by spray pyrolysis

This section concerns about cation doping of Cu_2O films sprayed on glass. The utilized dopants (zinc, magnesium and calcium) were inserted during the synthesis of the samples. These elements were chosen because, as deeply discussed in section 3.4, they are theoretically responsible for the oxide dark and photo conductivity enhancement.

3.8.a - Synthesis and structural characterization

As a first step, some cuprous oxide films, deposited by spray pyrolysis, were doped with Zn or Mg, adding to the precursor solutions, used for samples ***U1*** and ***U2***, respectively zinc acetate, $Zn(CH_3COO)_2$ and magnesium acetate, $Mg(CH_3COO)_2$. These salts were added at different molarities in order to investigate the effects of dopants concentration (dopant/Cu from 0% up to 10%) on the physical properties of the films.

The first set of Zn and Mg doped samples consists of films deposited from a solution containing 0.04 M of copper acetate, 0.02 M of glucose and 20 % of IPA (like for sample ***U2***, which is the reference film for the entire set). The deposition temperature was set at 275 °C and the dopants concentration was varied between 0% and 3%.

The XRD patterns of all the doped samples of this set show that, irrespective of the dopant element, crystalline grains of metallic copper appear along with Cu_2O phase. The formation of metallic copper phase occurs even at small Zn or Mg concentration (see Fig. 3.37) and indicates that the kinetic of film synthesis is modified by the presence of these dopants. Looking at the expression for metallic copper molar fraction in the film, in Eq. (3.5), it can be stated that both dopants induce a reduction of the rate constant k_1 regulating the oxidation of metallic copper into cuprous oxide during film synthesis.

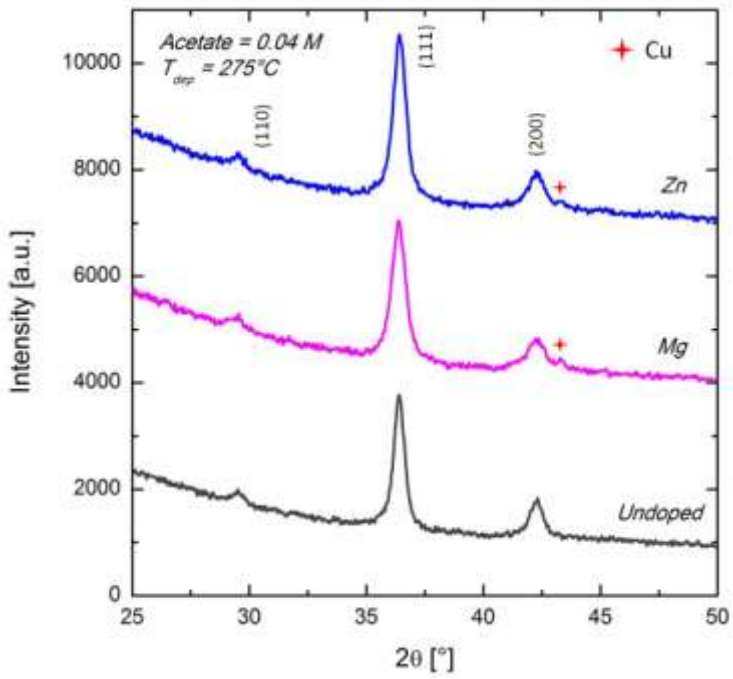

Fig. 3.37 *XRD spectra of undoped (**U2**), Zn (Zn/Cu = 0.4%) and Mg (Mg/Cu = 0.4%) doped films deposited at 275 °C. Solution conditions were: copper acetate, 0.04 M; glucose, 0.02 M; and 2-propanol, 20% vol. Cu_2O peaks (ref. code 00-005-0667) are labeled with relative Miller indices.*

In order to verify if Mg and Zn have similar effects on the rate constant k_2, for the oxidation of cuprous oxide into CuO (see Eq. (3.5)), it was deposited a second set of Zn and Mg doped samples, preparing a solution containing, in this case, 0.02 M of copper acetate and setting the deposition temperature again at 275 °C. Whereas, the dopants concentration was varied between 0% and 10%. For these conditions, the undoped film consists of a Cu_2O/CuO mixed phase. The XRD spectra of all these doped films, compared to the pattern of the reference undoped sample, show much less intense (or even absent in the case of Zinc doped film) peaks of CuO phase (see Fig. 3.38). On the contrary, the Cu_2O phase fraction in doped films resulted augmented. This result firmly demonstrates that when Zn or Mg are added to the precursor solution, the rate of Cu_2O oxidation into CuO, during the film formation, is diminished as well.

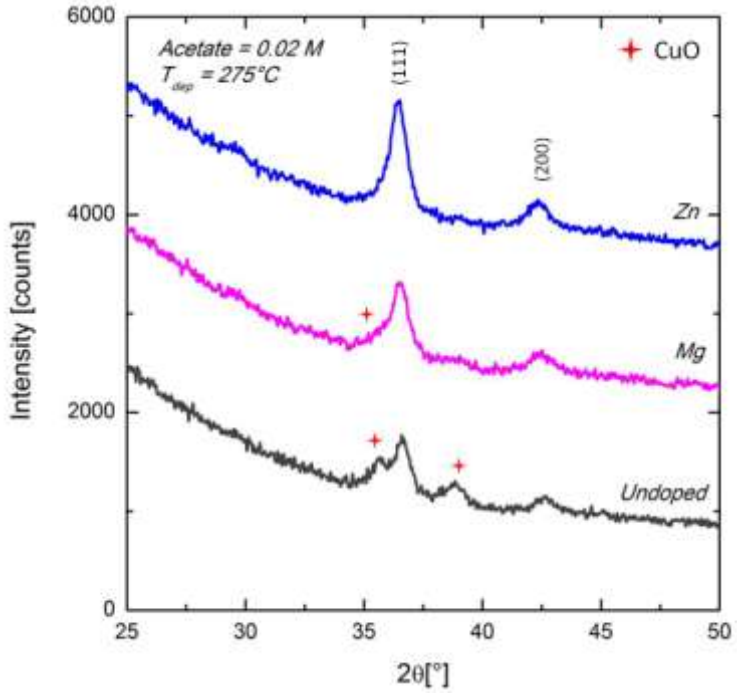

Fig. 3.38 *XRD spectra of undoped, Zn (Zn/Cu = 3%) and Mg (Mg/Cu = 3%) doped films deposited at 275 °C. Solution conditions were: copper acetate, 0.02 M; glucose, 0.02 M; and 2-propanol, 20% vol. Cu_2O peaks (ref. code 00-005-0667) are labeled with relative Miller indices.*

Since, with Zn or Mg doping, the reaction rate constants k_1 and k_2 decreased, the phase relations in the copper-oxygen system of the phase diagram reported by Kosugi and Kaneko for undoped films [27] (see Fig. 3.31) are modified.

In particular, adding Zn or Mg atoms, the phase boundaries, in the copper acetate concentration vs T_s diagrams, calculated by Eq. (3.5) and experimentally determined for undoped films by Kosugi and Kaneko [27], result translated at higher deposition temperatures (see Fig. 3.39).

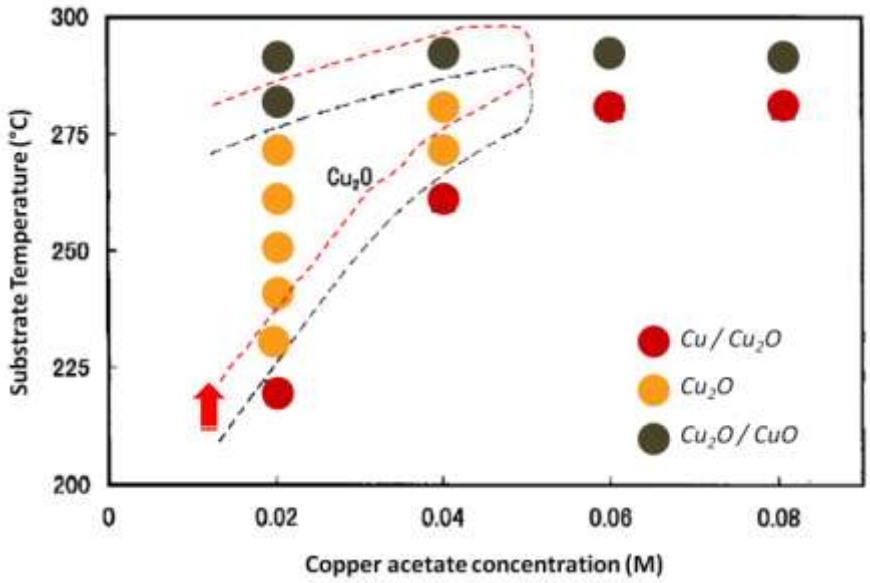

Fig. 3.39 *Phase relations (filled circles) in the copper-oxygen system under various copper acetate concentrations and substrate temperatures for undoped films (taken from [27]). The black dashed line designates the phase boundary, for undoped films, inside which the Cu_2O molar fraction is, according to Eq. (3.5), higher than 95%. The red dashed line, approximately represents the same phase boundary for Zn or Mg doped films, defined empirically in this study.*

To sum up, these Zn and Mg effects on the kinetic of copper oxide film synthesis, by spray pyrolysis, reveal that such elements influence the oxidation rate of Cu ions during the film formation. The possibility to control the fractions of Cu, Cu_2O and CuO phases in the film, not only setting the copper acetate molarity and the deposition temperature, but also fixing the dopants concentration, allows a fine tuning of the Cu_2O formation parameters (there is, in fact, a further degree of freedom for such tuning). In this way, Cu_2O films with high purity (specifically with negligible CuO contamination), for high performance solar cells, could be, in principle, more easily obtained. Moreover, since, with Zn or Mg doping, the phase boundaries of pure Cu_2O, in the phase diagram, are translated to higher deposition temperatures (see Fig. 3.39), it is possible, for a proper copper acetate concentration, to deposit single phase Cu_2O films with larger crystalline grains. Indeed, as it has been discussed comparing samples ***U1*** and ***U2***, higher deposition temperatures favour the formation of larger oxide grains.

Since it was observed that single Cu_2O phase is not preserved by doping the films prepared at the same conditions set for sample ***U2***, a third ensemble of Zn or Mg doped films was subsequently deposited at the conditions used for sample ***U1*** (i. e. a precursor solution containing 0.02 M of copper acetate and substrate temperature equal to 250 °C). The dopants concentration was varied between 0% and 10%.

The XRD spectra of Zn doped samples show that, for Zn/Cu < 1% (see Fig. 3.40), the phase is only Cu_2O (we label this group of samples ***Cu_2O:Zn***). On the other hand, for Zn/Cu ≥ 1%, crystalline grains of ZnO are formed together with Cu_2O. Since the ZnO detected peak is related to the family of planes (002) (reference code: 00-001-1136), it can be argued that ZnO grains, grew mainly along the ZnO cell c-axis. Therefore, we can imagine that the structure of such highly doped films is a dense network of interpenetrating Cu_2O grains and ZnO pillars.

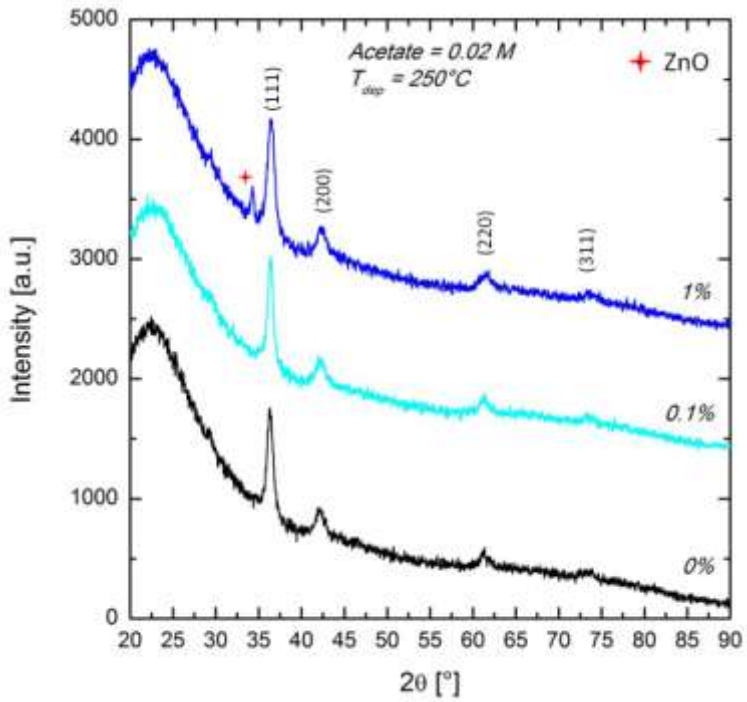

Fig. 3.40 *XRD spectra of Zn doped films deposited at 250 °C. Solution conditions were: copper acetate, 0.02 M; glucose, 0.02 M; and 2-propanol, 20% vol. Cu_2O peaks (ref. code 00-005-0667) are labeled with relative Miller indices.*

The XRD patterns of Mg doped samples revealed that the films consist of only Cu_2O phase for Mg/Cu < 10% (we label this group of samples ***Cu_2O:Mg***). In fact, for Mg/Cu ≥ 10%, the formation of the compound Cu_2MgO_3 (guaggenite) is clearly detected (see Fig. 3.41).

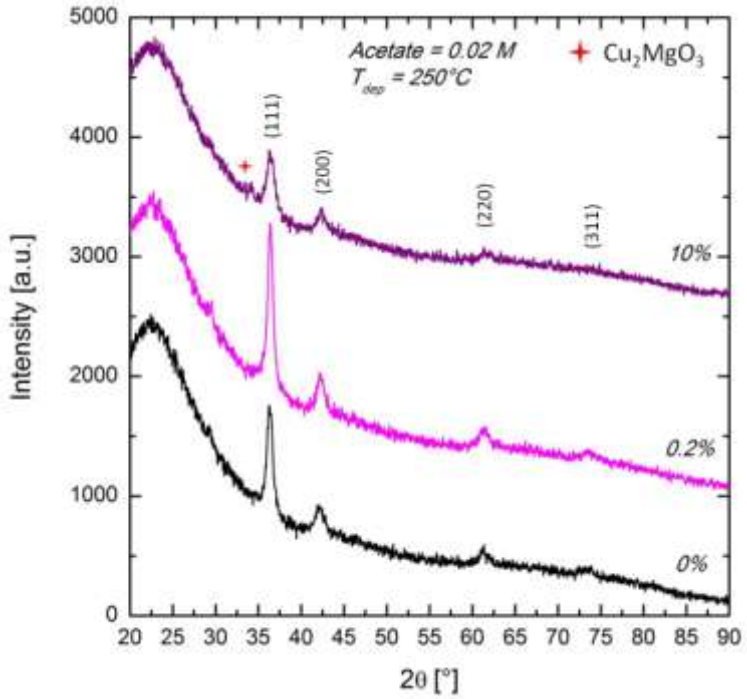

Fig. 3.41 *XRD spectra of Mg doped films deposited at 250 °C. Solution conditions were: copper acetate, 0.02 M; glucose, 0.02 M; and 2-propanol, 20% vol. Cu_2O peaks (ref. code 00-005-0667) are labeled with relative Miller indices.*

Since some Cu atoms were consumed to form Cu_2MgO_3, the appearance of its peak at 34.4 ° (reference code: 00-041-1364) is accompanied by the visible decrease of Cu_2O related peaks.

Along with the already described Zn and Mg doped samples, Ca doped films were deposited at the same conditions. Looking at their XRD spectra (Fig. 3.42 reports some examples) the same conclusions, as for Mg doped samples, can be stated.

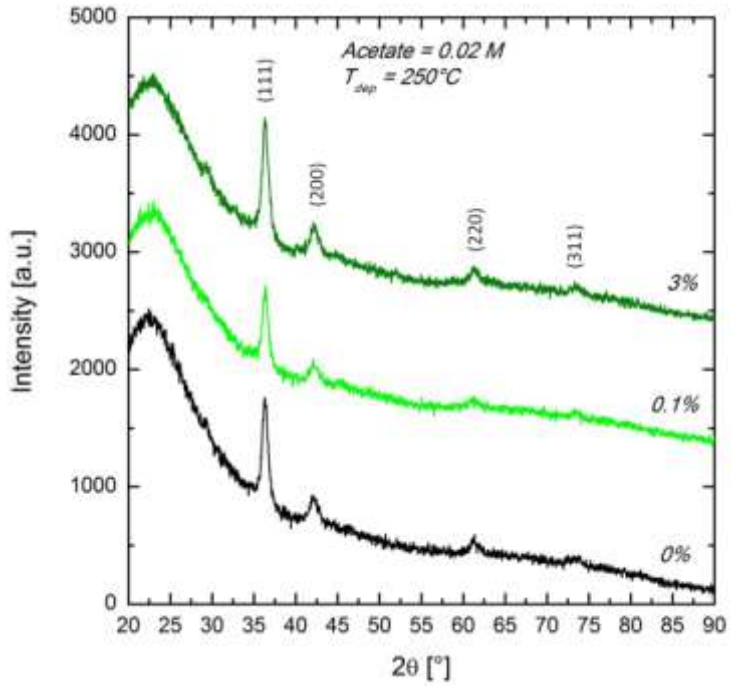

Fig. 3.42 *XRD spectra of Ca doped films deposited at 250 °C. Solution conditions were: copper acetate, 0.02 M; glucose, 0.02 M; and 2-propanol, 20% vol. Cu_2O peaks (ref. code 00-005-0667) are labeled with relative Miller indices.*

From the quantitative analysis of the XRD patterns of all the Cu_2O single phase samples (***Cu_2O:Zn***, ***Cu_2O:Mg*** and ***Cu_2O:Ca***), it was observed that the cubic cell edge length is 4.27 Å, that is the reference Cu_2O cell parameter. Therefore, the incorporation of Zn, Mg or Ca does not alters the Cu_2O cell structure.

For the doped films containing spurious phases, like ZnO or Cu_2MgO_3, the calculated cell parameter resulted, respectively, not reliable or smaller (about 4.24 Å). Moreover, the grain average size (calculated according to the Debye-Scherrer formula) of all the Cu_2O single phase samples falls into the range between 10 nm and 12 nm. Hence, Zn, Mg and Ca do not influence the Cu_2O grain nucleation and growth dynamic.

The presence of non-crystalline materials, such as pyrolysis by-products or dopant compounds was excluded thanks to FT-IR investigations. Furthermore, from SEM analyses, the ***Cu_2O:Zn***, ***Cu_2O:Mg*** and ***Cu_2O:Ca*** films morphology appeared with the same features observed for the reference undoped sample ***U1***.

3.8.b - Optical and electrical characterization

Plotting $(\alpha \cdot hv)^2$ vs (hv) curves for ***Cu_2O:Zn***, ***Cu_2O:Mg*** and ***Cu_2O:Ca*** samples, it was observed that all show a direct optical band gap randomly ranging from 2.55 to 2.58 eV (see Fig. 3.43). Since the band gap of the reference sample ***U1*** is 2.58 eV and the extension of this range is equal to the accuracy (±0.03 eV) of the band gap extrapolation method, it can be concluded that, in our case, Zn, Mg and Ca do not induce significant band gap modulation.

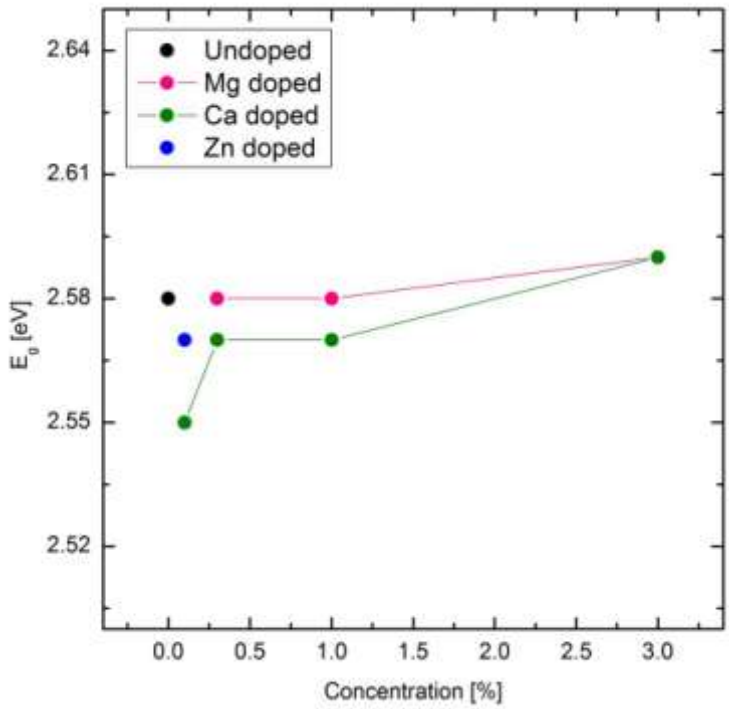

Fig. 3.43 *Optical band gap as a function of Zn, Mg and Ca concentration. The films were deposited at 250 °C and Solution conditions were: copper acetate, 0.02 M; glucose, 0.02 M; and 2-propanol, 20% vol.*

These outcomes are consistent with Nolan and Elliott [11] DFT study for Zn and Mg doping (see Tab. 3.3). The negligible band gap modulation measured for samples ***Cu_2O:Zn*** and ***Cu_2O:Mg***, according to these authors, is due to the small structural distortions caused by Zn and Mg atoms (they have ionic radii similar to Cu^+) and the absence of mid-gap states. On the contrary, as regards Ca doping, while in our ***Cu_2O:Ca*** samples we did not observed any large band gap change, Nolan and Elliott reported a theoretical widening of 0.11 eV.

The electrical resistivity of ***Cu_2O:Zn***, ***Cu_2O:Mg*** and ***Cu_2O:Ca*** films, along with Cu_2O reference sample are reported in Fig. 3.44.

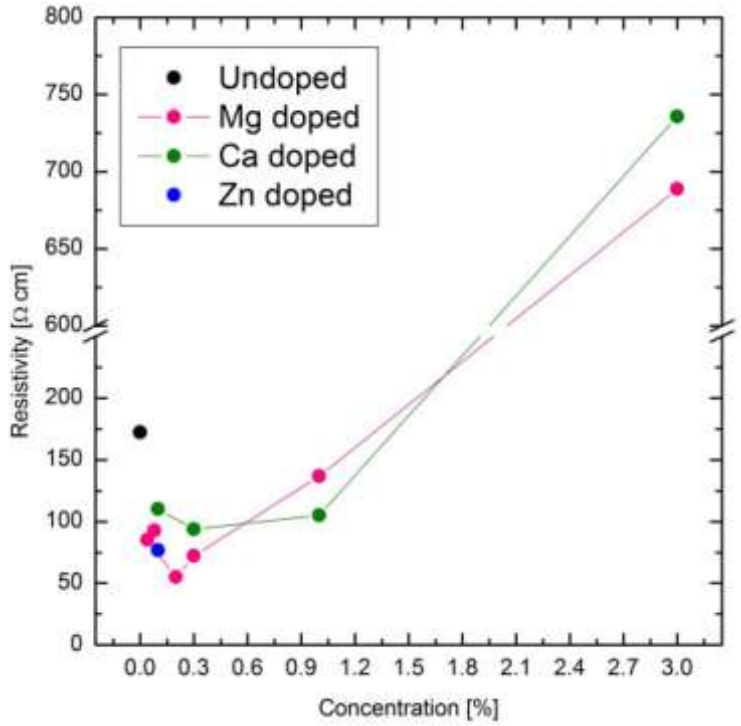

Fig. 3.44 *Electric resistivity as a function of Zn, Mg and Ca concentration. The films were deposited at 250 °C and Solution conditions were: copper acetate, 0.02 M; glucose, 0.02 M; and 2-propanol, 20% vol.*

For Zn, Mg and Ca concentrations less than 1%, the resistivity is much less than the value of the undoped film (see Fig. 3.44). Therefore, incorporation of such elements, presumably, augments the free charge carriers concentrations in Cu_2O. Whereas, at higher dopants concentrations (> 1%), the strong reduction of doped samples conductivity, compared to the undoped film, is owing to the degradation of charge carriers mobility, being the density of scattering centres increased. In this case, the mobility degradation overwhelmed the increase of charge carriers density.

The temperature dependence of the conductivity, in the range between 250 K and 400 K, was investigated also for samples ***Cu_2O:Zn***, ***Cu_2O:Mg*** and ***Cu_2O:Ca***. For all these doped films, as for the undoped reference sample ***U1***, the conductivity trend follows the Arrhenius law expressed in Eq. (3.6) and the same activation energy of 0.23 eV (see Fig. 3.45) was measured.

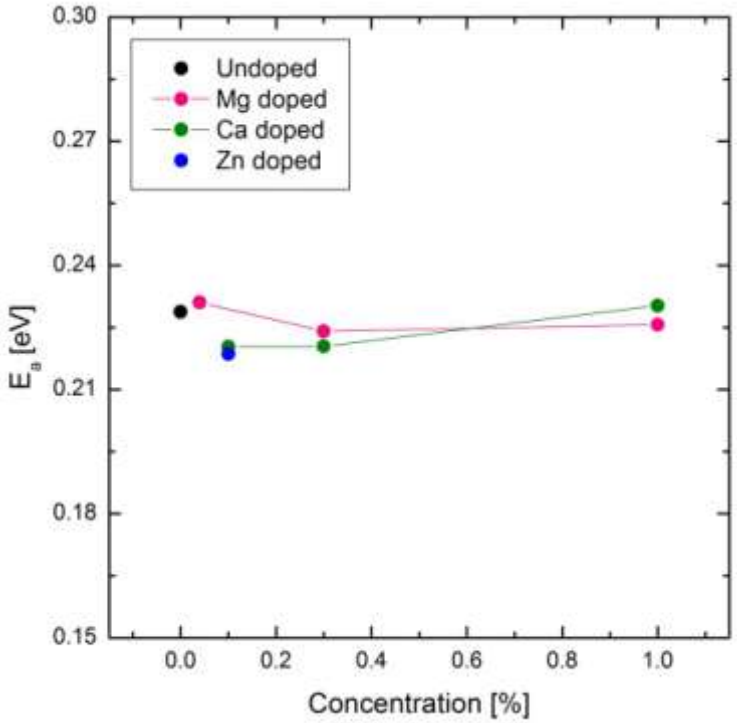

Fig. 3.45 *Conductivity activation energy as a function of Zn, Mg and Ca concentration. The films were deposited at 250 °C and Solution conditions were: copper acetate, 0.02 M; glucose, 0.02 M; and 2-propanol, 20% vol.*

This results indicates that the doped samples are p-type because the free holes are provided by the ionization of the shallow acceptor state introduced by the copper vacancies (see section 3.2). Moreover, it is evident that Zn, Mg and Ca, in spite of being n-type dopants, anyway, induce the formation of further copper vacancies, which in turn are responsible for the increase of the hole density. This kind of compensation mechanism, previously discussed in section 3.4, is typical for Cu_2O doping, and here it is reported for thin films deposited by spray pyrolysis.

In order to investigate the effects of Zn, Mg and Ca on the minority charge carriers (electrons), photo-conductivity measurements were carried out at room temperature employing a 100 mW/cm^2 Xe lamp. Indeed, the difference Δσ between the conductivity value in the dark and the value under constant illumination is directly related to the photo-generated charge carriers life time. The longer it is the more charge carriers are collected at the electrodes under illumination thus the film will be more conductive.

For sample ***Cu_2O:Zn*** (Zn/Cu = 0.1%) the same Δσ as for sample ***U1*** was measured (see Fig. 3.46).

On the other hand, for ***Cu_2O:Mg*** samples the scenario is a little more complex (see Fig. 3.46), in fact, for low Mg content (less than 1%) Δσ slightly increased in respect to the one measured for sample ***U1***, while, for Mg/Cu > 1%, surely due to a strong degradation of charge carriers mobility, Δσ resulted much lower.

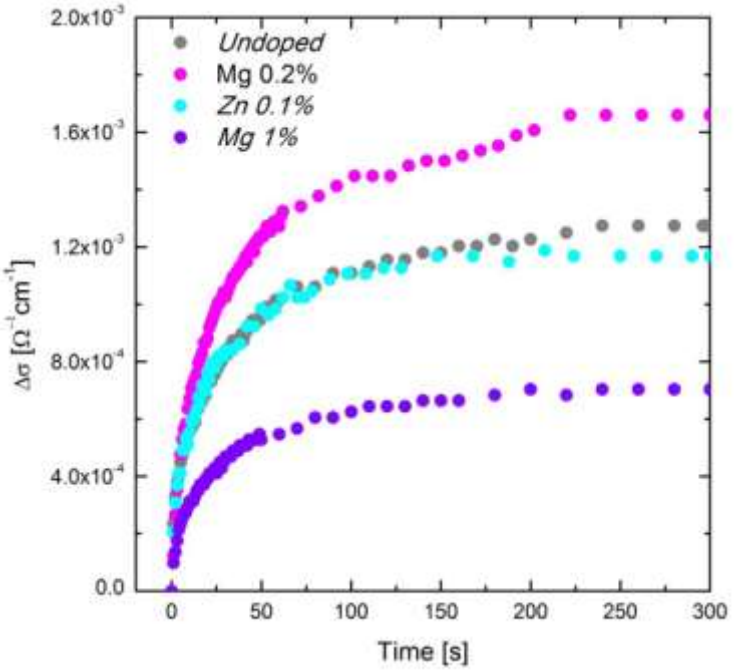

Fig. 3.46 *Difference Δσ between the conductivity value in the dark and the value under constant illumination as a function of time, for undoped (U1) and some Zn and Mg doped samples deposited at 250 °C. Solution conditions were: copper acetate, 0.02 M; glucose, 0.02 M; and 2-propanol, 20% vol.*

The slight enhancement of Δσ for samples doped at low Mg concentrations can be the experimental proof of the doping effects theoretically predicted by Isseroff and Carter [16], discussed in section 3.4. These authors stated that cations, such as Mg, Zn and Li, by means of their ability to hinder trap defects (split copper vacancies) formation, improve the hosting Cu_2O photo-conductivity. This hindering, in turn, depends on their ability to promote clustering of the second copper vacancy with the dopant (see section 3.4). According to their calculations, such clustering is only minimally energetically favourable, thus the photo-conductivity improvement will be small. Indeed, the contribution of Mg to ameliorate the photoconductivity of our Cu_2O samples, resulted moderate, indicating that the scenario proposed by Isseroff and Carter probably suits to explain our experimental outcomes.

3.8.c - Conclusions

The structural, optical and electronic properties of undoped and doped (Mg, Zn and Ca) Cu_2O thin films synthesized by ultrasonic spray pyrolysis have been investigated in terms of deposition and precursor solution parameters.

The formation process, by spray pyrolysis, of doped Cu_2O films appeared to be strongly influenced by the presence of Mg and Zn atoms in the solution. In particular we illustrated that these dopants modify the relations in the copper-oxygen system, diminishing the rate of the oxidation reactions involved in this specific material synthesis. The importance of this result relies on the fact that, doping offers to the method, another variable for the tuning, on molecular scale, of Cu_2O phase purity.

Subsequently, it was demonstrated that Mg, Zn and Ca doping, at proper concentrations (dopant/Cu < 3%), improves the electrical conductivity of the films due to the increase of free holes density, through the generation of copper vacancies. Since the used foreign elements are n-type dopants, the latter phenomenon is the proof that, for the conditions here used, n-type doping of Cu_2O synthesized by spray pyrolysis is hindered by spontaneous formation of compensating acceptor states.

Moreover, the modulation of the electrical conductivity has been achieved, in this work, without affecting the structural and absorption properties of the material.

Finally, the photo-sensitivity enhancement (about 30 %) observed for low Mg doped samples could be explained by the theoretical model by Isseroff and Carter [*Isseroff*], in which it is stated that Mg has a moderate potential to improve the photo-conductivity by inhibiting photo-charges trap states generation.

Bibliography

[1] Defects and Doping in Cu_2O - F. Biccari - Ph.D. thesis - Sapienza University of Rome (2009)

[2] A. Mittiga, E. Salza, F. Sarto. M. Tucci, R. Vasanthi - Applied Physics Letters **88**, 163502 (2006)

[3] T. Minami, Y. Nishi and T. Miyata; Applied Physics Express **6**, 044101 (2013)

[4] T. Minami, Y. Nishi, T. Miyata and J. Nomoto; Applied Physics Express **4**, 062301 (2011)[8] M. Hara, T. Kondo, M. Komoda, S. Ikeda, J. N. Kondo, K. Domen, K. Shinohara and A. Tanaka; Chemical Communications **3**, 357 - 358 (1998)

[5] S. Siah, Y. Lee, Y. Segal and T. Buonassisi - Journal of Applied Physics **112**, 084508 (2012)

[6] S. Lee, Y. Lee, J. Heo, S. Siah, D. Chua, R. Brandt, S. Kim, J. Mailoa, T. Buonassisi and R. Gordon - Advanced energy Materials - 1301916 (2014)

[7] E. Fortunato, V. Figueiredo, P. Barquinha, E. Elangovan, R. Barros, G. Gonçalves, S. Park, C. Hwang and R. Martins - Applied Physiscs Letters **96**, 192102 (2010)

[8] M. Hara, T. Kondo, M. Komoda, S. Ikeda, J. Kondo, K. Domen, M. Hara, K. Shinohara and A. Tanaka - Chemical Communications **3**, 357-358 (1998)

[9] A. Kargar, S. S. Partokia, M. T. Niu, P. Allameh et al.; Nanotechnology **25**, 205401 (2014)

[10] P. Korzhavyi, B. Johansson - Technical Report TR - 11 - 08 (2011)

[11] M. Nolan and S. Elliott - Chemistry of Materials **20**, 5522-5531 (2008)

[12] C. Malerba, F. Biccari, C. Ricardo, M. D'Incau, P. Scardi, A. Mittiga - Solar Energy Materials & Solar Cells **95**, 2848-2854 (2011)

[13] Transparent Electronics - From Synthesis to Applications - Edited by A. Facchetti and T. J. Marks - Wiley (2010)

[14] A. Mittiga, F. Biccari, C. Malerba - Thin Solid Films **517**, 2469-2472 (2009)

[15] O. Porat, I. Riess - Solid State Ionics **74**, 229 (1994)

[16] L. Isseroff and E. Carter - Chemistry of Materials **25**, 253-265 (2013)

[17] O. Porat, I. Riess - Solid State Ionics **81**, 29 (1995)

[18] W. Brattain - Review of Modern Physics **23**, 203 (1951)

[19] M. O''Keeffe and W. Moore - The Journal of Chemical Physics **35**, 1324 (1961)

[20] J. Bloem, A. van der Hovven, F. Kroger - Physica **22**, 1254 (1956)

[21] Physics of Solar Cells; From Principles to New Concepts - P. Würfel - Wiley-VCH (2005)

[22] Z. Yao, S. Liu, L. Zhang, B. He, A. Kuman, X. Jiang, W. Zhang and G. Shao - Applied Physics Letters 101, 042114 (2012)

[23] L. Chen - Materials Science in Semiconductor Processing **16**, 1172-1185 (2013)

[24] V. Figueiredo, E. Elangovan, R. Barros, J. Pinto, T. Busani, R. Martins an E. Fortunato - Journal of Display Technology Vol. 8 No. 1 (2012)

[25] F. Li, R. Waddingham, W. Milne, A. Flewitt, S. Speakman, J. Dutson, S.Wakeham, M. Thwaites - Thin Solid Films **520**, 1278-1284 (2011)

[26] P. de Jongh, D. Vanmeekelbergh and J. Kelly - Chemistry of Materials 11 112, 3512-3517 (1999)

[27] T. Kosugi and S. Kaneko - Journal of the American Ceramic Society 81 [12], 3117-3124 (1998)

[28] W. Lan, C, Tsai, S. Lee, W. Chao, M. Shih, Y. Chou, Y. Wu, Y. Hsu - 17th Opto-electronics and Communications Conference, July 2012 - Busan (Korea) - Technical Digest

[29] S. Ishizuka, S. Kato, T. Maruyama and K. Akimoto - Japanese Journal of Applied Physics Vol. 40, 2765-2768 (2001)

[30] J. Robertson and S. Clark - Physical Review B **83**, 075205 (2011)

[31] M. Li, J. Zhang, Y. Zhang and T. Wang - Chinese Physica B Vol. 21, No. 8, 087301 (2012)

[32] Y. Nakano, S. Saeki and T. Morikawa -Applied Physics Letters 94, 022111 (2009)

[33] H. Li, C. Pu, C. Ma, S. Li, W. Dong, S. Bao, Q. Zhang - Thin Solid Films **520**, 212-216 (2011)

[34] M. Mayer, AIP Conference Proceeding **475**, 541 (1999)

[35] J. F. Pierson, A. Thobor-Keck, A. Billard, Appl. Surf. Sci. **210**, 359 (2003)

[36] C. Malerba, C. Ricardo, M. D'Incau, F. Biccari, P. Scardi, A. Mittiga - Solar Energy Materials & Solar Cells **105**, 192-195 (2012)

[37] J Tauc - Materials Research Bulletin **3**, 37 (1968)

[38] S. Ghosh, D. K. Avasthi, P. Shah, V. Ganesan, A. Gupta, D. Sarangi, R. Bhattacharya, W. Assmann, Vacuum **57**, 377 (2000)

[39] Y. Seog Lee, M. T. Winkler, S. C. Siah, R. Brandt, T. Buonassisi, Applied Physics Letters **98**, 192115 (2011)

[40] SRIM - The Stopping and Range of Ions in Matter - J. Ziegler, J. Biersack, M. Ziegler - SRIM Co. USA (2008)

[41] D. Perednis and L. Gauckler - Journal of Electroceramics **14**, 103-111 (2005)

[42] J. Bogovic, A. Schwinger, S. Stopic, J. Schroeder, V. Gankel, H. Schuchmann, B. Friedrich - Metall Fachzieitschrift fur Metallurgic Vol. 65, 455-460 (2011)

[43] Thin-Film Transistors - C. Kagan and P. Andry - Marcel Dekker (2003)

List of publications

1) **Nanofabrication processes for innovative nanohole-based solar cells**
C. Garozzo, C. Bongiorno, S. Di Franco, M. Italia, A. La Magna, S. Scalese, P. M. Sberna and R. A. Puglisi
Phys. Status Solidi A Vol. 22 - 8, 1564-1570 (2013)

2) **Competition between uncatalyzed and catalyzed growth during the plasma synthesis of Si nanowires and its role on their optical properties**
C. Garozzo, A. La Magna, G. Mannino, V. Privitera, S. Scalese, P. M. Sberna, F. Simone, R. A. Puglisi
J. Appl. Phys. 113, 214313 (2013)

3) **Enhanced light scattering in Si nanostructures produced by pulsed laser irradiation**
P. M. Sberna, G. G. Scapellato, N. Piluso, S. Boninelli, M. Miritello, I. Crupi, E. Bruno, V. Privitera, F. Simone and S. Mirabella
Appl. Phys. Lett. 103, 221902 (2013)

4) **Raman and photoluminascence spectroscopy of Si nanocrystals: Evidence of a form factor**
G. Faraci, G. Mannino, A. R. Pennisi, R. Ruggeri, P. M. Sberna and V. Privitera
J. Appl. Phys. 113, 063518 (2013)

5) **TiO2/Cu2O All-Oxide Heterojunction Solar Cells Produced by Spray Pyrolysis.**
M. Pavan, S. Rühle, A. Ginsburg, D. A. Keller, H. Barad, P. M. Sberna, D. Nunes, R. Martins, A. Y. Anderson, A. Zaban, E. Fortunato
Solar Energy Materials & Solar Cells 132 549–556 (2015)

6) **Fe ion-implanted TiO2 thin film for efficient visible-light photocatalysis**
G. Impellizzeri, V. Scuderi, L. Romano, P. M. Sberna, E. Arcadipane, R. Sanz, F. Simone, V. Privitera
J. Appl. Phys. 116, 173507 (2014)

7) **Sputtered cuprous oxide thin films and nitrogen doping by ion implantation**
P. M. Sberna, I. Crupi, V. Privitera, F. Simone and M. Miritello
Submitted

International conferences

1) **IEEE-NMDC 2014 - Aci Castello (Italy) 12-15 October**
   Oral presentation:
   - *Effects of N and Mg doping in nanometric Cu_2O films*

2) **E-MRS 2014 Fall Meeting – *Warsaw (Poland) 15-19 September***
   Oral presentation:
   - *Nitrogen doping into copper oxide thin films for solar cells*
   - *Effects of Mg, Zn and Ca doping in nanometric Cu_2O films synthesized by Spray Pyrolysis*

3) **57th Course of the International School of Solid State Physics "Materials for Renewable Energy" - Erice (Italia) 12-18 July 2014**

4) **E-MRS 2014 Spring Meeting – *Lille (France) 25-30 May***
   Oral presentation:
   - *Enhanced light scattering in Si nanostructures produced by pulsed laser irradiation*

   Poster presentation:
   - *Nitrogen doping into copper oxide thin films for solar cells*

5) **E-MRS 2013 Spring Meeting – *Strasbourg (France) 27-31 May***
   Oral presentation:
   - *Enhanced light scattering in Si nanostructures produced by pulsed laser irradiation*

6) **56th Course of the International School of Solid State Physics "Materials for Renewable Energy" - Erice (Italy) 18-28 July 2012**

Acknowledgements

During my three years long activity, I had the luck to meet and work with a lot of people in Italy, Portugal and at the international conferences around Europe. Each of them gave me a contribution, from a constant and long dedication to just a stimulating talk, for the realization of these thesis. Therefore, I am glad to express here my, never sufficient, thankfulness for all of them.

A special thanks goes to Prof. Francesca Simone (University of Catania) for having wisely led me through all the important steps of my Ph.D.. I will always keep in my heart her patient dedication, trust and expert advices. For all these precious things now, I feel myself more mature and ready to continue my engagement in science and research.

The same sincere thanks is also for Dr. Vittorio Privitera (CNR-IMM), to whom I have a big debt for having given me the great chance to enlarge my knowledge in prestigious research centers abroad. To him I wish all the best for his current projects, sure of the fact that he is leading them with the same open mind and trust on young students, demonstrated in my case.

Furthermore, I am very grateful to Prof. Elvira Fortunato (Nova University of Lisbon), for having kindly accommodated me at the CENIMAT laboratories and for her distinguished supervision. In particular, I would like to thank her for having provided me the possibility to use with autonomy and responsibility all the facilities of the laboratory.

For their punctual and precise supervision I thank Dr. Maria Miritello (MATIS CNR) and Dr. Salvatore Mirabella (MATIS CNR).

For their expert and accurate contribution to the paper on enhanced light scattering in Si nano-structures, I would like to thank the co-authors (MATIS and CNR): Dr. Giorgia Scapellato, Dr. Nicolò Piluso, Dr. Simona Boninelli, Dr. Isodiana Crupi and Dr. Elena Bruno.

Moreover, a special thank goes to Dr. Rosaria Puglisi (CNR-IMM), which kindly involved me in some of her interesting works, that eventually appeared on important papers and enriched this thesis. Together with her I also thank, the not yet cited, co-authors (CNR) of the mentioned papers, to whom I gave my small contribution, specifically: Dr. Cristina Garozzo, Dr. Antonino La Magna, Dr. Giovanni Mannino, Dr. Silvia Scalese, Mr. Corrado Bongiorno, Mr. Salvatore Di Franco and Mr. Markus Italia.

I am very grateful to Dr. Giuliana Impellizzeri (MATIS CNR) and the other co-authors (MATIS CNR): Dr. Viviana Scuderi, Dr. Lucia Romano, Dr. Enrica Arcadipane and Dr. Ruy Sanz, for my participation in one of their innovative work on TiO_2.

I want also to express my deep thanks to the friend and colleague Dr. Michele Pavan, which, a part from the honest friendship, has been a source of advanced and accurate knowledge. Moreover, I thank him for having kindly asked my contribution in his paper on Cu_2O solar cells. To him goes my best wishes for his current Ph.D. studies.

Along with Michele, I am glad to thank, the not yet mentioned, co-authors of the above quoted paper: Prof. Rodrigo Martins (Nova University of Lisbon), Prof. Arie Zaban (Bar Ilan University), Dr. Sven Rühle (Bar Ilan University), Dott. Adam Ginsburg (Bar Ilan University), Dr. David A. Keller (Bar Ilan University), Dr. Hannah Barad (Bar Ilan University), Dr. Daniela Nunes (CENIMAT) and Dr. Assaf Anderson (Bar Ilan University).

I wish to thank, as well, Dr. Kasra Kardarian (CENIMAT) for his nice friendship, for the stimulating talks on spray pyrolysis and for all the professional help always benevolently provided. Also for him I send my best آرزوها بهترین for his future.

Deep acknowledgements are, then, for my friends and colleagues: Dr. Antonella Gentile, Dr. Stefano Boscarino, Dr. Giacomo Torrisi, Dr. Manuel Mendes, Dr. Seweryn Morawiec, Dr. Vicky Strano, Dr. Rosario Raciti, Dr. Eric Barbagiovanni, Dr. Gabriele Bellocchi, Dr. Salvatore Cosentino and all the other people of the MATIS group.

I want to manifest my gratefulness also to my friends Dr. Francesco Ruffino (MATIS) and Dr. Massimo Zimbone (MATIS) for their valuable suggestions and explanations.

For their fundamental technical support I am glad to thank also Mr. Giuseppe Pantè (MATIS), Mr. Salvatore Tatì (MATIS) and Mr. Carmelo Percolla (MATIS).

A profound thanks goes then to the friends of CENIMAT, in Lisbon, that hosted me as one of them and helped me, during my activity, specifically sharing their wide knowledge and providing accurate technical support. For this I thank: Dr. Joana Pinto, Dr. Alexandra Gonçalves, Dr. Sonia Pereira, Dr. Pedro Barquinha, Dr. Rita Branquinho, Prof. Hugo Aguas, Dr. Jonas Deuermeier, Dr. Tomas Calmeiro, Dr. Pawel Wojcik and Dr. Iwona Wojcik.

Aftrewards, I would like to thank Prof. Francesco Priolo (University of Catania and MATIS), the coordinator of my Ph.D. Prof. Francesco Riggi (University of Catania), Prof. Maria Grazia Grimaldi (University of Catania and MATIS), as the coordinator of the

PON01_01725 project that supported my activity, Prof. Antonio Terrasi (University of Catania and MATIS) and Prof. Giovanni Piccitto (University of Catania and MATIS).

Finally, I would like to state my recognition to my former tutors, respectively of the bachelor and master theses, Prof. Andrea Rapisarda (University of Catania) and Prof. Giuseppe Faraci (University of Catania).